

Introduction

The hydroxyls and cyclic structure in starch cause strong brittleness of starch, subsequently leading to some limitations such as insufficient adhesion and brittle film of starch in the applications of paper-making and textile fields. This work aimed to confirm that sulfo-itaconation can increase the adhesion of starch to fibers and lessen its film brittleness for improving its end-use ability, and to determine the optimal extent of starch sulfo-itaconation for the sulfo-itaconylated starch (SIS) samples.

Experimental process

Preparation

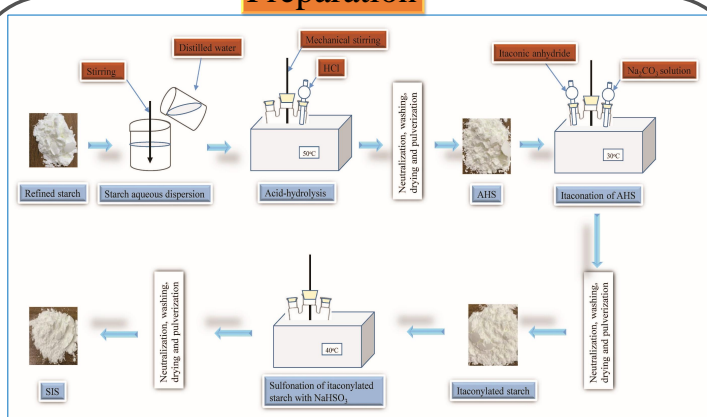


Fig. 1. Preparation process of SIS samples.

Characterization and measurement

- The obtained SIS granules in this work were characterized by the uses of Fourier transform infrared (FTIR) spectroscopy and scanning electron microscopy (SEM). Film characterizations with the SEM and x-ray diffraction (XRD) analyses were also conducted.
- The measurements on DS values of SIS samples, adhesion to cotton fibers, tensile strength and breaking elongation, bending endurance. All of the characterizations and measurements were carried out on SIS and acid-hydrolyzed starch (AHS, as a control) samples.

Results and discussion

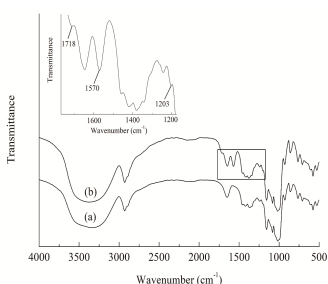


Fig. 2. FTIR spectra of AHS (a) and SIS with a DS value of 0.086 (b).

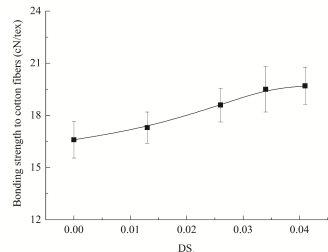


Fig. 3. Effect of sulfo-itaconation on the adhesion of starch to cotton fibers.

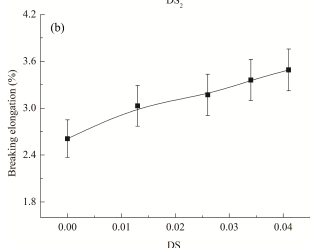
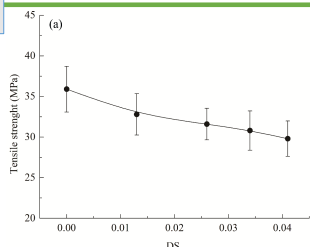


Fig. 4. Effect of sulfo-itaconation on tensile strength (a) and breaking elongation (b) of film.

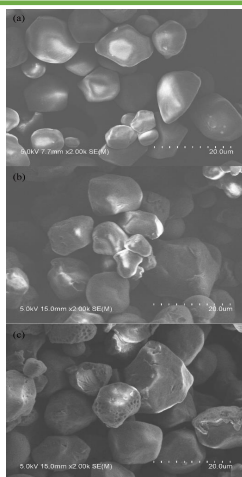


Fig. 5. SEM micrographs of granular native starch (a), AHS (b) and SIS (c).

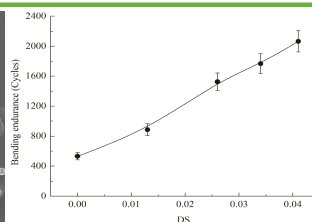


Fig. 6. Effect of sulfo-itaconation on bending endurance of starch film.

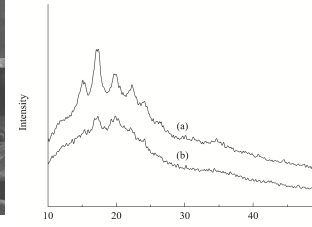


Fig. 7. XRD of AHS (a) and SIS (DS value of 0.041, b) films.

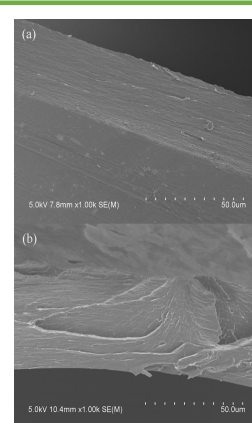


Fig. 8. SEM micrographs of tensile fracture cross-sections of AHS (a) and SIS (DS value of 0.041, b) films.

FTIR analysis confirms the successful preparation of SIS. The sulfo-itaconate substituents introduced onto starch chains can improve the adhesion to cotton fibers. The sulfo-itaconation also favors reducing film brittleness of starch which has been revealed by the XRD and SEM analyses of SIS and AHS films, promoting the breaking elongation and bending endurance of starch film, and enhancing its flexibility and extensibility.

Conclusions

- ◆ Starch sulfo-itaconation was an effective method to improve the adhesion of starch to cotton fibers and film properties for overcoming the shortcomings (insufficient adhesion and brittle film) of starch.
- ◆ On basis of the results of adhesion and film properties, SIS with a modification level range of 0.034-0.041 showed potential for the application as a new starch-based sizing agent in textile fields.



Development and Applications of Two-way reversible shape memory polymer: Benzoyl peroxide crosslinked poly(ethylene-co-vinyl acetate)

Jin Hui¹, Hong Xia², Yiping Qiu³, Yaqing Fu⁴, Qing-Qing Ni^{2*}
School of Textile and Clothing, Nantong University

Introduction

Shape memory polymers (SMPs) are smart materials that can significantly change their shape upon exposure to an external stimulus, such as temperature, water, light, electricity, magnetism, and pH, with temperature being the most common. SMPs have the potential to be used in a wide range of applications, including as actuators and sensors, and in aerospace technology, textile, and biomedical applications. The type of shape memory effect (SME) include one-way shape memory effects (1W-SME) and two-way shape memory effects (2W-SME). The 2W-SME is a novel SME that shows the full reversibility in heating and cooling that is required for many application as actuators.

Abstract

Two-way (reversible) chemically crosslinked semi-crystalline shape memory polymers with various crosslinking densities were synthesized by poly(ethylene-co-vinyl acetate) (PEVA) with different contents of benzoyl peroxide (BPO). The developed materials exhibited reversible shape changes by controlling the “switch on” temperature that triggers shape change within a reasonable temperature range. The PEVA-B10 samples exhibited both optimal actuation performances and excellent recovery ratio over 99%. BPO as the crosslinker played an important role in allowing samples to return to their original shape. The developed PEVA/BPO materials indicated enough soft performance and good mechanical properties even at large deformation, which may contribute to the potential applications in the fields of soft material actuators and other applications.

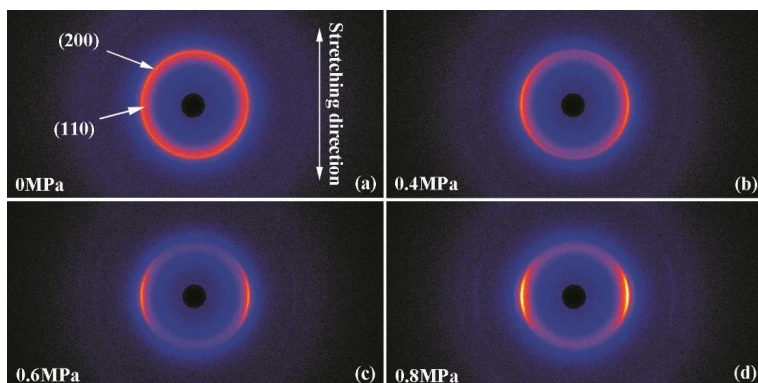


Figure 1. 2D-WAXS patterns of the PEVA-B10 sample after cooling as (i) unstretched and under different stress conditions: (ii) 0.4MPa; (iii) 0.6MPa; (iv) 0.8MPa. White arrows indicated the stretching direction. (e) The second heating run of PEVA-B10 sample in DSC test, the sample stretched at various stresses (0.4 MPa-0.8 MPa) and unstretched one.

Result and discussion

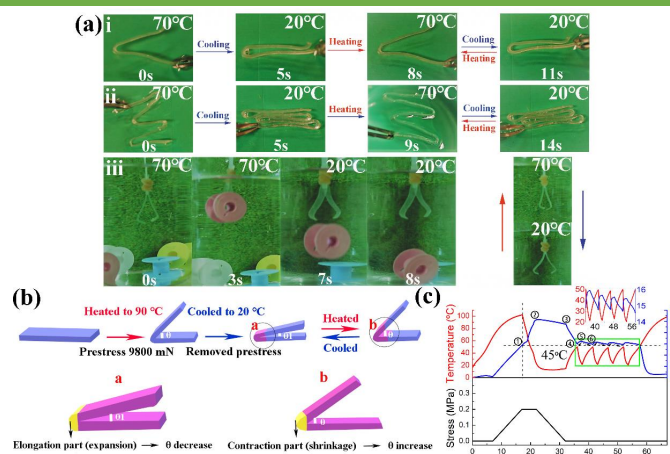


Figure 2. (a) The picture of “V”, “M” and gripper shapes of PEVA-B10 sample in the hot and cold water taken from video. (b) Schematics of the stress-free PEVA/BPO two-way shape memory behavior design. (c) Stress-free two-way shape memory cycles of PEVA-B10 sample.

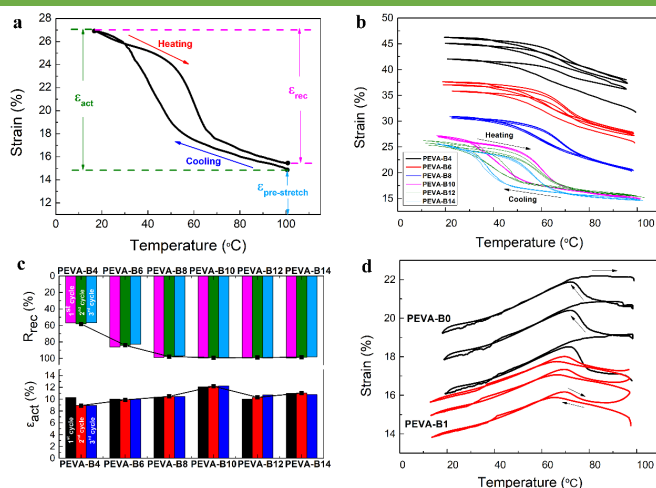


Figure 4. a: Definition of two-way shape memory process; b: Two-way shape memory behavior of samples with various benzoyl peroxide (BPO) contents of 4 wt% to 14 wt% under 0.2 MPa; c: Actuation and recovery capabilities, the actuation strain (ϵ_{act}) represents crystallization leading to elongation upon cooling, the recovery ratio (R_{rec}) represents the recovery capabilities during heating; d: Two-way behavior of a low crosslinking density sample of 1 wt% BPO and a non-crosslinked sample under 0.02 MPa.

Conclusion

We synthesized a two-way (reversible) shape memory polymer using BPO crosslinked PEVA. The recovery ratios of high crosslinking density samples are over 99% that can almost completely recover to original shape. BPO as the crosslinker was key issue for shape recovery behavior, and high crosslinking density in PEVA/BPO leads to a significant increment of recovery ratio. The developed PEVA/BPO materials indicated enough soft performance and better mechanical properties even at large deformation. The PEVA-B10 sample exhibited both optimal actuation strain of 12.22 % and shape recovery ratio of 99.68%. These properties could contribute to the potential application as soft material actuators, artificial intelligence and other applications.

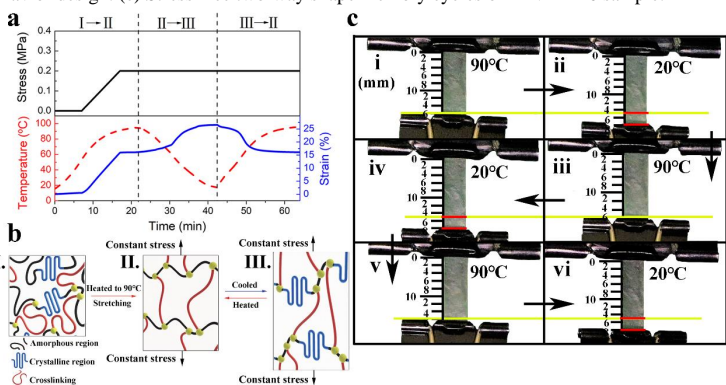


Figure 3. a: Two-way shape memory cycles for PEVA-B10. b: Mechanism of reversible behavior. c: Two-way behavior of PEVA-B10 at 90 °C and 20 °C under constant stress.



Damage detection of CFRP composites by electromagnetic wave nondestructive testing (EMW-NDT)

Jun Hong^{1,2}, Zhenzhen Xu², Hong Xia³, Qing-Qing Ni^{3*}

1 Interdisciplinary Graduate School of Science and Technology, Shinshu University, Ueda 386-8567, Japan.

2. College of Textile and Garments, Anhui Polytechnic University, Wuhu, China

3. Department of Mechanical Engineering & Robotics, Shinshu University, Ueda 386-8567, Japan.

Introduction

Damages such as fiber breakage and delamination are likely to occur inside CFRP composites when subjected to external forces, such as impact and fatigue load. These damages are mostly invisible and cause safety hazards during the service of the products. This study proposes a new type of nondestructive testing (NDT) method using electromagnetic wave (EMW) technique, EMW-NDT. It was proven that the proposed EMW-NDT method is effective in detecting damages such as delamination, crack or other defects in CFRP composites. The EMW-NDT method's detection capacity to the delamination size, delamination thickness, and slits in CFRP composites were investigated.

Experiment and Methods

Material Preparation

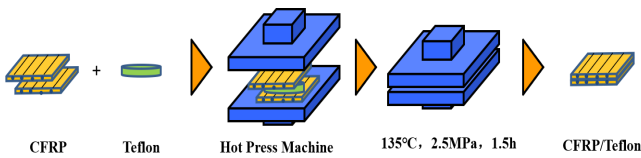


Fig.1 Fabrication process of CFRP composites inserted with Teflon film

Table 1. Properties of the Teflon film used in this study

Profile	Value	Unit
Thickness	0.05	mm
Permittivity	2.1	-
Volume Resistivity	over 1×10^{17}	$\Omega \cdot \text{cm}$

EMW-NDT measurement

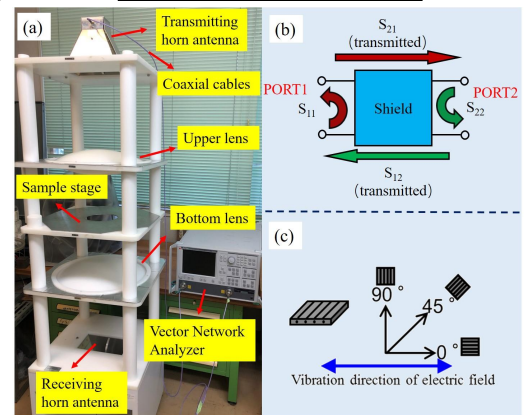


Fig. 2. (a) The specially designed free-space measurement system and its set-up, (b) illustration of the S-parameter obtained via measurement, (c) incident angle of the EM wave between fiber direction and electric field direction

Results and Discussion

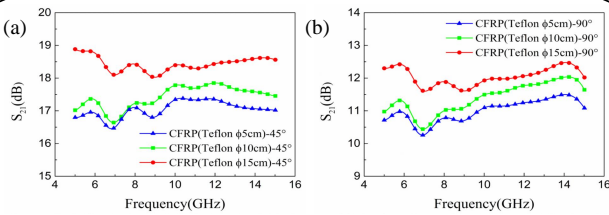


Fig. 3. S_{21} (dB) values of CFRPs inserted with various diameters of Teflon film under the testing angles of 45° (a) and 90° (b);

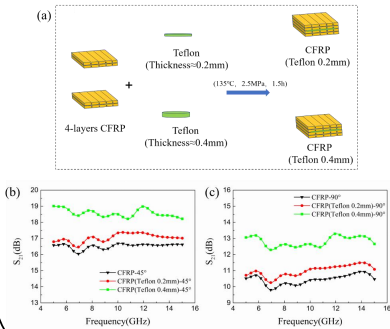


Fig. 4. (a) Preparation process of CFRP inserted with different thicknesses of Teflon film; (b) (c) SE values at the incident angles of 45° and 90°.

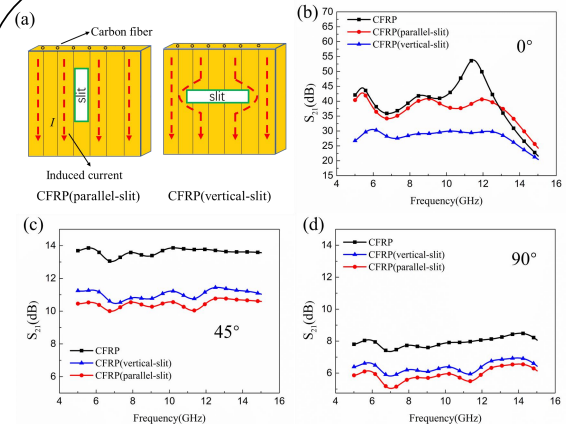


Fig. 5. (a) CFRPs with slits; SE values of the CFRPs at different incident angles of (b) 0°, (c) 45°, and (d) 90°

- EMI SE values of the parallel-slit CFRP were higher than the vertical-slit CFRP at the 0° incident angles.
- The slit and its orientation can be identified successfully by the EMW-NDT method.

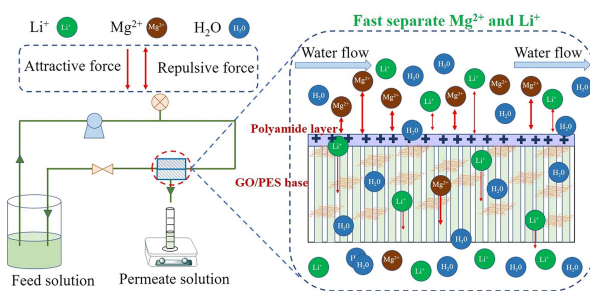
Conclusions

1. Delamination damage with different sizes and thicknesses could be identified with high detection sensitivity using the proposed EMW-NDT method;
2. Both the slit and its direction were identified successfully based on the characteristics of EMI shielding anisotropy in CFRPs;
3. The proposed EMW-NDT method exhibits vast potential for NDT application of CFRP composites and uses in various fields.

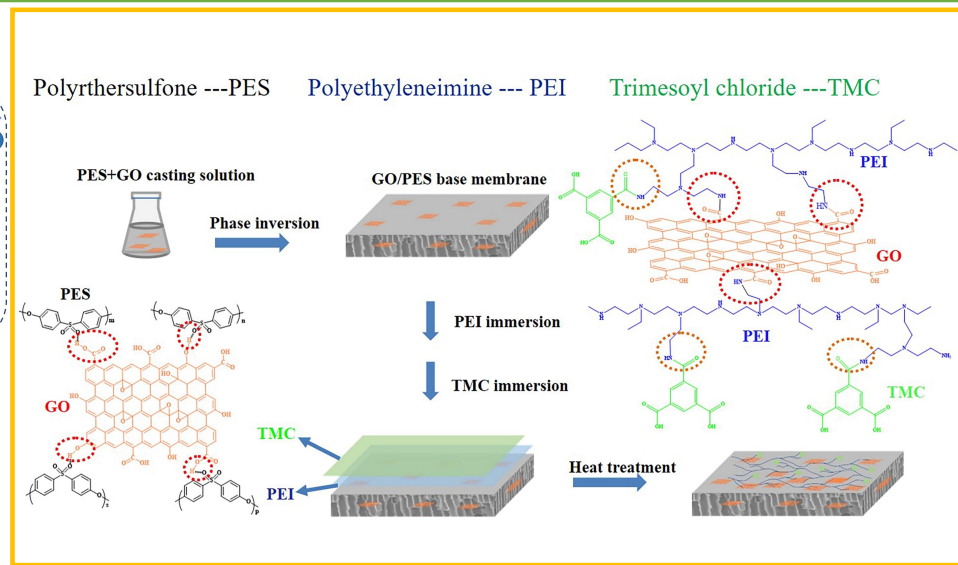
Introduction

To extract lithium resources from brines, it is necessary to achieve effective separation of Mg^{2+}/Li^+ . In recent years, nanofiltration (NF) membrane, an environment friendly approach for separating Mg^{2+} and Li^+ , has drawn more attention in the field of lithium recovery. However, there are few articles on Mg^{2+}/Li^+ separation using NF membranes. Many reported membranes performed excellent during the process of Mg^{2+}/Li^+ separation, while most of them showed low flux at the same time, which limited the work efficiency and application of NF membrane. Additionally, most studies on Mg^{2+}/Li^+ separation using NF membranes focused on modification for polyamide layer, while no reports on optimizing for substrate membrane. In order to efficiently extracting lithium, both high permeation flux and high separation ability for Mg^{2+} and Li^+ are necessary. The goal of this work is to synthesize a novel NF membrane with high permeation flux, high separation performance and long-time stability for improving the lithium extraction purity and efficiency.

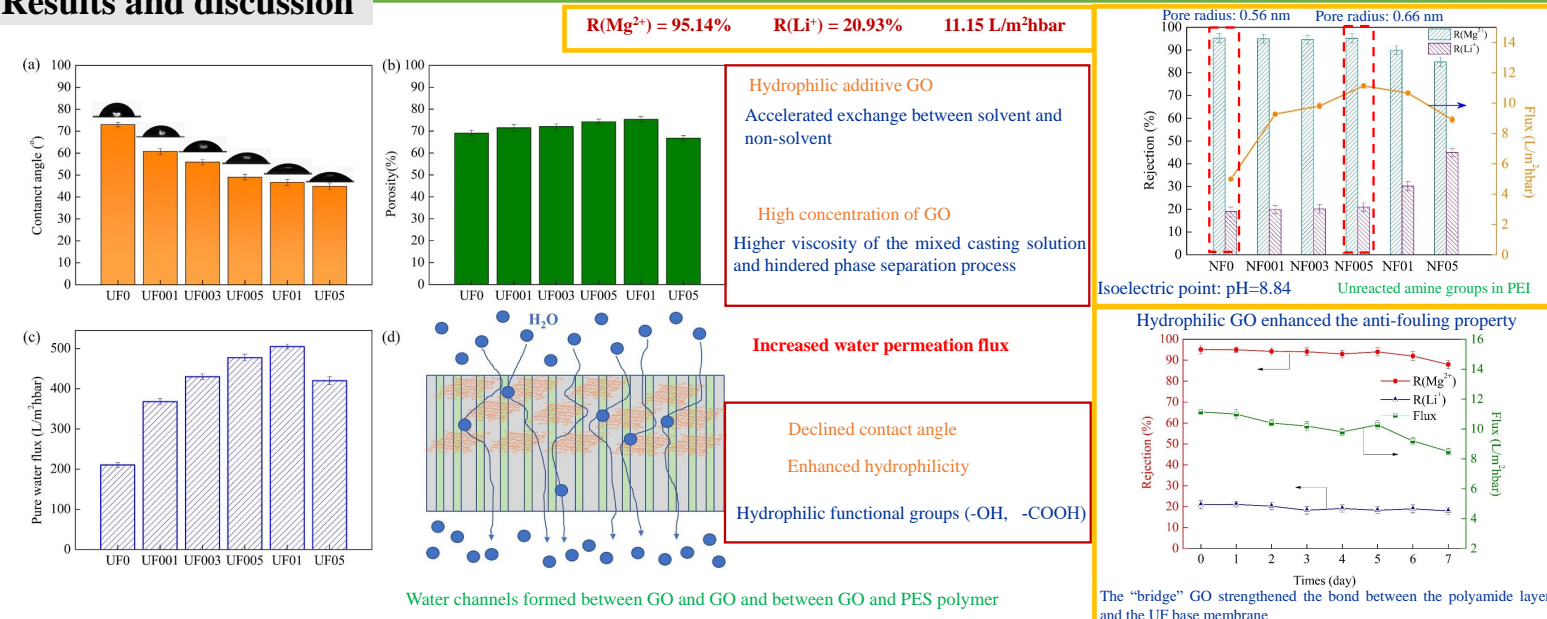
Experimental process



From the perspective of optimizing the substrate film, we modified polyethersulfone (PES) ultrafiltration (UF) substrate membrane with GO nano-additives to improve the mechanism and hydrophilicity performance, followed with interfacial polymerization between PEI and TMC.



Results and discussion



Conclusions

- The hydrophilic GO acted as a “bridge” between UF membrane and polyamide layer due to the “anchor effect”, which significantly enhanced the interaction between base membrane and polyamide layer.
- A small amount of GO doping greatly improved the permeability of both UF and NF membranes, which correspondingly improved the separation efficiency and accelerated the filtration rate.
- Compared to previously reported articles, the obtained NF membrane prepared in this work exhibited an optimal Mg^{2+}/Li^+ separation performance and efficiency, the rejection for Mg^{2+} and Li^+ and the flux were 95.14%, 20.93%, and $11.15 \text{ L/m}^2\text{hbar}$, respectively.

Development of multifunctional stimuli-responsive shape memory polyurethane for soft actuators target to biomaterials

Suphassa Pringpromsuk¹, Hong Xia², Qing-Qing Ni²

¹Graduate School of Medicine, Science and Technology, Shinshu University, Japan

²Faculty of Textile Science and Technology, Shinshu University, Japan

Introduction

As the average human age in global society increases, the effects of some injuries can be replaced by using polymer as artificial equipment.

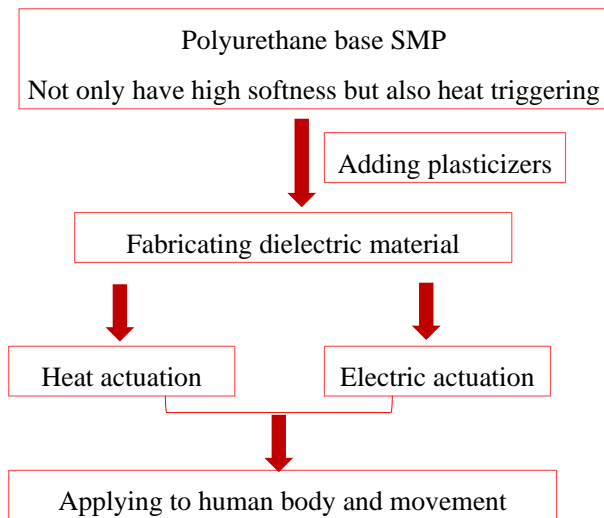
- **Metallic or alloy** have side effect during long term use inside human body



▪ **Shape memory polymers** have developed as soft actuator to be expected for biomaterial application such as smart bandage, stent and artificial muscles.

Among SMPs, **polyurethane-based SMPs** have features such as shape recovery, good processability, light weight, and low cost.

Experimental process



Film characterization

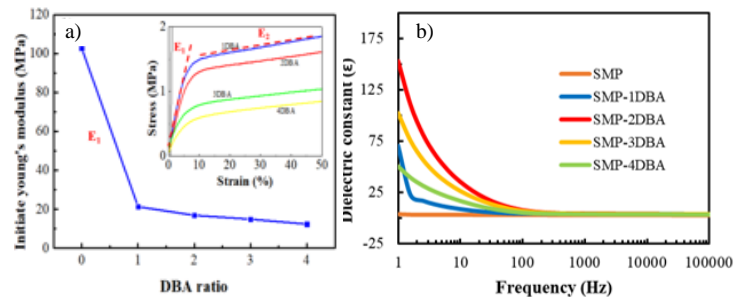


Fig.1 a) young's modulus b) dielectric constant of SMP films

The young's modulus and dielectric constant are the main factor on the **Maxwell stress** principle to fabricate this soft actuator

Results and discussion

Heat actuation

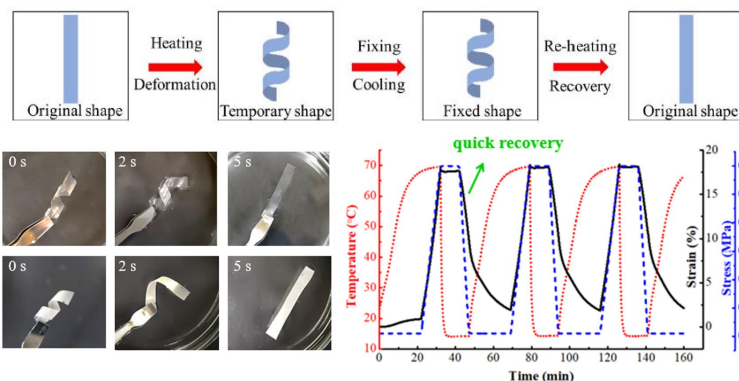


Fig.2 Direct thermal applied and thermomechanical analysis under 3 cycles

- The film could be stretched up to a large strain and then **rapidly** recover back to their original shape
- They could be reproducibility, shown as good repeatability for 3 cycle

Electric actuation

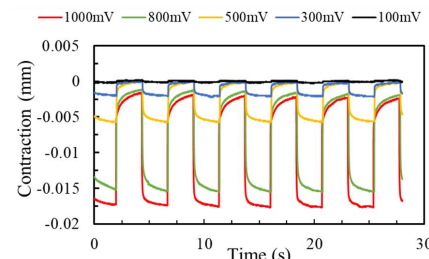
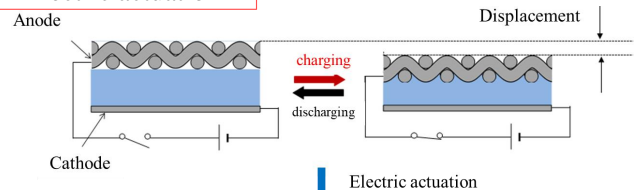


Fig.3 Deformation of the SMP gel actuator on DC on-off

Two-way shape deformation of **contraction and expansion** were tested over many electric on-off cycles and the largest contraction reached 6.76%. They acted similar to human movement at low frequency

Conclusions

- ✓ Enhancing softness
- ✓ Good in both thermal and electric actuation
- ✓ Similar to human muscle movement by electric field
- ✓ Activating at human body temperature
- ✓ This work could be developed to be artificial muscle and biomaterials in the future

The Research on Low-velocity Impact Performance of 3D Woven Textile Composites

Yajun LIU, Hong XIA, and Qing-qing NI

Graduate School of Medicine, Science and Technology, Shinshu University
3-15-1, Tokida, Ueda, Nagano, 386-8567, Japan,
niqq@shinshu-u.ac.jp



Introduction

Fiber reinforced composites have a great application in recent decades among automobiles, aerospace, civil and sports. Compared with traditional laminated composites, three-dimensional (3D) woven textile-reinforced composites have better delamination resistance and impact resistance, due to introducing the binder yarn in the thickness direction. The current research mainly study on the development of 3D woven textile composites with different weaving structures and their low-velocity drop weight impact performance.

Experimental

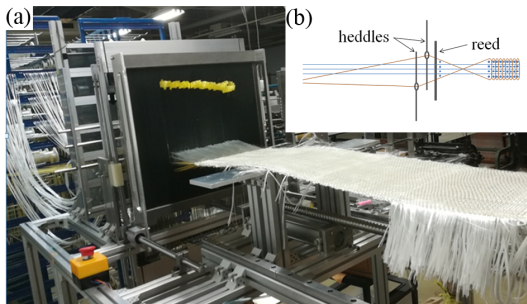


Figure. (a) Self-built 3D weaving loom and (b) a schematic of the weaving technique.

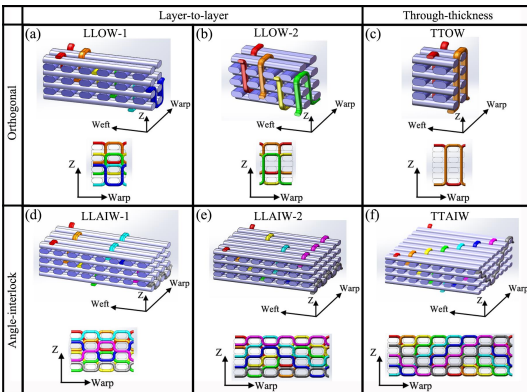


Figure. 3D model of the six designed 3D woven textiles.

Six 3D woven textiles, named LLOW-1, LLOW-2, TTOW, LLAIW-1, LLAIW-2, and TTAIW, were manufactured based on a self-built 3D weaving loom with a modified heddle position system.

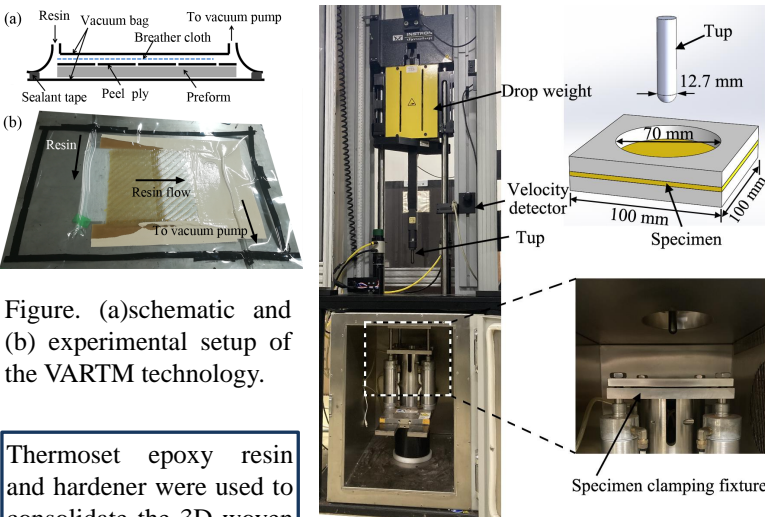


Figure. (a) schematic and (b) experimental setup of the VARTM technology.

Thermoset epoxy resin and hardener were used to consolidate the 3D woven textile preforms using VARTM technology.

Figure. Experimental setup of the low-velocity drop-weight impact test.

Application of Fiber Reinforced Composite



Results

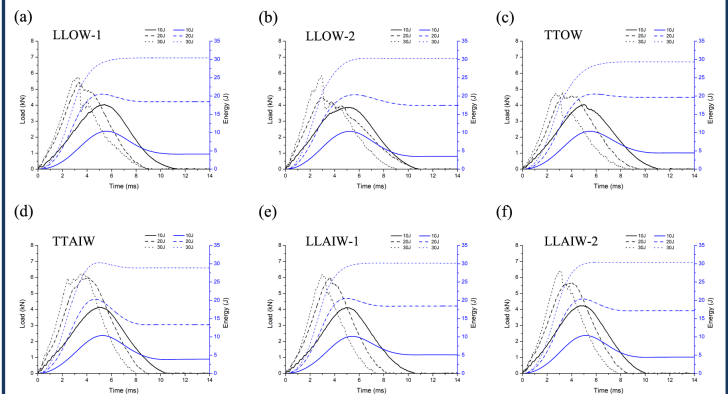


Figure. Representative load/energy-time curves of low-velocity drop-weight impact for six 3D woven composites subjected to three impact energy levels: 10, 20, and 30 J.

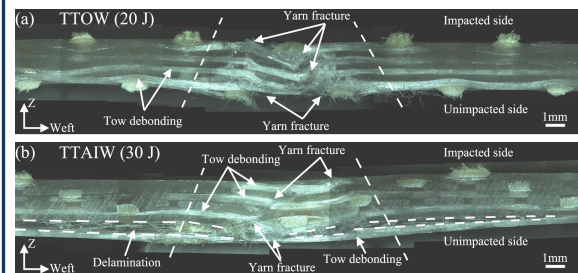


Figure. Through-thickness failure map of composites.

Conclusion

Six types of glass/aramid fiber hybrid 3D woven textiles with different binder yarn paths and binding patterns were manufactured on the basis of a self-built 3D weaving loom with a modified heddle position system. The 3D textile-reinforced epoxy resin composites were fabricated with VARTM technology, and low-velocity drop-weight impact tests of the composites were conducted under 10, 20, and 30 J impact energy levels. It was found that the composites with different woven structure and fiber volume fraction are not sensitive to low energy impact (10 J and lower energy), but sensitive to higher impact energies (20 and 30 J). Woven structure is a key parameter on the impact resistance of these 3D woven composites. The woven structure has an obvious influence on failure modes of the composites subjected to low-velocity impact.

Examination of new viscoelasticity evaluation method

Using ultrasonic waves

KOUHEI YAMADA and QING-QING NI

Department of Mechanical Engineering and Robotics, Shinshu University, Ueda, Japan

Introduction

Viscoelasticity is the combination of elasticity and viscosity, and is one of the indexes for evaluating physical properties of materials. Viscoelasticity is dependent on temperature and frequency. Generally, viscoelasticity is measured using DMA(Dynamic Mechanical Analysis). However, this measurement method is limited to a frequency of about 10^2 Hz due to the mechanical limit of the device, and it is not possible to directly measure viscoelasticity in the frequency range above kHz. In the conventional method, the viscoelasticity in the high frequency region is measured by using the conversion law, but there is a problem due to the conversion error.

Therefore, in this study, the viscoelasticity in the high frequency region was directly measured using U-DMA (Ultrasonic Dynamical Mechanical Analysis). There are two types of U-DMA, the "bottom method" and the "surface method", and currently there is a measurement error between these two types. The purpose of this study is to investigate the cause of this measurement error and to examine the usefulness of U-DMA.

Measuring method

Measuring device

The ultrasonic viscoelasticity measuring device URM <prototype> shown in the right was used. The principle of the device is to calculate viscoelasticity using complex elasticity theory.



Measurement principle

In this device, ultrasonic waves are incident by a transducer and the reflected waves occur at each boundary which are used for viscoelasticity evaluation. The reflection waveform is cut out, and L' , L'' , and $\tan \delta$ are obtained from the amplitude spectrum and phase spectrum obtained by the fast Fourier transform. In this study, two types of measurements were performed, the bottom method and the surface method. Figure 1 shows the principle diagram of U-DMA. In addition, the principles of the bottom surface method and the surface method are shown respectively.

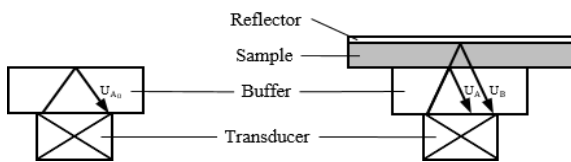


Fig.1 Principle diagram of U-DMA

Bottom method

Damping factor α
Phase velocity V_p

Storage modulus $L' = \rho V_p^2$
loss modulus $L'' = \frac{2\alpha V_p}{\omega} L'$
Loss sine $\tan \delta = \frac{L''}{L'}$

Surface method

Reflectance $|R_2| = \left| \frac{A}{A_0} \right|$
 $R_2 = \frac{Z_2 - Z_1}{Z_2 + Z_1}$
 $L^* = L' + iL'' = \frac{Z_2^2}{\rho_2}$

Results and discussion

Measurement sample

Table 1 shows the samples used in this measurement.

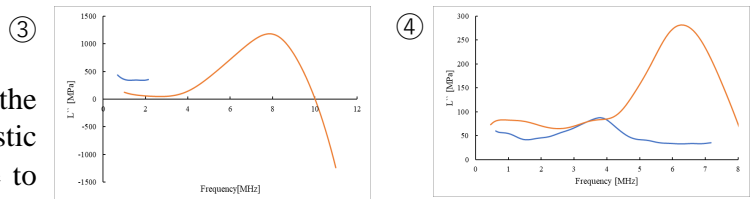
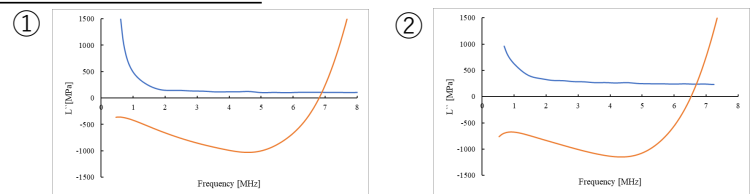
Table 1 Measurement sample

Sample	①Acryl	②PET	③NR	④PVC
Density[g/cm^3]	1.19	1.27	1.57	0.902
Thickness[mm]	3.00	3.00	3.00	4.00

Measuring method

From previous studies, the bottom surface method and the surface method cause measurement errors in the loss elastic modulus L'' . In this study, the error factor is assumed due to couplant. Therefore, only PVC is measured by the bottom method and the surface method without adding couplant.

Measurement result



— Bottom method
— Surface method

The measurement result of PVC has the smallest error.

Conclusion

The error factor between the bottom method and the surface method was confirmed due to couplant. Therefore, the measurement accuracy of U-DMA could be improved by considering effect of couplant in the theoretical formula.

A strong, ultrastretchable, antifreezing and high sensitive strain sensor based on double network ionic conductive organohydrogel

Di Wang, Qufu Wei*
Jiangnan University

Introduction

With the rapid development of artificial intelligence and the growing demand for human-machine interfaces, the flexible ionic conductive sensors have drawn extensive attention. As the flexible ionic conductive sensors have been expanded into various applications such as wearable devices, electronic skin and human health monitoring, the flexible ionic conductive sensors have been numerously studied for enhancing mechanical performance, expanding operating conditions and improving ionic conductivity

Experiment

Gelatin and potassium persulfate were dissolved in the NaCl solution under vigorously stirring at 80 °C. After that, acrylamide monomers and N,N-methylenebisacrylamide were slowly dropped into the above solution. The precursor solution was adsorbed into the PU electrospun fiber membrane and cross-linked at 60 °C for 2 h. During this time, PAM was grafted onto the gelatin chains and the crosslinked PAM/GE hydrogels were formed in the network of PU electrospun fiber membrane. Finally, the as-prepared hydrogel membrane was soaked in the NaCl glycerol/H₂O binary solvent to endow the organohydrogels membrane antifreezing properties and ionic conductivity

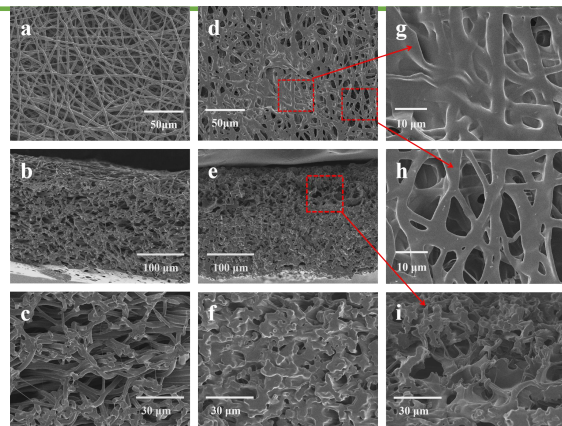
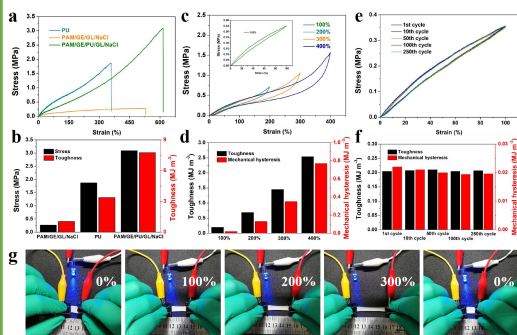


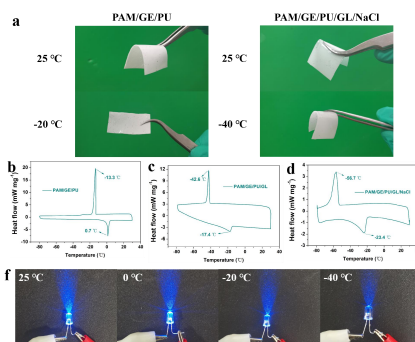
Figure SEM images of pure PU electrospun fiber membrane and PAM/GE/PU/GL/NaCl.

Results and discussion

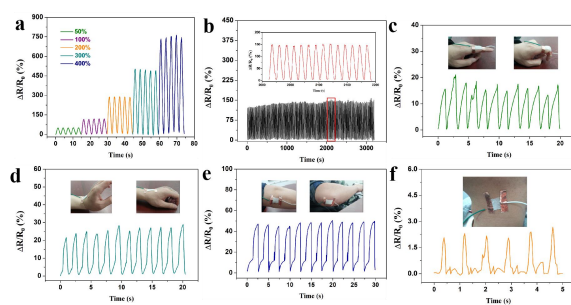
Mechanical property



Antifreeze Property



Sensing property



Conclusions

In summary, a facile method of composite organohydrogels with eletrospun fiber membrane was successfully employed to prepare the double network PAM/GE/PU/GL/NaCl organohydrogel with integrated characteristics, including excellent mechanical property (strain up to 614%, stress up to 3.09 MPa), superb antifreeze performance (-40 °C), high ionic conductivity (1.51 S m⁻¹) at room temperature and remarkable elasticity. In addition, the ionic conductive organohydrogel was served as a strain sensor to monitor human movements and subtle motion signals with high strain sensitivity, good stability and repeatability.

A Stretchable Electrode for Single Enzymatic Biofuel Cells

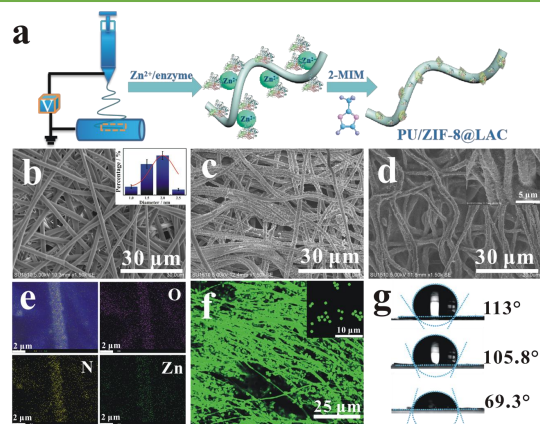
Xin Li, Qufu Wei*
Jiangnan University

Introduction

The rise of energy harvesting textiles has opened up an emerging path to prospective energy solution for the next generation of wearable electronics. Flexible electrodes as the core link in enzymatic biofuel cell (EBFC) should be stretchable while utilizing enzyme molecules to transfer the energy from chemical of green fuels into electrical, which is beneficial to meet the key requirements of practical applications and shows considerable potential in wearable electronics.

Experiment

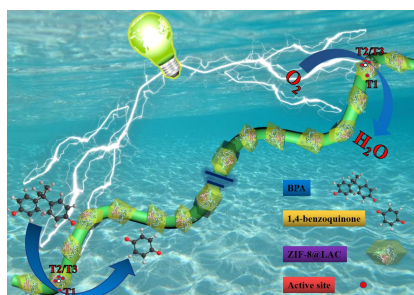
The synthesis method of PU/ZIF-8@enzyme is consistent with our previous work and the synthesis mechanism is exhibited in Figure. Prior to the synthesis of ZIF-8@LAC, the PU were treated by the plasma treatment for 30 s in a vacuum with a power of 20 W. Followed by 3 g zinc nitrate containing 0.3 g LAC getting dissolved in 100 mL PBS solution then stirred for 0.5 h. The PU was further immersed into the prepared solution for 12 h. After being washed for 3 times, the nanofiber was put into 2-MIM solution for 24 h under standing condition. After that, the electrode was obtained by soaking it in CNTs dispersions and then dried at 45 °C



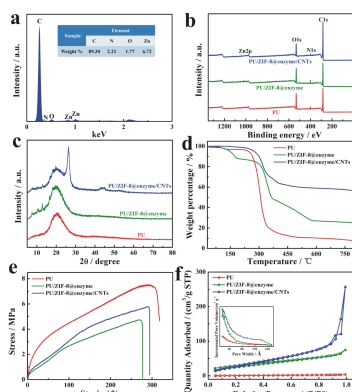
Schematic illustration showing the synthesis of PU/ZIF-8@LAC; SEM images of each samples

Results and discussion

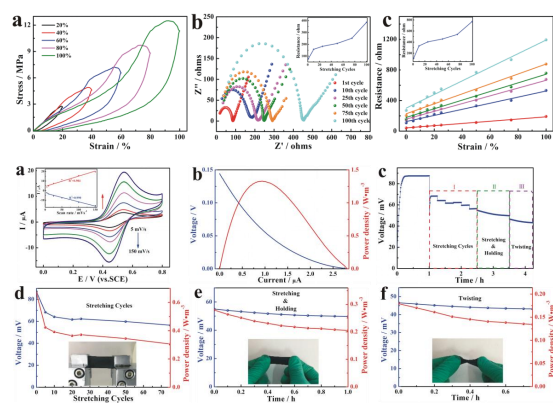
Schematic of single-EBFC



Characterization of electrode



Performance of single-EBFC



Conclusions

The development of a new and reliable stretchable electrode with the ability to effectively comply the body profile as well as withstand repeated mechanical stress for powerful wearable energy is a key component of the further development of flexible devices in wearable electronic systems. Herein, we created a stretchable PU/ZIF-8@LAC/CNTs electrode by encapsulating enzyme into ZIF-8 crystals during the process of in-situ growth of ZIF-8 on electrospun PU nanofiber membranes. The as-fabricated electrode showed excellent elasticity and stable electrical property after repeated stretch cycles. The current developments suggests considerable applications in wearable sensors and monitoring systems.

Structural colouration of polyester fabrics with high colorfastness by bipolymer photonic crystals containing reactive epoxy groups

Peng Yan¹, Yinchun Fang¹, Xinhua Liu^{1*}

¹Anhui Polytechnic University, Wuhu, China,

*Corresponding authors: E-mail addresses Liuxinhua66@163.com

Introduction

Photonic crystals (PCs) have received more and more attention for constructing structural colors due to it is a kind of photonic nanomaterials with photonic band gap forming by closely packed periodic arrangement of nanospheres with different reflective index. PCs have been reported to fabricate the structural colors on smooth, seamless and rigid solid substrates such as glass and silicon. However, textile fabrics consist of a network of natural or chemical fibers containing voids and gaps between fibers and yarns which are quite different from the solid substrates. Hence, it is more difficult to fabricate the PCs structural colors on textile fabrics than on the solid substrates.

In this paper, the bipolymer of poly (tert-butyl acrylate-co-glycidyl methacrylate) (P(t-BA-co-GMA)) containing reactive epoxy groups was synthesized and used as the photonic crystal to fabricate the structural color on black polyester fabrics. The color properties of different P(t-BA-co-GMA) bipolymers with different mass ratio of t-BA and GMA were investigated. The colorfastness were also investigated. This research will provide the experimental basis for the development of photonic crystals structural color on fabrics with high colorfastness to promote the practical application of structural color in textile colorization.

Experimental process

1.Synthesis of P(t-BAco-GMA)

t-BA and GMA with different mass ratio and 0.05g sodium bicarbonate were evenly dispersed into a 150 mL round-bottom flask filled with 90 mL deionized water. And then N₂ gas was injected into the flask for 15 min. After that the flask was put into the water bath of 80 ° C which was kept stirring for 30 min. And then 0.15 mmol (NH₄)₂S₂O₈ was dissolved into 10 mL deionized water which was used as initiator solution. After that, the 10 mL (NH₄)₂S₂O₈ solution was added into the above reaction flask using a syringe. The reaction was kept at 80 ° C for 4 h. After that the reaction solution was centrifuged at 11000 rpm for 40 min to obtain the solid product.

2.Preparation of structural color on black polyester fabric

2 g P(t-BA-co-GMA) were added into 50 ml conical flask with 20 ml deionized water which was magnetic stirred for 2 h to obtain the uniform nanospheres dispersion. The black polyester fabric with the diameter of 8 cm was placed on a sealed foamed plastic box. 10 mL nanospheres dispersion was added into the WH-2000 ultrasonic nebulizer (Guangdong Yuehua Medical Device Factory Co. Ltd, China) which was sprayed out from the nozzle to form the atomization and deposit on the polyester fabrics. Then the fabrics were dried on an oven at 40 °C for 10 minutes, and then the structural colored fabrics were obtained.

Results and discussion

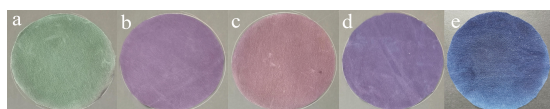


Figure 1

The photographs of structural colors of P(t-BA-co-GMA) nanospheres on polyester fabrics with different mass ratio of t-BA and GMA are shown in Figure 1. Five different colors of P(t-BA-co-GMA) nanospheres on black polyester fabrics were obtained with different mass ratio of t-BA and GMA.

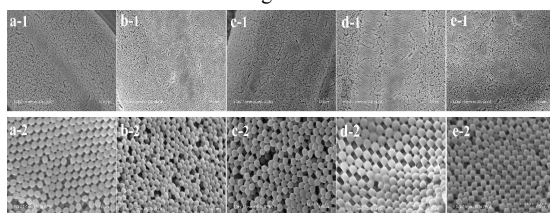


Figure 2

The SEM images of P(t-BA-co-GMA) nanospheres on polyester fabrics with different mass ratio of t-BA and GMA are shown in Figure 2. As shown in Figure 2, all the P(t-BA-co-GMA) nanospheres with different mass ratio of t-BA and GMA were successfully formed close-packed coating on polyester fabrics.

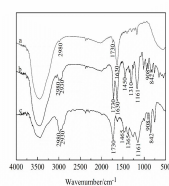


Figure 3

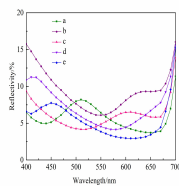


Figure 4

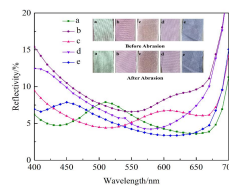


Figure 5

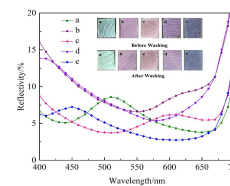


Figure 6

The chemical structure of P(t-BA-co-GMA) bipolymer was characterized by FTIR which is shown in Figure 3. In the curve of c, all the peaks at 2980 cm⁻¹, 2930cm⁻¹, 1730 cm⁻¹, 1161cm⁻¹, 908 cm⁻¹ and 842 cm⁻¹ exist. These demonstrate the characteristic absorption peaks of saturated and unsaturated C-H, ester C=O bond and epoxy group all exist in the product. And the new peaks at 1465 cm⁻¹ and 1365 cm⁻¹ which belong to -CH₂ and -CH appear in curve c. These results confirm the P(t-BA-GMA) bipolymer has been successfully synthesized.

The reflectance spectra of P(t-BA-co-GMA) nanospheres structural colors on polyester fabrics with different mass ratio of t-BA and GMA are shown in Figure 4. The different colors and reflectance curves of P(t-BA-co-GMA) nanospheres on polyester fabrics with different mass ratio of t-BA and GMA may be arisen from the different diameters of P(t-BA-co-GMA) nanospheres to form the different photonic band gap corresponding to different wavelength of electromagnetic waves in the visible range.

The P(t-BA-co-GMA) nanospheres structural colors on polyester fabrics with different mass ratio of t-BA and GMA before and after abrasion are shown in Figure 5. These results show that P(t-BA-co-GMA) nanospheres structural colors on polyester fabrics possess good abrasion colorfastness.

The washing colorfastness of the structural colors polyester fabrics is shown in Figure 6. These results also demonstrate the P(t-BA-co-GMA) nanospheres structural colors on black polyester fabrics have good washing colorfastness.

Conclusions

In this study, the P(t-BA-co-GMA) bipolymers containing reactive epoxy groups with different mass ratio of t-BA and GMA were successfully synthesized. P(t-BA-co-GMA) nanospheres can self-assembled into short range ordered and long range disordered photonic crystals to present different bright crack-free structural colors on polyester fabrics. The P(t-BA-co-GMA) nanospheres possess excellent monodispersity, and their diameters vary with the different mass ratio of t-BA and GMA to obtain five different colors on black polyester fabrics. The different diameters of the P(t-BA-co-GMA) nanospheres and the arrangement of short range ordered and long range disordered in microstructure may be the reason of different structural colors on polyester fabrics. The P(t-BA-co-GMA) nanospheres structural colors on polyester fabrics possess good abrasion and washing colorfastness. This research provides the experimental basis for the development of polymer photonic crystals containing reactive groups structural color on fabrics with high colorfastness to promote the practical application of structural color in textile colorization.

ABSTRACT

In this paper, we report a graphene-coated Calotropis gigantea yarn (CGY) by pad dyeing with graphene oxide and reduction process, which endows it with high conductivity, outstanding conducting stability, and scale production capacity. By optimizing the pad dyeing, the modified CGYs display high electrical conductivity of 7 S/m. Range analysis results indicate that electrical conductivity of the graphene-coated yarns exhibits strong dependence on the concentration of graphene oxide and pad dyeing cycles. The combination between hydrogen bond of the fiber and the oxygen bond of graphene during dyeing process renders the functionalized yarns stable conductivity to washing and bending. Based on the simple fabrication process, and fascinating performance, the graphene-coated yarns show great potential in flexible wearable electronic devices and large-scale production.

I. Introduction

The explosion of multi-functional flexible wearable electronic textiles in flexible sensors and wearable electronic devices has attracted extensive attention due to their great potential as next-generation electronics with the advantages of lightweight, flexibility, and portability. Compared with other materials, graphene can be much easier to cover along the fiber surface to gain high electrical conductivity.

Calotropis gigantea yarns (CGYs) have received intense attention in recent years due to its unique structure and performance. The functionalization of CGFs by the coating of graphene was not investigated. More importantly, scale production of such graphene-coated CGFs has always been a great challenge, which has not been reported. We report a graphene-coated CGY by pad dyeing, which endows it with not only high performance in conductivity but also scale capacity in production.

II. Method

Pre-treatment of GO: The graphite powders (2 g), NaNO₃ (2 g), and 50 mL of H₂SO₄ (98%) were mixed and kept in an ice bath. For purification, the mixture was washed by HCl and deionized water to obtain GO solution.

Preparation of GO-CGY: The pristine CGYs were firstly immersed into GO solution to make surface fully contact with the GO solution. Then the excess GO solution on the pristine CGYs surface was removed by a rolling mill to obtain continuous structure and full coverage for high-efficiency electron transport.

Reduction of GO-CGY: the GO-coated yarn experienced reduction through being transferred into ascorbic acid solvent (with a weight ratio of 10:1 to GO) at 80°C to acquire rGO-CGYs.

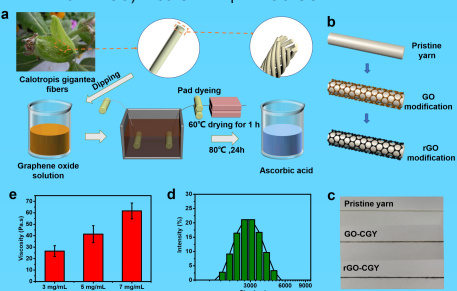


Fig. 1. (a) Schematic diagram of rGO-CGYs through pad dyeing. (b) The illustration of the pristine, GO-modified, and rGO-modified CGYs. (c) The photos of the pristine CGY, GO-CGY, rGO-CGY. (d) The particle size distribution of the GO solution, (e) the viscosity of GO solution.

III. Result and discussion

In order to optimize the experimental parameters, we analyze the GO concentration, pad dyeing cycles, and reduction time in determining the properties of graphene-coated CGYs through an orthogonal design with three factors and three levels. Table 1 shows the sample specifications. We choose the samples with good conductivity (Sample 2, Sample 5, and Sample 8) to present and evaluate their performance, which are denoted as rGO-CGY-4, rGO-CGY-7 and rGO-CGY-10 respectively.

Table 1. The specifications of rGO-CGYs through pad dyeing.

Sample	A	B	C	Additive concentration (mg/mL)	Reduction time (h)	Dipping cycles
1	1	1	1	3	12	4
2	2	3	1	5	36	4
3	3	2	1	7	24	4
4	1	2	2	3	24	7
5	2	1	2	5	12	7
6	3	3	2	7	36	7
7	1	3	3	3	36	10
8	2	2	3	5	24	10
9	3	1	3	7	12	10

The pristine CGY and rGO-CGY-10 in Fig. 2a, b show that the nature-color yarn becomes black after the functionalization. Fig. 2c shows the atomic percentage of C, N and O on the surface of pristine CGY, GO-CGY-10, and rGO-CGY-10. It presents that the atomic percentage of C, N, and O of the pristine yarn is 57.780%, 4.678%, and 37.542% respectively, while that becomes 59.323%, 3.133%, and 37.544% after GO modification. After reduction, the C increases by 61.855%, N and O decrease by 2.536% and 35.609% respectively. Fig. 2d, e, f show the surface morphology of the pristine CGY, GO-CGY-10, and rGO-CGY-10 respectively. Comparing with the smooth pristine CGYs surfaces, the GO-CGY-10 shows rough and uneven surfaces due to the existence of GO layers. Fig. 2(g-o) show the element distribution of the pristine CGY, GO-CGY-10, and rGO-CGY-10 respectively.

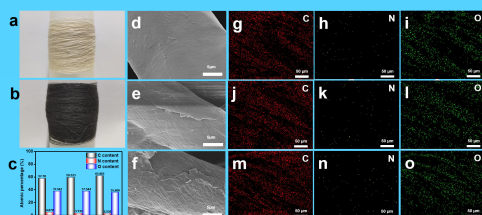


Fig. 2. (a-b) the photos of the pristine CGYs and rGO-CGY-10; (c) the surface element content of CGYs; the surface morphology of (d) the pristine CGY (e) GO-CGY-10, (f) rGO-CGY-10; (g-o) C, N, and O distribution of the pristine CGY, GO-CGY-10, and rGO-CGY-10.

Fig. 3(a-c) shows that the Raman spectra of the pristine CGYs after the functionalization. They all presents the characteristic peaks of graphene, the D-band at 1370 cm⁻¹ (related to defects or heteroatom-doping) and G-band at 1590 cm⁻¹ (attributed to the vibrations of the sp²-bonded crystalline carbon), indicating that graphene wrapped onto the pristine CGYs successfully. In Fig. 3d, the intensity ratios of D-band and G-band increases from 0.9 to 1.2 and the full width at half maximum (FWHM) of the D-band decreases from 71 to 53. These changes indicate that GO-CGYs are chemically converted into rGO-CGYs.

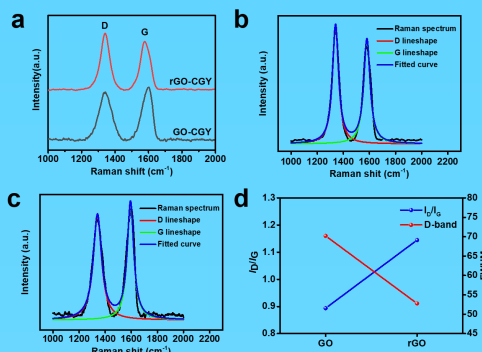


Fig. 3. (a) Raman spectra of the CGYs after the functionalization, (b-c) high-resolution spectrum of Raman spectra of the GO-CGY-10 and rGO-CGY-10, (d) the intensity ratios of D-band and G-band and the full width at half maximum (FWHM) of the D-band for the GO-CGY-10 and rGO-CGY-10.

Fig. 4a shows changes in surface wettability of the pristine CGYs after graphene coating. The contact angles of CGYs increase greatly from around 20° for the pristine CGYs to about 150° for the rGO-CGY-10 cycles. The pristine CGY is hydrophilic material, graphene is the hydrophobic material, when the pristine CGY is coated with graphene, and the corresponding contact angle gradually increases. The typical tensile strain curves of CGYs with various pad dyeing cycles in Fig. 4b exhibit the CGYs possess different mechanical properties. Fig. 4c shows with the increase of pad dyeing cycles, the breaking strength of the CGYs increases from about 168 cN to 195 cN after 10 pad dyeing cycles. Fig. 4d shows the tensile strain of the rGO-CGY-10 has decreased to 4.1% from the pristine CGYs 7.2%. It is obvious that the pad dyeing method can improve the breaking strength of CGYs.

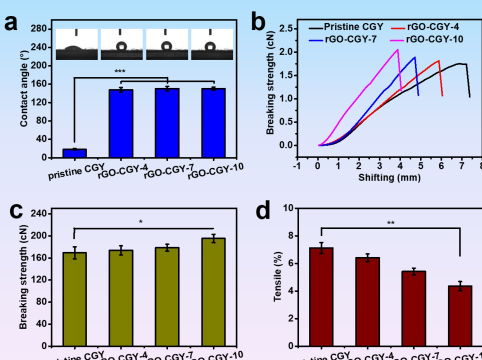
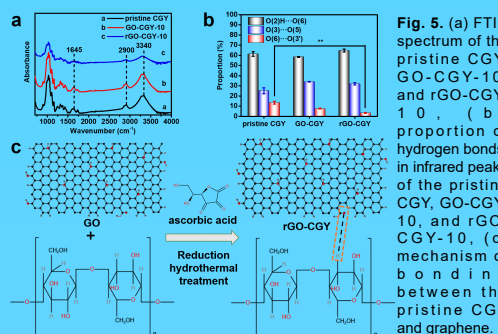
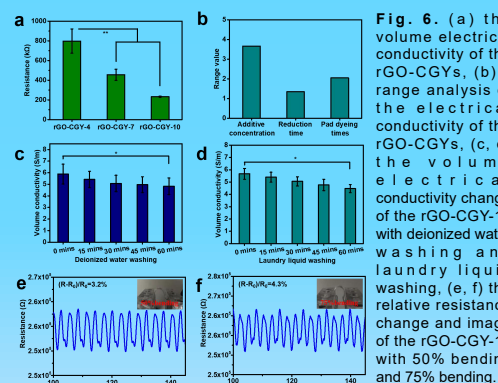


Fig. 4. (a) the contact angle of the pristine CGYs after graphene coating, (b) the stretch curve of CGYs, (c) the breaking strength of the graphene-coated CGYs, (d) the tensile strain of the graphene-coated CGYs.

Fig. 5a presents the FTIR spectrum corresponding to the pristine CGY, GO-CGY-10, and rGO-CGY-10. The peak at 1645 cm⁻¹ (C=O stretching) disappears and the peak at 2900 (asymmetrical C-H stretching) and 3340 (OH stretching) cm⁻¹ become weaker, which implies that GO on the surface of CGY is successfully reduced to rGO after the treatment of ascorbic acid. Fig. 5b shows changes in the characteristic absorption wavenumbers of intramolecular hydrogen bond. It reveals that the content of O(6)···O(3') in CGY decreases during the treatment. Fig. 5c shows the binding mechanism between the pristine CGY and graphene, which shows that oxygen bond and III are mainly combined in the reduction process.



The Fig. 6a shows that the electrical conductivity of rGO-CGY-10 is obviously improved and exhibits high electrical conductivity of 7 S/m. The range value of the additive concentration of GO solution (Fig. 6b) is 3.665. Therefore, the electrical conductivity of rGO-CGYs depends largely on the additive concentration of GO solution. Fig. 6(c, d) shows that the volume conductivity of the rGO-CGY-10 still maintains a high level when yarns are washed with deionized water and laundry liquid for 60 mins. The relative resistance change of the rGO-CGY-10 with 50% bending and 75% bending in Fig. 6(e, f) show that CGY has a very limited response to bending, which means that the graphene-coated CGYs have certain anti-interference performance to bending and shows great potential in flexible wearable electronic devices.



IV. Conclusions

In this work, we report a conductive CGY through pad dyeing with graphene, showing better mechanical properties, mass production, high performance and excellent stability in conductivity. The pad dyeing for preparing conductive CGYs can be rapidly extended to almost any other yarns, paving a new way for developing large-scale production, low-cost, and high-performance conductive yarns.

V. Acknowledgements

This work was supported by National Key R&D Program of China (SQ2020YFE010170) and (2019YFE0117700) and the joint scientific research project of Sino-foreign cooperative education platform of Jiangsu Higher Education Institutions (5011500720). The authors would like to thank for the support of China National Textile and Apparel Council (J202002); Nature Science Foundation of Jiangsu, China (BK20191191).

VI. References

[1] Fang M H, Xiong X H, Hao Y B, Zhang T X, et al., (2019) Preparation of highly conductive graphene-coated glass fibers by sol-gel and dip-coating method. Journal of Materials Science & Technology. 35(9):1989-1995
[2] Liu Z K, Zheng Y, Jin L, Chen K L, et al., (2021) Highly Breathable and Stretchable Strain Sensors with Insensitive Response to Pressure and Bending. Advanced Functional Materials. 31(14)

引言

棉织物作为使用最广泛的天然纤维之一，因其舒适、透气和柔软等优点而被用于服装、床上用品和装饰纺织品。然而，天然纤维素纤维有其自身的缺陷，如高的易燃性、易起皱等。棉织物的极限氧指数LOI为18%左右，属于可燃材料。棉织物在穿着和反复洗涤过程中容易形成折皱，会对服装外观产生很大影响。因此，提高棉织物的阻燃和抗皱性能对其安全性和舒适性非常重要。

最有效和最常见阻燃剂是含卤和含磷化合物。然而，含卤阻燃剂在燃烧过程中可能会产生有毒和腐蚀性气体而被限制使用。因此，无卤阻燃剂受到越来越多的关注，磷系阻燃剂被认为是最有希望的替代品之一。棉织物上广泛使用的持久含磷阻燃剂是“Pyrovatex CP”，其含有可与羟基反应的活性N羟甲基。然而，其在甲醛的释放问题，会对人体健康造成损害。膨胀阻燃体系(IFR)作为绿色阻燃剂之一，越来越受到人们的重视，在近几十年来更受关注。特别是源于植物和动物的生物基化合物已被探索用于构建膨胀阻燃体系。生物大分子已被研究用作新型绿色阻燃剂，如壳聚糖、DNA、酪蛋白、乳清蛋白、核酸、香蕉假茎汁液、石榴皮提取物和椰子壳提取物。特别是生物基植酸和壳聚糖已被广泛研究。植酸主要来源于植物的种子、根和茎，由于其磷含量高，已被用作有机磷阻燃剂。植酸作为一种绿色、可再生、可持续的天然阻燃剂，已有报道用于棉、丝和毛织物的阻燃剂。壳聚糖来源于动物壳中几丁质的部分脱乙酰。壳聚糖因含有丰富的碳和氮元素而被用作构建IFR的氮源和碳源。

甲醛基化合物可通过N-羟甲基与纤维素纤维中的羟基发生交联反应被广泛用于抗皱整理剂，例如二羟甲基二羟基乙烯脲(DMDHEU)。甲醛基抗皱整理剂大大提高了棉织物的抗皱性能，但也存在甲醛释放的问题。自20世纪90年代以来，人们对纤维素织物的无甲醛抗皱剂进行了广泛的研究。自Welch报道多元羧酸高效催化剂次磷酸钠以来，多元羧酸被认为是最有前途的替代品之一。1,2,3,4-丁烷四羧酸(BTCA)是最有希望取代甲醛类抗皱剂的多元羧酸产品。近年来，多功能棉织物受到越来越多的关注。有报道多元羧酸和纳米氧化锌已被研究用于制备阻燃和紫外线防护棉织物。全生物基IFR与多元羧酸复合用于棉织物的环保阻燃和抗皱多功能整理尚未见报道。本研究以植酸和壳聚糖为原料，构建纯生物基IFR体系，并与生态友好型多元羧酸BTCA用于改善棉织物的阻燃和抗皱性能。

实验过程

材料

植酸(PA, 70% H₂O溶液)、BTCA和次磷酸钠(SHP)购自阿拉丁试剂有限公司(中国上海)。壳聚糖(CS, 脱乙酰度:80-95%)购自国药化学试剂有限公司(中国上海)。漂白纯棉机织物(105g/m²)购自东莞云帆有限公司(中国广东)。

棉织物的复合多功能整理

将壳聚糖加入到去离子水中，然后搅拌24小时以制备0.5%壳聚糖溶液。在去离子水中加入BTCA 63g/L和SHP50g/L，制成抗皱整理液。在抗皱整理液中加入不同质量浓度的PA，制备BTCA/PA复合溶液。棉织物在CS溶液中浸泡2 min，经轧车轧压(带液率90-100%)后，在85℃的烘箱中烘干3 min。然后将其浸入BTCA/PA复合溶液中2 min，然后轧车轧压(带液率90-100%)，并在85℃下干燥3 min。处理后织物在160℃焙烘3 min。多功能改性的具体过程如图1所示。

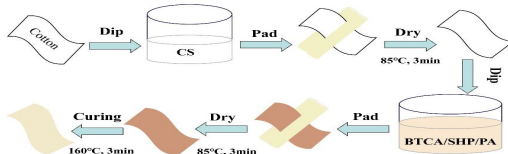


图1 复合多功能改性示意图

性能表征

棉织物改性前后的傅里叶变换红外光谱由 Thermo Nicolet Avatar 6700红外光谱仪(Thermo Electron, 美国)测定。采用LOI法和垂直燃烧法测定多功能改性棉织物的阻燃性能。参照GB/T 5454—1997《纺织品 燃烧性能试验 氧指数法》测试标准，在室温下用氧指数仪器(JF-3, 江宁分析仪器)测定LOI值。参照GB/T 5455—1997《纺织品 燃烧性能试验 垂直法》测试标准，采用织物阻燃性能测试仪(YG(B)815D-1, 温州大荣)测定垂直燃烧性能。棉织物阻燃耐久性测定洗涤程序参照AATCC 61-2006，改性棉织物用2g/L合成洗涤剂在49℃洗涤45分钟相当于普通家庭洗涤5次。参照AATCC 66标准，采用YG 541E全自动激光织物折皱弹性测试仪(温州方圆)上测定折皱回复角。参照ASTM D5034标准，采用YG(B) 026G电子织物拉伸测试仪(温州大荣)测定拉伸断裂强度。采用WSB-3A白度测定仪(中国温州鲁东)测定改性前后棉织物白度。棉织物的硬挺度参照ASTM D 1388-96 (2002)标准，采用YG(B) 022D自动织物挺度测试仪(温州大荣)测定。所有样品在恒温、恒湿(±2±2℃, 65±5%相对湿度)下平衡24小时以上。

结果和讨论

棉织物的表面红外表征和形态

从图2可以看出，原棉织物的红外光谱在3420 cm⁻¹、2900 cm⁻¹、1642 cm⁻¹、1427 cm⁻¹、1365 cm⁻¹和1160 cm⁻¹处存在特征吸收峰。这些吸收峰都存在于改性棉织物的光谱图中，改性棉织物出现了新的吸收峰。1725cm⁻¹处的新峰归因于BTCA和纤维素的羟基通过酯化交联反应形成的C=O(酯基)。1340 cm⁻¹处的新峰被认为是-CO-NH-特征峰，这可能是由于在壳聚糖和BTCA之间形成了CO-NH键。1120、1060和987 cm⁻¹处的新峰归属于P=O、O-P-C和P-O键的特征吸收峰。这些结果表明，BTCA已经与纤维素大分子和壳聚糖共价交联，PA也已成功应用于棉织物。如图3所示，改性前棉纤维表面光滑平整。然而，先用0.5%壳聚糖溶液改性，再用BTCA/PA(的质量浓度为10%)复合溶液改性后的棉纤维表面变得粗糙，略有溶胀。改性棉纤维上覆盖了一层涂层。因此，这些结果表明，BTCA和PA的功能剂不仅成功地应用于棉织物表面，而且在多功能改性后渗透到棉纤维内部。

棉织物的阻燃抗皱性能

如表1和图4所示，改性后棉织物的阻燃性大大提高，当BTCA/PA复合溶液中PA用量为6%时，改性棉织物的LOI值达到27%左右。随着PA的用量和改性棉织物的加上量增加，LOI值增加。当复合溶液中PA的用量为10%时，LOI值达到30%以上。对于垂直燃烧性能，改性棉的炭长随着PA的用量从4%到10%逐渐减少。未改性棉织物燃尽，而10%PA的复合整理液改性棉织物的炭长减少至9.6cm。当复合溶液中PA的用量大于10%时，改性棉织物的炭长不再减少。当复合溶液中PA的用量大于6%时，续燃时间和阴燃时间均为0s。因此，当复合溶液中PA的用量大于10%时，多功能改性可赋予棉织物优异的阻燃性能。改性棉织物经5次水洗后的LOI值大幅降低至22.8%，但多功能改性棉织物经燃烧后会形成较多残炭，有利于其阻燃。表1也列出棉织物的折皱回复角。未改性棉织物的折皱回复角仅为165°，改性棉织物的折皱回复角均达到260°左右，表现出优异的抗皱性能。植酸用量为4%到10%时，不会影响改性棉织物的折皱回复角。当BTCA/PA复合溶液中PA的用量为12%时，折皱回复角略有下降。因此，经过多功能改性后，改性棉织物的抗皱性能得到明显改善。改性棉织物经5次洗涤后的折皱回复角仍保持在250°以上，表明其抗皱性能具有优异的耐水洗性。同时也证实了BTCA与棉织物之间已经形成共价键。从表1可以看出，改性棉织物的拉伸断裂强度会明显降低，当PA用量为10%时，多功能改性棉织物的强力保留率不到50%。当PA用量高于12%时，拉伸断裂强度会继续降低。改性棉织物拉伸断裂强度的降低可能是由于BTCA和PA的强酸性，以及BTCA与纤维素大分子的交联反应，强酸性会导致纤维素的降解，增加棉纤维的脆性；纤维素大分子的交联反应抑制了分子链的运动，导致拉伸断裂强度的降低。改性棉织物的弯曲长度随着改性棉织物加上量的增加而逐渐增加，表明其硬挺度增加，手感受到影响。与未改性棉织物相比，所有试样的弯曲长度都增加不超过20%，表明多功能改性对棉织物手感的影响较小。从表1中还可以看出，当PA的用量低于10%时，棉织物的白度受多功能改性的影响较小。因此，对棉织物进行多功能改性可以获得优异的阻燃和抗皱性能。

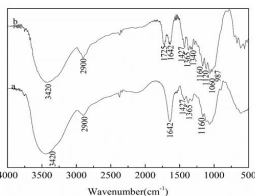


图2 改性前后棉织物的红外光谱图

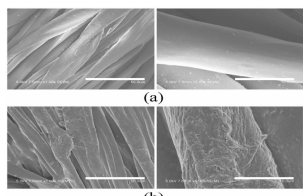


图3(a)未改性和(b)改性的棉织物的表面形态

表1 改性前后棉织物的阻燃性、折皱回复角、力学性能和物理性能

试样	加上量 (%)	LOI	垂直燃烧测试		折皱回 复角 (°)	拉 伸 强 力 (N)	弯 曲 度 (mm)	白 度	
			长炭 (cm)	续燃 时间 (s)					
未处理	0	18.0	燃尽	7.0	25.6	166	525	25.8	82
CS-PA4	9.31	25.8	燃尽	6.5	0	261	304	27.6	80
CS-PA6	12.86	26.8	12.0	0	0	265	268	29.1	77
CS-PA8	14.47	28.3	11.2	0	0	258	250	29.6	76
CS-PA10	16.96	30.8	9.6	0	0	262	251	29.7	76
CS-PA12	18.08	31.8	10.0	0	0	253	223	31.1	73
CS-PA10 [*]	-	22.8	燃尽	6.8	13.5	259	234	28.5	75



图4 垂直测试后未改性和改性棉织物的图片

结论

本研究利用生物基植酸、壳聚糖和生态友好型多元羧酸BTCA，通过简单的两步后整理工艺对棉织物进行阻燃抗皱多功能改性。LOI和垂直燃烧结果表明，改性棉织物的LOI值超过30%，改性后棉织物的炭长减少到10cm以下，无续燃和阴燃，多功能改性棉织物可获得优异的阻燃性。多功能改性棉织物的折皱回复角超过260°，表现出优异的抗皱性能。本研究为利用生物基化合物和环保型多元羧酸对天然纤维素纤维进行多功能改性提高其阻燃和抗皱性能提供实验基础。

Development of thermoplastic epoxy filaments with shape memory properties

Baoji Hu¹, Hong Xia², Fan Liu³, Qing-Qing Ni²

1. Interdisciplinary Graduate School of Science and Technology, Shinshu University, Ueda 386-8567, Japan

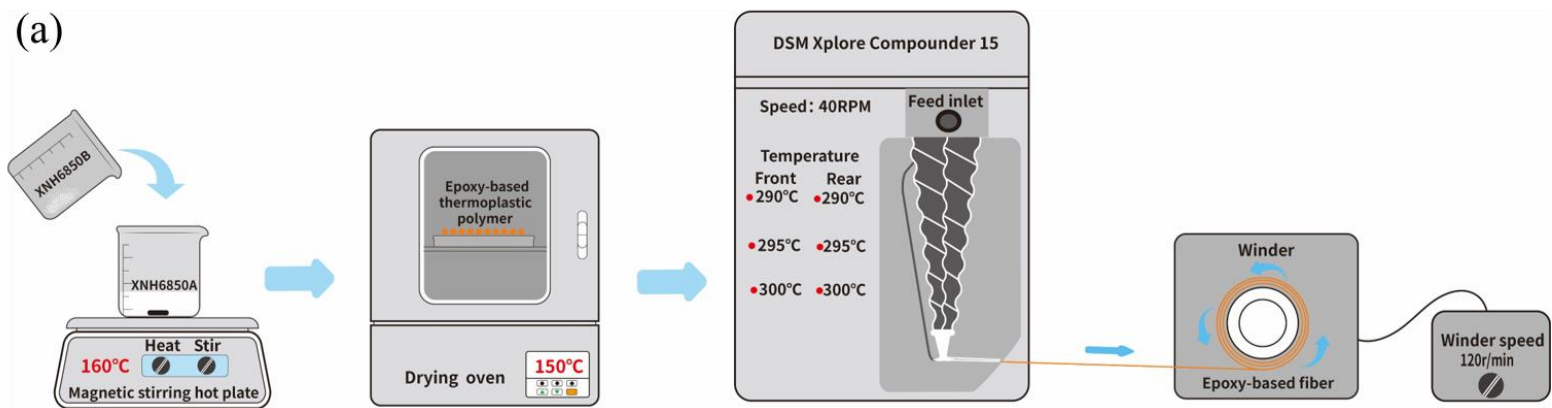
2. Department of Mechanical Engineering and Robotics, Shinshu University, Ueda 386-8567, Japan

3. Textile and Clothing Industry Research Institute, Zhongyuan University of Technology, Zhengzhou 450007, Henan, China

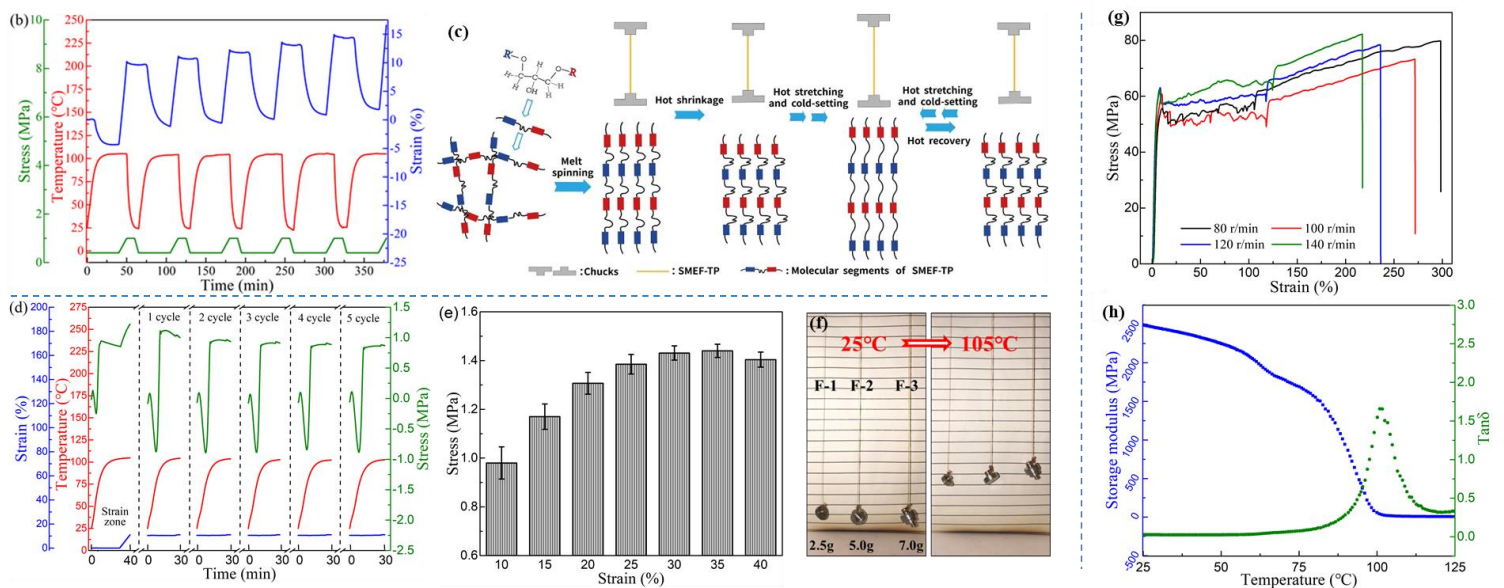
Introduction

In this research, an epoxy resin mixture composed of epoxy and phenol monomers is used to prepare thermoplastic epoxy polymer (EP-TP) through a curing reaction and shape memory thermoplastic epoxy filament (SMEF-TP) was successfully developed for the first time through a melt-drawing process. The developed SMEF-TP shows excellent shape memory performance and thermal actuation capability, which provides huge application potential in the fields of soft actuators, artificial muscles, and smart textiles.

Experimental process



Results and discussion



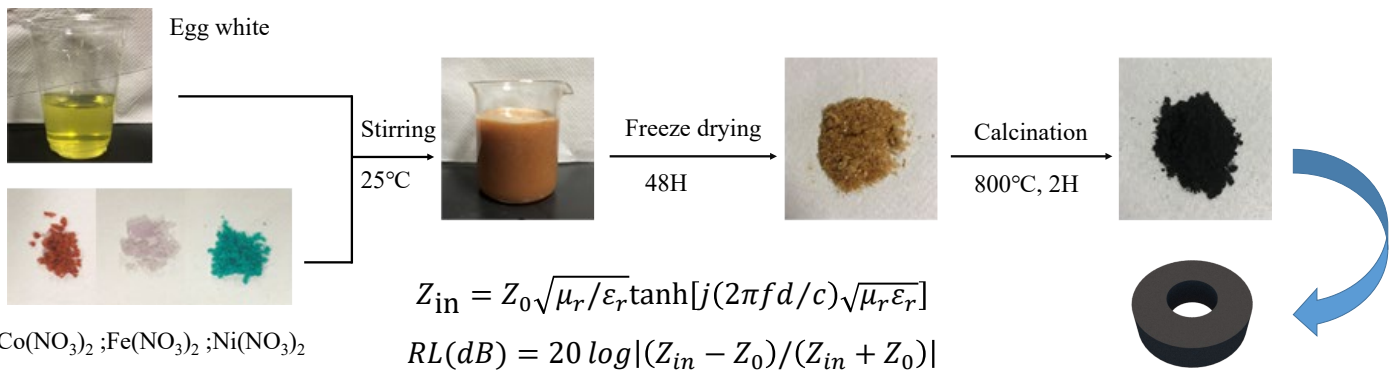
Conclusions

Through shape memory experiments, it is revealed that the SMEF-TP has excellent shape memory performance. The shape fixation rate can reach 97%, shape recovery rate can reach more than 97%, and cyclic test showed good stability. The shape recovery stress of SMEF-TP was further tested to show that it can stably respond to temperature, and the shape recovery stress increases with the increase of strain, reaching 1.45 MPa at a strain of 35%.

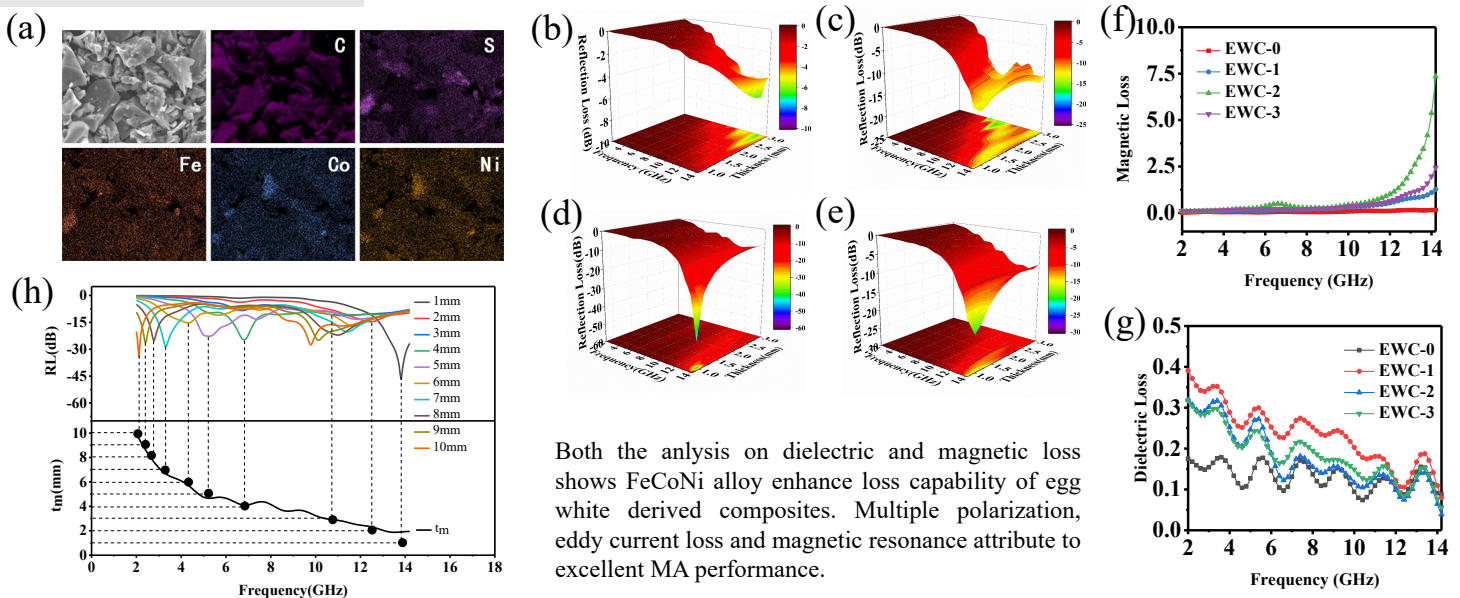
Introduction

The rapid development of electronic equipment, and wireless communication has caused severe electromagnetic pollution. Carbonaceous materials such as graphene, carbon nanotubes, and hollow carbon spheres exhibit tremendous potential as microwave absorption materials. However, pure carbon materials suffer from single loss mechanism and poor impedance matching. Egg white is a sustainable biomaterial containing C, S, O, and N. Herein, we aim to explore a simple and low-energy method for fabricating egg-white-derived microwave absorption (MA) materials for use in two main steps: mixture and pyrolysis. This study is the first to consider egg white as a source for carbon and sulfur; in addition, Co^{2+} , Ni^{2+} , and Fe^{3+} are chosen as additives to form magnetic components.

Experimental process



Results and discussion



Conclusions

- The S-doped carbon flake possesses multiple polarization relaxations but poor impedance matching, leading to low microwave absorption performance with an RL value of less than -10 dB.
- When regulating amount of FeCoNi alloy in S-doped carbon, a strong microwave absorption intensity (-47.09 dB at 13.8 GHz) while the thickness is 1 mm.
- The moderate polarization relaxation and conductive loss in dielectric and obvious natural resonance in magnetic loss result in enhanced MA performance.

Introduction

BaTiO₃ (“BTO” for short below) is one of the widely used typical piezoelectric materials. As is widely known, BTO is an artificial mineral and does not occur in nature, so it has various forms depending on the synthetic method. In recent years, nanostructured materials have received a great deal of attention because of their unique shape and size, which allows them to combine multiple types of materials to create new materials with innovative properties. In this study, uniform BTO nanoparticles were synthesized via a simple wet chemical route at low temperature (50 °C and 65 °C). This study describes possible synthetic mechanisms of BTO nanoparticles.

Experimental Process

BTO Synthesis Mechanism

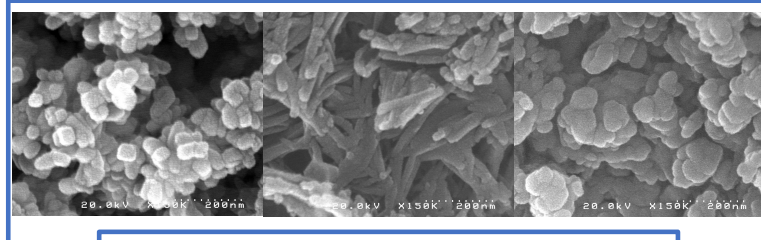
- ① $\text{TiO}_2 + 2\text{NaOH} \rightarrow \text{Na}_2\text{TiO}_3 + \text{H}_2\text{O}$
- ② $\text{Na}_2\text{TiO}_3 + 2\text{HCl} \rightarrow \text{H}_2\text{TiO}_3 + 2\text{NaCl}$
- ③ $\text{H}_2\text{TiO}_3 + \text{Ba}(\text{OH})_2 \cdot 8\text{H}_2\text{O} \rightarrow \text{BaTiO}_3 + 10\text{H}_2\text{O}$

① TiO₂ powder was added to 10 M NaOH aqueous solution and magnetic stirred at room temperature for 12 h. Next the mixed suspension was transferred into Teflon lined autoclave, and the autoclave was then sealed and placed in oven and heated to 150 °C, for 48 h. The newly formed white suspension was separated from the liquid by centrifuge and washed with deionized water.

② The newly formed white precipitate was magnetic stirred with 0.1 M HCl aqueous solution for about 1.5 h to exchange Na⁺ with H⁺. Afterward, the treated sample was washed repeatedly with distilled water until the pH level was almost neutral. Finally, the resulting white precipitate was dried under vacuum at 50 °C for 24 h.

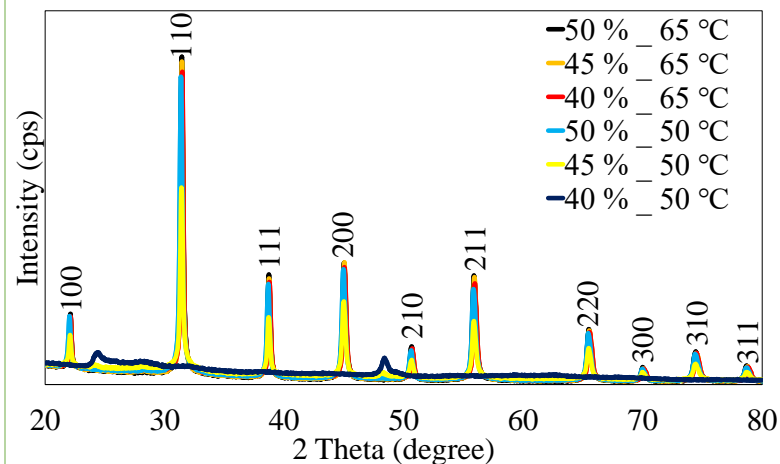
③ The prepared H₂TiO₃ and Ba(OH)₂·8H₂O was added to ethanol/water mixed solvent in a beaker. Afterward, the beaker was put into water bath for 4 h under magnetic stirring. After the reaction was completed, the beaker was taken out. The resulting product was washed sequentially with 0.1 M formic acid, ethanol, and distilled water. Finally, the final product was dried under vacuum at 50 °C one day for further characterization.

Results and Discussion



FE-SEM Images of TiO₂, H₂TiO₃ and BaTiO₃.

TiO₂ was obtained from Sigma-Aldrich Co. LLC. The FE-SEM image shows that it were nanoparticles. After steps ① and ② described in the previous section, the H₂TiO₃ nanotubes were obtained and can be seen from the FE-SEM image. After completing the final task ③, the BTO nanoparticles were obtained. The experimental conditions were ethanol/water mixed solvent with 50 % ethanol by volume, and the temperature of the water bath was 50 °C.



This figure shows the X-ray diffraction (XRD) pattern of BTO nanoparticles synthesized by the above method. In the figure, % means ethanol volume ratio of the ethanol/water mixed solvent, and °C means water bath temperature.

Conclusions

The results of the XRD analysis present all diffraction peaks can be labeled and assigned to the cubic crystal structure of BTO, and the lattice constant is indexed as a = 4.031 Å; b = 4.031 Å; c = 4.031 Å, which exactly match the reported data (JCPDS Powder Diffraction File Card No. 31-0174). In this study, BTO nanoparticles were successfully synthesized by a simple process at low temperature. It was found that the ethanol volume ratio of the ethanol/water mixed solvent and the water bath temperature play important roles in the synthesis. When the water bath temperature was 50 °C, the ethanol concentration (40 %, 45 %, 50%) had a great effect on the crystallinity. On the other hand, when the water bath temperature was 65 °C, there was no significant difference in crystallinity due to the change in ethanol concentration (40 %, 45 %, 50%).

Electromagnetic waves propagation in carbon fiber composites

Pham Hoang Quang Duy and Qing-Qing Ni
National Shinshu University, Nagano, Japan

Introduction

In recent years, the electronic innovation (gadgets) has been expanding in the assembling business and the data business. This expands the odds of openness to electromagnetic waves. Since electromagnetic waves may influence human wellbeing, the researches on electromagnetic protecting materials become more and more significant. This study utilizes the finite element analysis of dynamic electromagnetic wave (EMW) propagation to investigate the impact of EMW in various carbon fiber composites. The results obtained may give a guidance of designing optimal EMW shielding materials for protecting human life and electric devices.

Simulation process

→ On the Vector Network Analyzer, S_{11} , S_{21} , S_{22} , S_{12} shown in Fig. 1 can be obtained in decibels.

Reflectivity:

$$R = |E_r/E_i|^2 = |S_{11}|^2 (= |S_{22}|^2)$$

Transmission rate:

$$T = |E_t/E_i|^2 = |S_{21}|^2 (= |S_{12}|^2)$$

Absorption rate:

$$A = 1 - R - T$$

Specific Absorption Rate:

$$A_{\text{eff}} = (1 - R - T) / (1 - R)$$

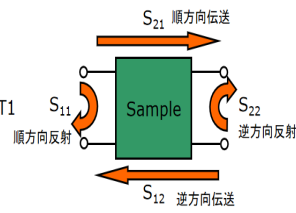


Fig. 1. S-parameters

Calculation of shielding effect SE (dB)

$$\text{EMI SE} = \text{SE}_R + \text{SE}_A + \text{SE}_{\text{MR}}$$

$$\text{EMI SE} = \text{SE}_R + \text{SE}_A + \text{SE}_{\text{MR}}$$

$$\text{SE}_R = -10 \log(1 - R)$$

$$\text{SE}_A = -10 \log(1 - A_{\text{eff}})$$

$$= -10 \log(T / (1 - R))$$

Modeling the sample

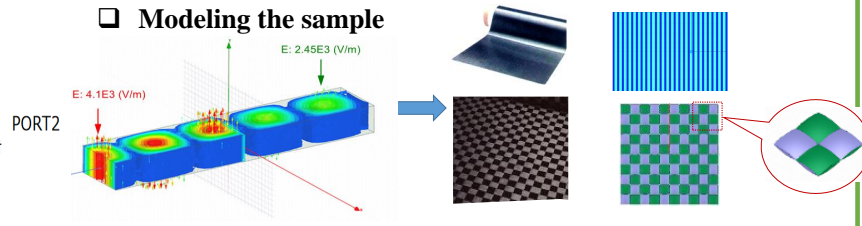


Fig. 2. The models of unidirectional CFRP and Carbon fiber fabric

→ The EMW analysis model comprises of three sections. Two air parts on the two sides of the material sample, the incident EMW propagates through the sample and the transmitted EMW is obtained and analyzed.

→ Material models as shown in Fig. 2. CFRP comprises of two sections, resin part and fiber part. Changing the property of the material, structures, may result in different EMW performance.

Results and discussion

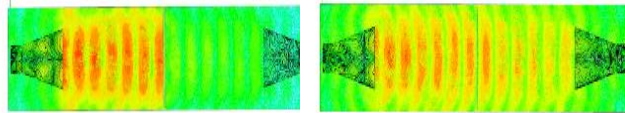


Fig. 3. Electric field propagation when fiber direction relative to the direction of electric field oscillation is 0 and 90 degrees, respectively.

→ In this work, electromagnetic waves are propagated from the left side and sent to the right side. On account of the model with 0° fiber orientation, the fiber direction is the same with the electric field vibration, so the electromagnetic wave was shielded obviously, that is the EM interference effectiveness (SE) is large, while for the model with 90° fiber orientation the SE value is confirmed being small. It is found the SE of electric field deeply depends on carbon fiber orientation in unidirectional CFRP composites.

→ In Fig. 4, the SE of the single-layer carbon fiber texture is 50 dB. By sandwiching a layer of Teflon between the two layers of carbon fiber texture, a more steady protecting material is obtained, and its SE value reached to 60 dB, while a model with one layer of carbon fiber texture coated by 0.05 mm copper layer shows a comparable result of 63 dB. The models made of two layers of carbon fiber fabric sandwiched by inserting a metal plate, such as, copper or and aluminum achieved fantastic electromagnetic wave performance. The one layer carbon fiber fabric coated by nickel and copper, 0.05mm, in both side, respectively, its SE value reached to 70 dB. The results indicated the EM shielding effectiveness is designable and controllable, and can be predicted by simulation analysis.

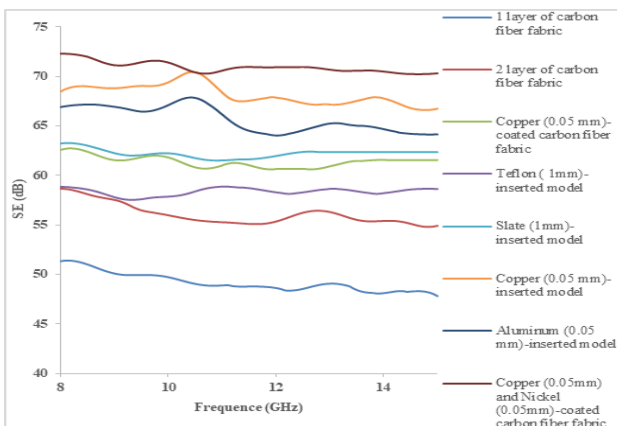


Fig. 4. Thickness effect of carbon fiber fabric

Conclusions

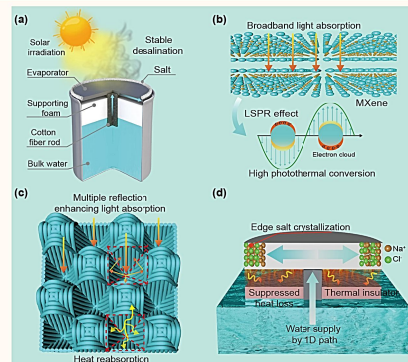
→ The electromagnetic wave shielding effectiveness (SE) of unidirectional CFRP material is analyzed and predicted by finite element analysis. The results indicated the SE value depends on fiber orientation deeply, an obvious anisotropic EM shielding performance is confirmed by this simulation approach.

→ Various models with carbon fiber fabric, multi-layer or coating with a thin layer of metal and/or sandwich structures, it is shown that the EM shielding effectiveness is designable and controllable. By coating two layer of metal, copper and nickel, the SE value reached to 70 dB. All of the results show that the proposed the simulation analysis of electromagnetic wave propagation is an effective way to analyze and predict the EMW performance in CFRP composite materials.

研究背景及意义

如今, 人口增长与淡水短缺之间的矛盾已成为21世纪最具挑战性的问题之一。太阳能作为最大的可再生和可持续能源资源, 通过太阳能光热技术驱动界面蒸气蒸发在海水淡化、废水净化和蒸汽灭菌等方面有多种应用。

我们创新提出了将毫米级蜂窝状结构的3D蜂巢织物与新型光热转换材料MXene结合设计高效的太阳能蒸汽产生装置。本研究通过综合优化光吸收、热管理、水输送、盐阻等方面, 实现了不同功能层的协同作用, 达到了高效的水蒸发和盐采集, 为便携式和可扩展的太阳能蒸汽产生的规模化应用提供了新思路。



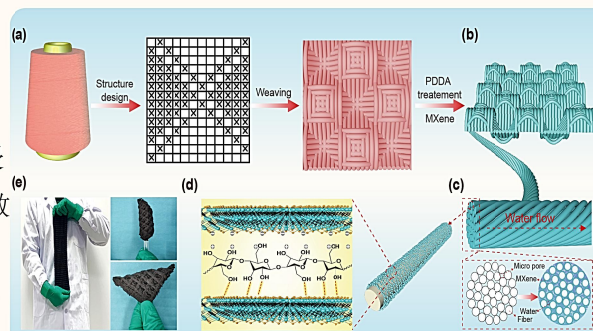
实验

蜂巢织物的织造: 蜂巢织物在半自动编织样品机上通过经纬交织法编织。

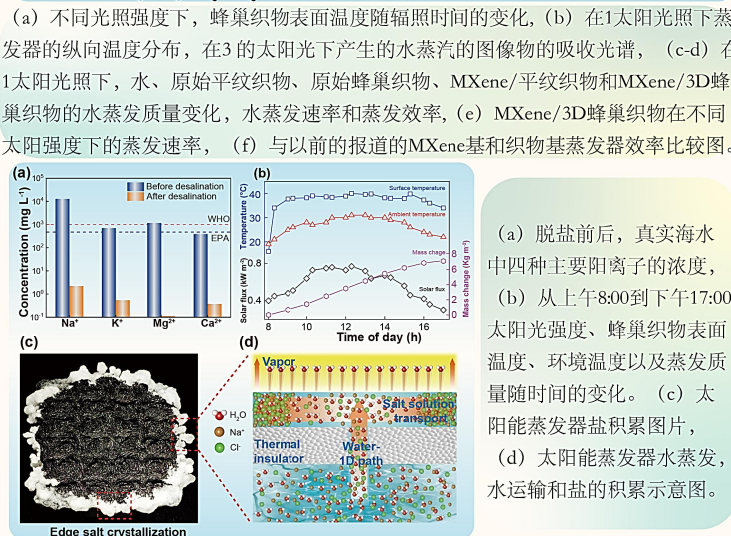
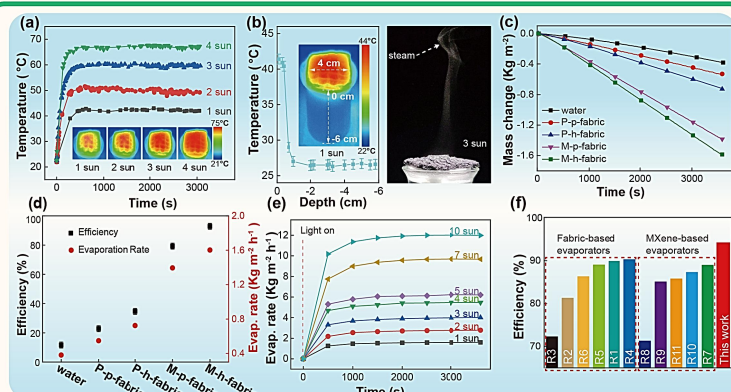
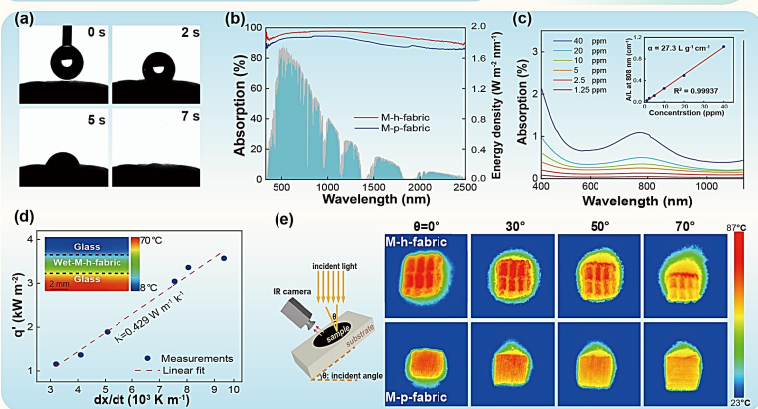
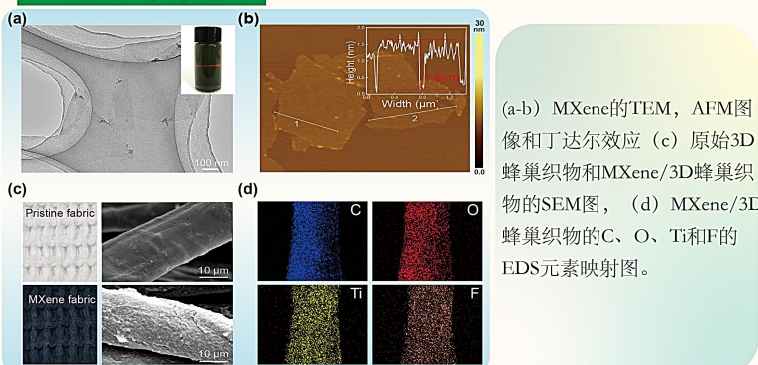
MXene的合成: $Ti_3C_2T_x$ (MXene) 是通过用LiF/HCl混合溶液蚀刻 Ti_3AlC_2 (MAX相) 的铝层获得的。

MXene改性蜂巢织物的制备: 将预清洁的纤维织物浸入PDDA溶液中并浸泡一定时间以进行表面改性, 然后将经过阳离子涂覆的织物浸入MXene分散液中, 干燥后得到MXene改性的蜂巢织物。

太阳能蒸气产生实验: 使用带有AM 1.5G滤光片的太阳能模拟器对太阳辐射进行模拟, 使用电脑连接的电子天平(精度0.1 mg)来实时测量的质量变化。



结果与讨论



结论

我们开发的基于MXene修饰的具有周期性凹形蜂窝结构排列的3D蜂巢织物的蒸发器, 可以达到约96%的光吸收率, 在1个太阳下实现约93.5%蒸发效率, 蒸发速率为 $1.62 \text{ kg m}^{-2} \text{ h}^{-1}$, 同时实现对盐的收集。此外, 在25次循环和连续35个小时的海水蒸发过程中, 通过在空间上将盐结晶与水蒸发表面隔离, MXene/3D蜂巢织物蒸发器的蒸发速率保持稳定, 呈现出优异的长期使用稳定性和可重复使用性。



PVP基碳/二硫化钼纳米纤维 复合材料的制备与分析

刘英琦 周惠敏
新疆大学 纺织与服装学院

引言

随着电子产品的轻量化、便携式甚至可穿戴性的快速发展，对具有优良电化学性能的柔性电池负极材料的需求越来越大。二硫化钼就是其中一种性能优良的电池负极材料。但是目前可负载二硫化钼的碳基体的得碳率不够高，也少有一维柔性的碳基体。

我们设计并制备了一种新型的碳基体，然后在表面负载上水热合成的二硫化钼。我们制备了PVP-碘纳米纤维，然后将其进行碳化处理，得到无定型碳纳米纤维。通过实验发现，使用了PVP作为碳纳米纤维的前驱体，并且采用PVP/碘-静电纺杂化纳米纤维的方法，使得PVP的得碳率得到改善，同时也极大地简化了实验步骤。然后我们通过水热合成法制备了二硫化钼前驱体，并且将其负载在PVP基碳纳米纤维上，调整前驱体浓度，得到二硫化钼纳米片分布不同的复合纳米纤维。

实验过程

(1) PVP/碘-静电纺杂化纳米纤维

将一定量的PVP和碘单质溶于DMF制成纺丝液，在16kV，1 mL/h的条件下进行静电纺丝，然后碳化。

(2) 二硫化钼的制备

将一定量的钼酸铵和硫脲溶于水，在高温高压的条件下进行水热反应，然后使用乙醇水溶液洗涤，离心，得到二硫化钼。

(3) PVP基碳/二硫化钼纳米纤维复合材料的制备与碳化

将一定量的钼酸铵和硫脲溶于水。取一定量上述二硫化钼和PVP基碳纳米纤维，在高温高压的条件下进行水热反应。降温后，用乙醇水溶液洗涤，离心，然后在氮气中碳化，得到二硫化钼/碳纳米纤维。

结果和讨论

(1) PVP/碘-静电纺杂化纳米纤维的形貌与结构分析

根据图1所示，PVP-碘复合纳米纤维，纤维整体直径分布在750 nm至1 μm之间。

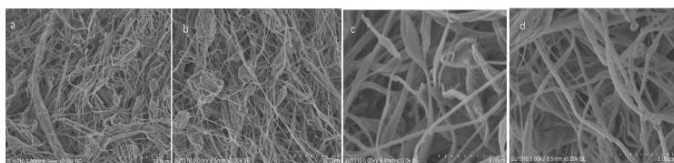


图1 碘-PVP杂化纳米纤维，(a, d) 低倍SEM图像，(c, d) 高倍SEM图像

(2) 二硫化钼的形貌与结构分析

如图2所示，得到二硫化钼的形貌为纳米片组成的微米球状，其形貌比较规则，微米球直径在2-5 μm左右。由高倍SEM可看出其是由不规则的片状组成了球状，片状呈“花瓣”形态，且片层厚度在20 nm左右。此微米球无规则聚集在一起。

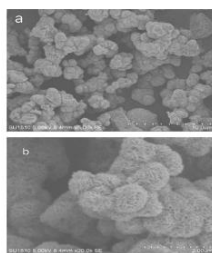


图2 不同倍率下二硫化钼的SEM图像

(3) PVP基碳/二硫化钼纳米纤维的形貌与结构分析

图3 (d) 中的放大SEM图像清楚地显示出纳米纤维是由紧密的MoS₂纳米薄片覆盖，并将复合纳米纤维的直径扩展到约1 μm。10 mg/mL的浓度得到的PVP基碳/二硫化钼纳米纤维中二硫化钼能均匀负载在碳纳米纤维上，是比较理想的负载浓度。

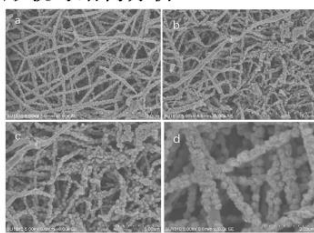


图3 (a, b, c, d) 10 mg/mL浓度的二硫化钼合成的复合纳米纤维的SEM图

图4中曲线b为PVP基碳/二硫化钼纳米纤维的TGA-DTG(热重)图谱，PVP基碳/二硫化钼纳米纤维中MoS₂的负载量通过样品在空气中的热失重反应来测得。可计算出含碳量约为70%，二硫化钼负载约占30%。

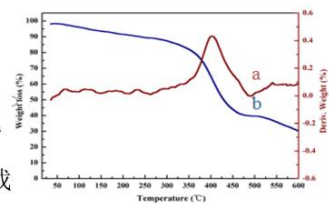


图4 a曲线为PVP基碳/二硫化钼的DTG曲线；b曲线为PVP基碳/二硫化钼的TG图谱

(4) MoS₂和PVP基碳/MoS₂复合材料作为锂/钠离子电池负极的电化学测试

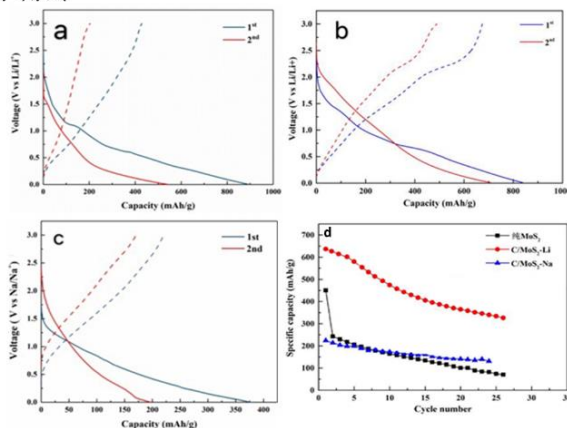


图5 (a) 纯MoS₂为锂离子负极的充放电曲线；(b) PVP基碳/MoS₂复合材料为锂离子负极的充放电曲线；(c) PVP基碳/MoS₂复合材料为锂离子负极的充放电曲线；(d) 不同状态下MoS₂作为钠或锂电池负极材料的循环性能

图5显示，经过测试其初始放电比容量为215mAh/g，20次循环后的放电比容量157mAh/g，以及容量保持率73%，表现出优异的电化学性质。

结论

我们采用静电纺丝法制备了PVP/碘-静电纺杂化纳米纤维，使得PVP碳纳米纤维的得碳率得到改善，同时也简化了实验步骤。我们进一步将水热合成法制备的二硫化钼负载到PVP基碳纳米纤维上，得到PVP基碳/二硫化钼纳米纤维复合材料。将其作为钠离子电池的负极材料，其初始放电比容量为215mAh/g，20次循环后的放电比容量157mAh/g，以及容量保持率73%，表现出优异的性能。

致谢：天山青年计划 (2020Q073)



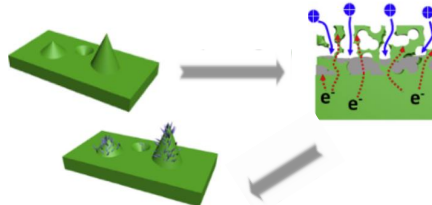
磁控溅射在柔性锌空气电池锌极上的应用

任雪岩, 周惠敏

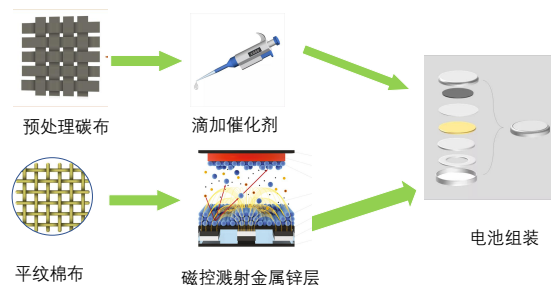
新疆大学, 纺织与服装学院, 新疆 乌鲁木齐 830046

引言

由于锌不均匀沉积在锌阳极表面, 在锌空气电池充放电循环过程中, 枝晶不断生长延长, 最后脱落成为死锌, 甚至可能刺穿隔膜导致电池短路, 导致电池寿命明显缩短。磁控溅射是物理气相沉积(PVD)的一种, 具有镀膜面积大和附着力强等优点, 而通过磁控溅射法在棉布表面溅射金属锌层, 并对溅射锌层后组装成电池的电化学性能的研究却鲜见报道。鉴于此, 本研究以棉布为基材, 利用磁控溅射法在平纹棉织物上溅射金属锌层, 对锌层负载厚度进行调控, 通过观察其表面形态并探索组装成柔性电池后的电化学性能, 探究锌枝晶生长情况, 为提升柔性锌空气电池的库伦效率与循环寿命做出贡献。



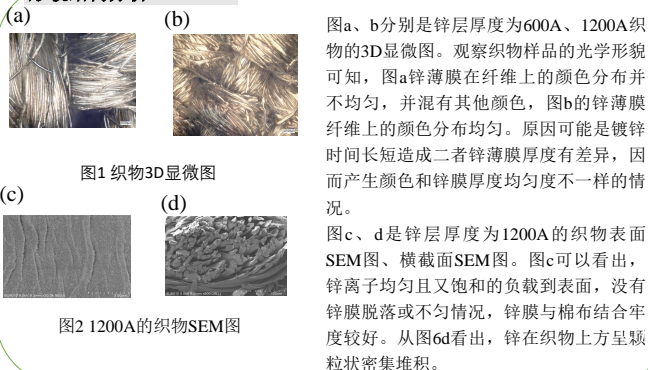
实验过程



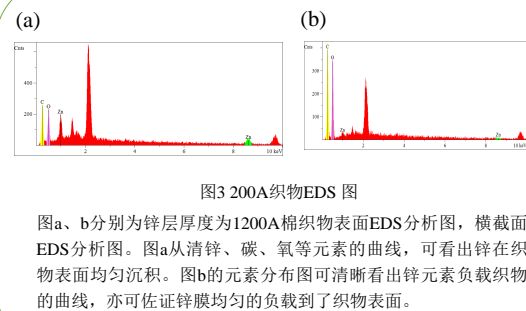
1. 将平纹棉布(经纬密度为74×48)基布剪成半径为5cm的圆形, 用高真空磁控溅射仪溅射金属锌层, 分别镀20min和40min得到薄膜厚度为600A、1200A两种样品。其中仪器功率选择80W, 输入氩气流量80ml/min。
2. 将碳布浸泡在的丙酮和乙醇混合溶液内, 超声处理后用大量去离子水清洗碳布上的丙酮和乙醇, 然后在真空干燥箱内烘干过夜, 以降低其表面附着的胶和油, 随后使用移液枪将碳化处理的普鲁士蓝粉末制成的催化剂浆料逐滴滴加在处理后的碳布上, 随后在室温下静置干燥, 制得空气阴极。
3. 按照负载普鲁士蓝催化剂的碳布、聚乙烯醇—氢氧化钾的凝胶电解质、磁控溅射镀锌的棉织物的顺序逐层组装柔性锌空气电池并测试。

结果和讨论

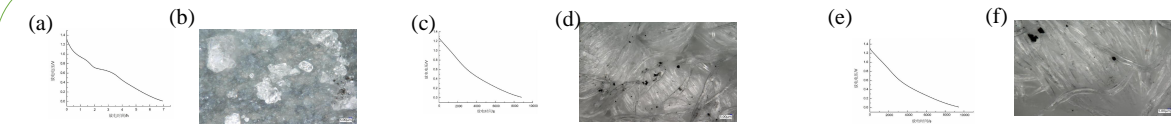
形貌结构分析



表面元素分析



电化学性能分析



图a、图b分别是锌片电极充放电曲线和充放电循环结束后的锌片表面3D显微图。图a可以看出, 电极电池的初始电压为1.3V, 整个放电过程持续7小时。图b显示, 在重复充放电循环后, 锌片表面有几块明显的白色晶体突出, 表明该锌片表面有明显的枝晶生成。

图c、图d分别是600A镀锌棉织物充放电曲线和充放电循环结束后的棉织物表面3D显微图。图c看出, 初始电压在1.25V, 整个放电过程持续了8800s。图d表示, 在进行充放电循环测试后, 织物表面可以出现明显的少量小黑点呈小颗粒状, 分布在纤维表面。但纤维表面光滑平整, 并未有凸起的晶体产生。这表示该镀锌棉织物未产生明显锌枝晶。

图e和图f分别是1200A镀锌棉织物充放电曲线和充放电循环结束后的棉织物表面3D显微图。图e看出, 初始电压在1.3V, 整个放电过程持续了9500s。图f表示, 充放电循环测试结束后, 织物表面出现明显的三块小黑点呈小颗粒状, 但纤维表面光滑平整, 并未有凸起的晶体产生。这表明该镀锌棉织物未产生明显锌枝晶。与600A镀锌棉织物对比, 两者枝晶现象都有明显改善, 但1200A镀锌棉织物电池电压高0.05V, 放电阶段也更为久一些, 这可能与镀膜厚度有关系。

结论

本研究在棉表面进行磁控溅射制备轻量化锌阳极后, 组装类三明治状柔性锌空气电池, 研究电池的电化学性能, 结论如下:

1. 通过改变溅射时间成功调控锌在织物表面沉积厚度, 并且沉积均匀度良好。
2. 组装的电池经电化学测试后, 锌枝晶生长明显改善。

致谢

天山青年计划(2020Q073)

参考文献

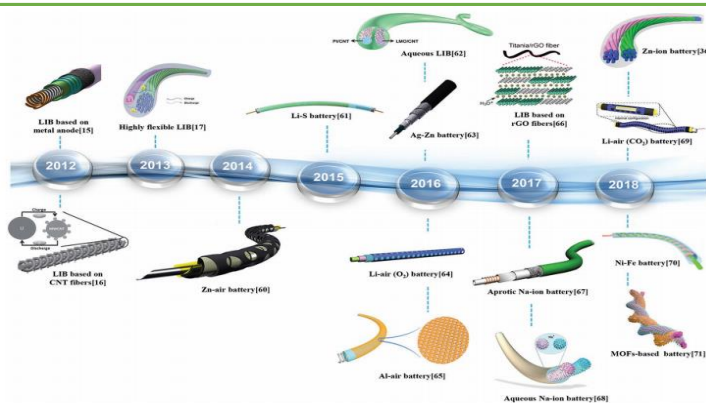
- [1] 朱博, 孟垂舟, 关玉明, 等. 柔性可充电锌空气电池研究进展[J]. 河北工业大学学报, 2020, 49(2): 27-38.
- [2] 翁晓琳, 刘佩佩, 刘江, 等. 锌空气电池研究进展[J]. 电源技术, 2019, 43(4): 716-719.

锌空气电池的柔性自支撑空气阴极

李斌¹, 周惠敏¹, 徐阳²¹纺织与服装学院, 新疆大学, 乌鲁木齐, 新疆, 830046²纺织科学与工程学院, 江南大学, 无锡, 江苏, 214122

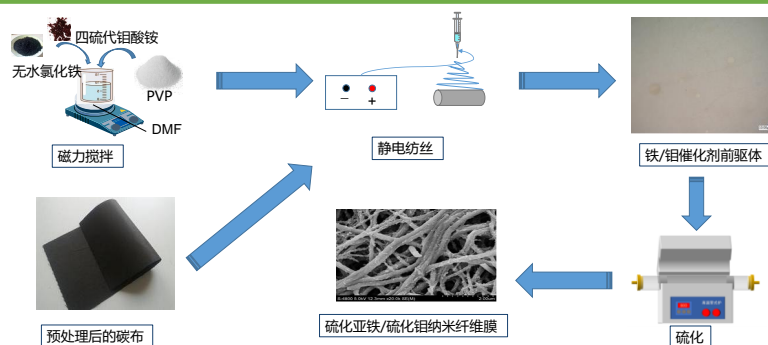
引言

随着柔性电子技术的飞速发展, 智能型可穿戴服装近年来受到了市场的青睐, 然而如何为可穿戴电子设备供电成为实现服装智能化的一大难题。其中金属空气电池具有能量密度高的优势, 且具有安全性高和成本低的特点。锌空气电池所用空气阴极电催化剂多为贵金属催化剂, 其原料具有稀缺性及高成本等特点, 此外, 目前研究中采用的催化剂多是硬度和刚性的结晶粉末, 这些刚性材料被加工到柔性集流体上, 以实现两组分之间的电子传导。这样操作会使催化剂在集流体上的分布难以控制, 降低材料的电导率和堵塞原本设计好的孔隙结构, 最终造成催化剂原本的催化活性得不到完全的发挥。为进一步优化电池结构, 减少界面相, 利用静电纺纱的方法形成一体化空气阴极, 进而以期电化学性能有所改善。



实验过程

1. 碳布预处理: 将碳布浸泡在30°C的丙酮和乙醇的混合溶液内15min后进行超声, 待清洗2~3次后放入60°C的真空干燥箱内烘干。
2. 静电纺丝: 配置15.4 wt.%的PVP/DMF溶液, 称取2.4g无水氯化铁和0.03g四硫代钼酸铵加入溶液共混后, 60°C条件下磁力搅拌24h后进行静电纺丝得到前驱体纳米纤维。电压为18kV, 速率为0.6 mL/h, 接收距离为20 cm, 接收滚筒转速为500 rpm。
3. 前驱体纤维膜硫化: 纤维膜与硫粉质量比为1:3, 升温速率为2 °C/min, 升至600 °C后保温2 h。然后待其自然冷却, 得到一体化空气阴极。
4. 表征测试。



结果和讨论

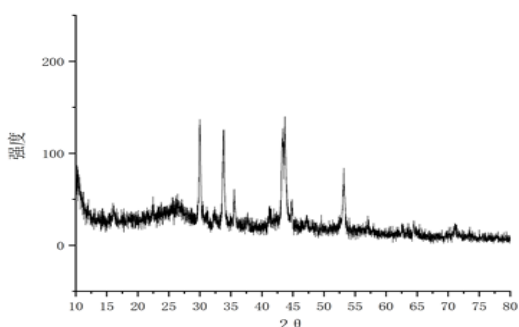


图1 前驱体纳米纤维XRD图

观察图1, 可以看到在30°、34°、46°、57°处的衍射峰较强, 基本符合硫化亚铁的X射线衍射谱图, 在14°、58°处也有衍射峰, 说明样品中含二硫化钼成分。即可证明硫化亚铁与二硫化钼成功负载, 达到预期效果。

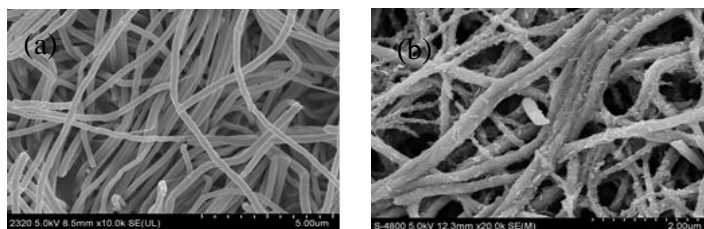


图2 硫化前后电纺纤维膜SEM图: (a) 硫化前纤维膜SEM图; (b) 硫化后纤维膜SEM图

如图2 (a)所示, 硫化前纳米纤维直径分布均匀, 表面较为光滑, 直径在500-600 nm之间。而图2 (b), 纤维膜在高温硫化后, 发生了一定程度的收缩, 纳米纤维直径分布在200-300 nm之间, 且纤维之间发生了一定程度的粘结, 纤维表面变得粗糙并且在表面形成了一些片状物质, 推测是硫化过程中的高温使得纤维发生了一定程度的熔化并造成纤维之间的黏粘, 同时硫蒸气与纤维中的氯化铁发生反应形成硫化铁, 而四硫代钼酸铵在高温条件下会热解成硫化钼, 二者共同形成了纤维表面的物质。

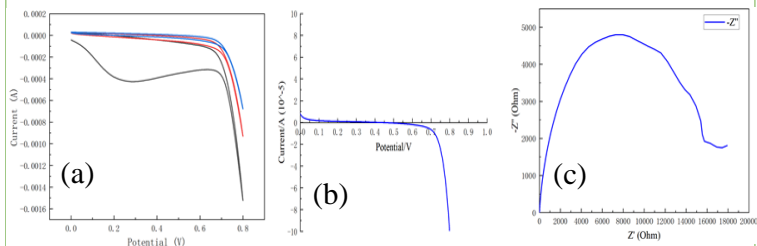


图3 硫化后Fe基电纺纤维电化学测试图: (a) CV测试, 扫描电压0~0.8V, 扫速0.05 mV/s; (b) LSV测试, 扫描电压0~0.8V, 扫速0.005mV/s; (c) EIS测试, 频率为0.1~10⁶ Hz, 初始电压0.68 V。

如图3所示, CV曲线有完整循环, 电纺粉末催化剂在0.3 V处显示出氧还原峰。从LSV中可以看出半波电势 ($E_{1/2}$) 达到0.7 V, 接近Pt/C ($E_{1/2}$ =0.83 V), 催化剂表现出良好的ORR催化性能。在EIS测试中, 催化剂的电子转移阻抗为15Ω, 较为良好, 推测得益于催化剂与电纺粉末的协同效应。

结论

1. 成功通过静电纺丝的方法制备铁基催化剂纳米纤维膜, 且物理结构良好。
2. 将Fe基催化剂与电纺纤维结合在一起制备出了一体化空气阴极, 表现出良好的催化性能, 表明此柔性自支撑型阴极可以改善界面性能。

致谢:

天山青年计划 (2020Q073)

参考文献:

1. Gates BD, Flexible electronics [J], Science, 2009, 323:1566-1567.

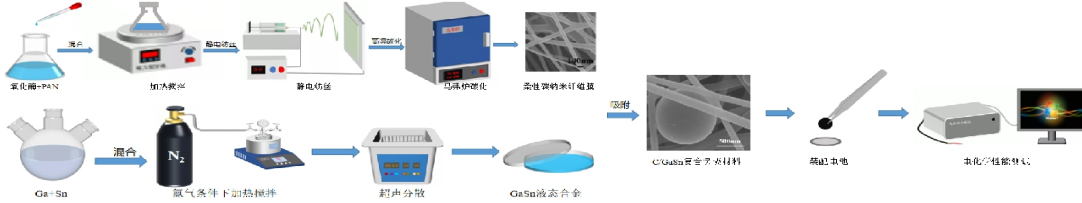
2. Xie Keyu, Wei Bingqing. Materials and structures for stretchable energy storage and conversion devices[J]. Advanced Materials, 2014, 26(22): 3592-3617.
3. Yue Guanghui, Liu Jiandi, Han Jiangtao, et al. Amorphous CoSnO₃@rGO nano-composite as an efficient cathode catalyst for long-life Li-O₂ batteries[J]. Chinese Journal of Catalysis. 2018,39(12):1951-1959.
4. Jing Fu, Zachary Paul Cano, Moon Gyu Park, et al. Electrically rechargeable zinc-air batteries: progress, challenges, and perspectives[J]. Advanced Materials, 2017, 29: 1604685.
5. Pei Pucheng, Wang Keliang, Ma Ze. Technologies for extending zinc-air battery's cycle life: A review[J]. Applied Energy. 2014, 128(C):315-324.



引言

室温下液态金属是一种具有特殊金属形式的低熔点材料, 具有液体的流动性和自愈合性, 以及金属良好的电导率和导热性, 其中毒性较小的镓和镓基合金因其低熔点、高电导率、高表面张力以及可调熔融温度等优点而备受关注。本文以静电纺丝、高温碳化的方法制备具有网络结构的柔性碳纳米纤维膜为基底, 吸附 GaSn 液态合金, 可以直接作为锂离子电池自支撑负极材料, 探究了 GaSn 液态合金在柔性多孔碳纳米纤维膜中的分布情况及其电化学性能。

实验过程



- 以氧化煤和聚丙烯腈(PAN)作为碳的前驱体采用静电纺丝、高温碳化的方法制备柔性碳纳米纤维膜。
- 取Ga和Sn单质金属放入三口烧瓶中, 在氮气条件下进行加热搅拌, 然后超声分散制备GaSn液态合金。
- 以柔性碳纳米纤维膜为基底, 吸附制备的GaSn液态合金纳米颗粒, 在超声条件下制备C/GaSn复合负极材料。
- 利用制备好的锂离子电池自支撑负极材料装配电池, 并进行电化学性能测试。

结果和讨论

1. C/GaSn 复合负极材料的形貌分析

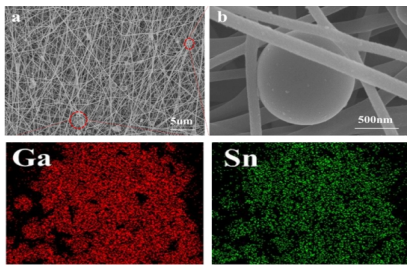


图1 C/GaSn 复合负极材料的 SEM 和元素分布图

从图1a中观察到纳米纤维表面分布着许多球状颗粒物质, 它们分布在纳米纤维膜表面, 或者分布在纳米纤维之间被纤维紧紧的缠结在一起。如图1b所示, 球状颗粒被相互交织的纤维紧密的缠绕在纤维层中, 形成稳定的结构。图1c、1d中, 对表面进行了 mapping 测试, 表面分布的有 Ga 和 Sn 元素, Ga 和 Sn 元素说明纳米纤维膜表面黏附的颗粒物质是 GaSn 液态合金。

3. 电化学性能分析

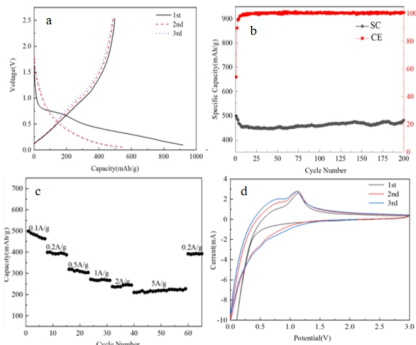


图4 GaSn /C 电池的电化学性能曲线

2. TG测试和XRD表征

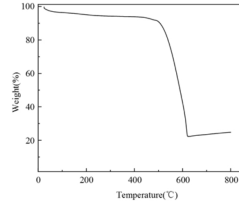


图2 C/GaSn 复合材料的TG图

从图2可以发现材料在 500 °C 以下有轻微的失重, 失重率在 10 % 左右; 在 500 °C 左右, 材料的质量急剧下降; 在温度大于600 °C 时, 物质的质量有所增加; 最后剩余 24.78 wt% 则是无机碳和 GaSn 液态合金及其高温下产生的氧化物。图3是C/GaSn 复合负极材料的XRD图, 图中分别在 2θ=26° 和 2θ=37° 左右有一个宽且短的衍射峰, 说明材料中的碳和金属基化合物的晶型结构相对无序, 强度较弱。其中在 2θ=26° 左右的衍射峰对应于柔性碳纳米纤维膜中的无定型结构的碳材料, 在 2θ=37° 左右的衍射峰对应于液态合金中 Ga 基氧化物。

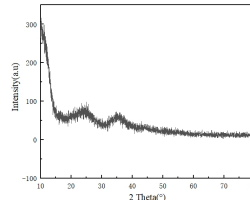


图3 XRD图

图4a是 C/GaSn 复合负极材料在电流密度为 50 mA/g 时的恒流充放电曲线, 该材料的首圈充电容量和放电容量分别为498.8 mAh/g 和 918.6 mAh/g。图4b是C/GaSn 复合负极材料在电流密度为50 mA/g 循环200圈循环性能曲线, 第 200 圈的充电容量和放电容量分别是484.4mAh/g 和 479.4 mAh/g, 循环 200 圈的容量保持率是 97.1 %。图4c是电流密度梯度分别为 0.1 A/g, 0.2 A/g, 0.5 A/g, 1.0 A/g, 2.0 A/g, 5.0 A/g 和 0.2 A/g 的倍率曲线, 可以发现在前 8 圈时, 即使电流密度很小, 但是容量衰减依然严重, 但电流密度在 0.2 A/g 时, 容量保持率较好, 经过高电流密度5 A/g 循环之后, 依然能够回到 0.2 A/g 的初始容量。图4d是复合负极材料的CV 曲线, 可以看出, 循环三圈的 CV 曲线均在 1.0 V 左右有明显的氧化峰, 进行锂离子的脱出, 而在 0.6 V 左右出现一个不明显的峰, 可能原因是 C/GaSn 复合材料表面元素更多的是 GaSn 液态合金, 另一方面是在测试过程中扫描速率过大导致还原峰不明显。

结论

我们采用制备的柔性多孔碳纳米纤维膜吸附 GaSn 液态合金纳米颗粒用作自支撑的锂离子电池负极材料, 组装成扣式电池, 并对其形貌以及电化学性能进行了表征和测试, 结果表明: (1) 制备的柔性碳纳米纤维膜具有丰富的网络结构, 较高的孔隙率, 可弯曲折叠性能较好, 并且具有一定的导电性, 可直接作为锂离子电池负极材料。(2) 以金属镓(Ga)为基底的液态合金与金属锡(Sn)制备的 GaSn 液态合金呈球状, 尺寸大小分布在 300-1200 nm。(3) 制备的 C/GaSn 复合负极材料的首圈效率与纯的柔性碳纳米纤维膜相比有所提高, 容量增大, 循环稳定性较好, 其中首圈的充放电容量分别是 498.8 mAh/g 和 918.6 mAh/g, 200 圈的容量保持率为 97.1 %

致谢

国家自然科学基金项目(51963020);
新疆自治区杰出青年项目 (2020q003)

参考文献

- [1] Thi T V, Rai A K, Gim J. Journal of Alloys and Compounds, 2014, 598: 16-22.
- [2] Bing Ding, Xiaoliang Wu. Journal of Alloys and Compounds, 2020, 842: 155838.
- [3] Boley J W, White E L, Kramer R K. Advanced materials, 2015, 27(14): 2355-2360.
- [4] Dickey M D. ACS Appl Mater Interfaces, 2014, 6(21): 18369-18379.
- [5] Yang Y, Sun N, Wen Z, et al. ACS Nano, 2018, 12(2): 2027-2034.
- [6] Xin G, Wang Y, Liu X, et al. Electrochimica Acta, 2015, 167: 254-261.
- [7] Yao H, Wang H J, Jiang Y B, et al. Materials Letters, 2020, 276: 128261.
- [8] Luo Z, Ji C, Yin L, et al. Materials Today Energy, 2020, 18: 100559.
- [9] Huang X, Cui S, Chang J. Angew Chem Int Ed Engl, 2015, 54(5): 1490-1493.22.
- [10] Sohn Y, Chu K. Materials Letters, 2020, 265: 127223.
- [11] Gancarz T, Berent K, Schell N, et al. Journal of Electronic Materials, 2019, 48(9): 5941-5947.
- [12] Chiechi R C, Weiss E A, Dickey M D. Angewandte Chemie, 2010, 120(1): 148-150.
- [13] Michael D. ACS Appl. Mater. Interfaces, 2014, 6: 18369-18379.

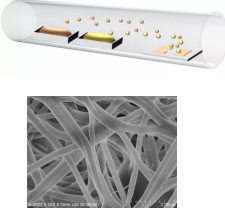
常压PECVD法制备多维SnSb/C/DLC 纳米纤维及性能研究

闫源¹, 马勇², 周慧敏³, 夏鑫*,
新疆大学, 纺织与服装学院, 新疆 乌鲁木齐 830046

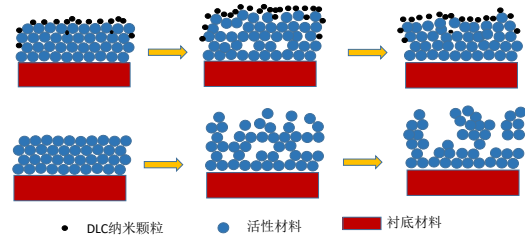
摘要: 为改善SnSb/C纳米纤维形态结构并获得优异的锂电性能, 借助于PECVD技术将硬度高、摩擦系数低、生物相容性好的DLC纳米颗粒碳材料分别引入两种不同前驱体的SnSb/C纳米纤维负极材料中, 以期解决SnSb/C纳米纤维做锂电池负极材料时, 多次循环后因锡铋合金膨胀、材料结构破坏导致的容量衰减的问题。结果表明: 改造的常压PECVD装置成功制备的结晶性能良好的DLC纳米颗粒, DLC纳米颗粒与纳米纤维形成的多维结构与特殊形貌可以有效抑制负极合金材料的大体积膨胀, 使得SnSb/C/DLC纳米纤维负极材料在经过100次充当循环后仍然能达到70.1%的容量保持率。

关键词: 等离子体化学气相沉积; 锡铋碳纳米纤维; 类金刚石碳纳米颗粒;

引言

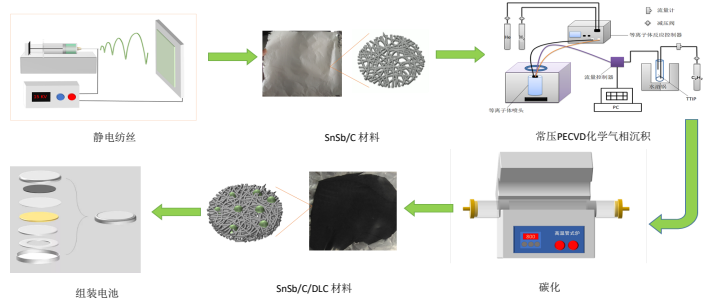


纳米纤维负极材料目前普遍存在体积膨胀严重的问题, 并可能造成活性材料的破裂、脱离, 导致电池循环性能持续下降。等离子体引发化学气相沉积(PECVD)技术, 因其结构构建功能优异, 制备纳米薄膜性能良好的优点在太阳能电池及抗菌材料等领域被广泛研究。而PECVD法高的沉积温度以及苛刻实验条件使其在锂电池负极材料领域应用较少。在前期工作中针对性的就改造相关的沉积实验条件进行研究, 并在本实验中通过构建多维结构的纳米纤维与DLC纳米颗粒复合合金材料, 以达到缓解电池负极材料因其体积膨胀, 结构破坏导致的容量衰减问题展开研究。



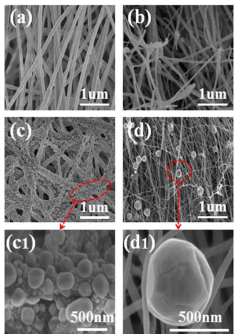
实验过程

1. 配置8wt%的PAN/DMF溶液, 锡铋前驱体与PAN的质量比1:2, 60°C下持续搅拌24进行静电纺丝, 得到SnSb/C前驱体纳米纤维。
静电纺丝参数: 电压18KV, 速率0.6mL/h, 滚筒收集装置转速 1500r/min, 收集距离20cm。
2. 利用自制常压等离子体化学沉积装置对静电纺丝膜进行沉积, 控制等离子体沉积头与基底材料距离为7mm, 利用氧气等离子体在100w的功率下对纳米纤维进行表面清洁10s。调整仪器功率110w, He速率为31L/min, H₂速率为0.35L/min, 乙炔速率为0.06L/min, 当反应腔温度升至180°C时, 打开气路开关沉积10min。
3. 将沉积后的纳米纤维膜进行碳化, 首先在空气中以2°C/min的升温速率升至280°C, 保温5h后再N₂氛围下以2°C/min升至800°C, 保温4h, 降温取出。
4. 将碳化的纳米纤维膜经研磨涂层后组装扣式电池并测试



结果和讨论

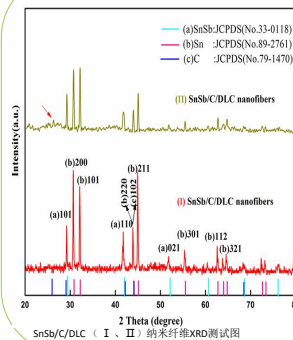
SEM形貌结构分析



SnSb/C和SnSb/C/DLC纳米纤维SEM测试图

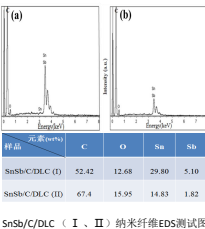
图a、b分别是采用SnCl₄·5H₂O/SbCl₃ (I)、Sn(CH₃COO)₂/Sb(CH₃COO)₃ (II)作为前驱体制备的SnSb/C电镜图, 可以看出a图的纤维一致性远远大于b图的纳米纤维。原因可能与电纺溶液本身的粘度及电导率有关。图c、d分别是a、b经沉积DLC纳米颗粒后的电镜图。图c1、d1分别是c、d的局部放大图。由图可知, c、d图中不同前驱体制备的DLC纳米颗粒沉积在相同的纳米纤维上时, 其形貌和结构不同。SnSb/C/DLC (I)纳米纤维通过沉积过程相互交联并形成网络。DLC沉积在纳米纤维上形成了不规则的立方纳米颗粒。这些纳米颗粒在沉积过程中被碳层覆盖或嵌入到复合材料中。不同于球形形状。此外, SnSb/C/DLC (II)纳米纤维上分散的纳米颗粒SnSb/C/DLC (I)纳米纤维上纳米颗粒的立方形状, SnSb/C/DLC (II)纳米纤维上纳米颗粒的数量较少, 如图d所示。对于PECVD沉积的纳米DLC纳米颗粒在不同纤维上表现的形貌不同, 其生长机理尚不完全清楚。其原因可能是因为(I)不同SnSb/C前驱体制备的纳米纤维表面可能决定了DLC纳米颗粒的形貌和结构。(II)对于纳米纤维沉积的DLC纳米颗粒, 当C₂H₂与不同的SnSb/C纳米纤维反应时, 由于两种纳米纤维表面的化学基团不同, 沉积的DLC纳米颗粒可能具有不同的结构形态。

晶形结构分析



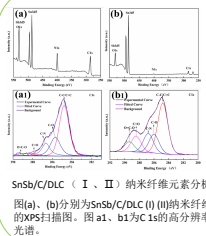
SnSb/C/DLC (I) (II)纳米纤维的主衍射峰尖锐而强烈, 表明其高结晶性。需要注意的是, SnSb/C/DLC (I)纳米纤维在2θ=43.9°处的峰值可归为金刚石(C(ICPDS No.00-79-1470)的(102)面。2θ=43.9°处的峰增加, 表明DLC纳米颗粒具有良好的结晶性能和良好的结构稳定性。沉积后的峰值没有变化, 表明没有晶格减少。此外, SnSb/C/DLC (I)纳米纤维中26.6°(图中红色箭头所示)的峰消失了, 该峰属于金刚石SnO₂(ICPDS No.00-041-1445)。SnSb/C/DLC (II)纳米纤维前驱体在碳化过程中, 碳可以还原二氧化锡形成锡, 反应可记为: SnO₂+C→Sn+CO₂。SnO₂峰的消失意味着沉积的DLC纳米颗粒增加了碳含量, 并完全还原了SnO₂。

表面元素含量分析



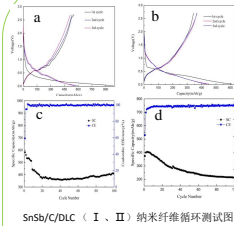
图a、b分别显示了SnSb/C/DLC (I)和SnSb/C/DLC (II)纳米纤维的C、O、Sn、Sb元素分布。可以看出, 不同SnSb/C/DLC纳米纤维上的元素含量有明显的差异。由表1可知, SnSb/C/DLC (I)和SnSb/C/DLC (II)纳米纤维的Sn、Sb含量分别为29.8wt%、5.10wt%和14.83wt%、1.82wt%。此外, 两种SnSb/C/DLC纳米纤维的碳元素含量均最高。

表面元素性质分析



图a、b中Sn3d₅信号的发生确认的Sn成纳米纤维。而通过xps中c峰的存在结合图(a1)(b1)可以看出, 其两个材料中284.8 eV和285.4 eV的能量峰分别对应着大量的sp³碳(C-C)和sp²碳(C=C)。284.5 eV表示C-C/C-C键。碳键(C-C)和不饱和碳键(C=C)分别由sp³杂化碳键和sp²杂化碳键衍生而来, 即成功将DLC纳米颗粒引入材料中。在碳1s高分辨谱中出现了不同含氧官能团可能是制备过程中的杂质引起的。

电池循环性能分析



SnSb/C/DLC (I、II) 纳米纤维循环测试图

图a、b显示SnSb/C/DLC (I) (II)纳米纤维的初始充放电容量分别为582 mAh/g和983 mAh/g、374 mAh/g和610 mAh/g, 对应的初始库伦效率分别为59.2%、%和61.3%。SnSb/C/DLC (II)纳米纤维的循环性能如图c、d所示, 循环100次后, SnSb/C/DLC (I)纳米纤维的容量保持率分别为70.1%和57.1%。从图c可以看出, SnSb/C/DLC (I)纳米纤维的网络结构和DLC均匀分布在SnSb/C/DLC (I)纳米纤维上, 使得SnSb/C/DLC (I)纳米纤维的容量衰减略有缓解。从图d可以看出, 循环100次后, SnSb/C/DLC (II)电极的放电容量为213.6 mAh/g, 容量保留率为57.1%。SnSb/C/DLC (II)的形成很可能是由于Li⁺萃取-插入过程中SnSb粒子体积发生了巨大的变化。由于没有有效的C抑制作用, SnSb粒子在循环过程中体积膨胀导致工作电极结构损伤, 电接触失效。第一次循环效率较低, 部分原因是由于复合材料的无序性和晶体尺寸较小。同时, SEI膜的形成也可能是非晶碳复合材料中普遍存在的不可逆容量衰减的原因之一。

结论

我们采用常压PECVD设备在纳米纤维合金负极材料上沉积DLC纳米颗粒后, 组装扣式电池, 研究其对材料电化学性能的影响, 其结论如下:

- (1) 自主改造的常压PECVD设备成功在纳米纤维表面引入了大量的DLC纳米颗粒, 并牢牢附着在SnSb/C纳米纤维表面, 并且该纳米颗粒具有良好的物理化学结构。
- (2) DLC纳米颗粒与纳米纤维形成的多维结构与特殊形貌可以有效抑制负极合金材料的大体积膨胀, 使得SnSb/C/DLC (I)纳米纤维负极材料在经过100次充当循环后仍然能达到70.1%的容量保持率。

致谢

国家自然科学基金项目 (51963020)
新疆自治区杰出青年项目 (2020q003)
新疆自治区研究生科研创新项目 (XJ2021G074)

参考文献

- [1] 刘忠志, 周仁, 李丹. 一种PECVD设备低温控制系统: 201510618286.4[P]. 20109-24.
- [2] 王小绘. 锂离子电池锡基合金负极材料的制备及改性研究[D]. 浙江工业大学, 2014.
- [3] Yuan Z, Dong L, Gao Q, et al. SnSb alloy nanoparticles embedded in N-doped porous carbon nanofibers as a high-capacity anode material for lithium-ion batteries[J]. Journal of Alloys and Compounds, 2018.
- [4] Sekhar C, Ray D, Mukherjee, Sweetie Sarma, et al. Functional diamond like carbon (DLC) coatings on polymer for improved gas barrier performance[J]. Diamond and Related Materials, 2017, 80:59-63.
- [5] Ladwig A M, Koch R D, Wenski E G, et al. Atmospheric plasma deposition of diamond-like carbon coatings[J]. Diamond and Related Materials, 2009, 18(9):1129-1133.
- [6] Jie Z, Rong Y, Lei X, et al. Cheminform Abstract: Plasma-Assisted Approaches in Inorganic Nanostructure Fabrication[J]. Cheminform, 2010, 41(22):1451.
- [7] Zhang S, Yao F, Yang L, et al. Sulfur-doped mesoporous carbon from surfactant-intercalated layered double hydroxide precursor as high-performance anode nanomaterials for both Li-ion and Na-ion batteries[J]. Carbon, 2015, 93:143-150.
- [8] Peled E, F Patolsky, Golodnitsky D, et al. Novel Silicon Nanowires-Based 3D Anodes for High-Capacity Lithium Ion Batteries[J]. Nano.let.2015, 15:6
- [9] Leigang, Xue, Xin, et al. A simple method to encapsulate SnSb nanoparticles into hollow carbon nanofibers with superior lithium-ion storage capability[J]. Journal of Materials Chemistry, A, 2013, 1:13807-13813.
- [10] Sekhar, C, Ray, et al. Functional diamond like carbon (DLC) coatings on polymer for improved gas barrier performance[J]. Diamond & Related Materials, 2017, 80:59-63

摘要: 通过前期的研究工作, 筛选出最优的硅/碳/石墨 (Si@C-G) 复合材料作为锂电池的负极材料。分析了在不同粘合剂作用下的Si@C-G复合材料, 其对材料电化学性能的影响和粘合剂对硅界面行为产生的变化。结果表明: 羧甲基纤维素钠&丁苯橡胶对复合材料的粘合效果最好, 其对应的循环性能最好; 羧甲基纤维素钠的长直链结构与丁苯橡胶的柔性结构形成的二维网络能够包覆活性材料, 使电极片的结构保持稳定, 提高了Si@C-G材料在充放电过程中的稳定性。

关键词: 粘合剂; 复合电极材料; 电化学性能

引言

目前, 锂离子电池被越来越多地用作便携式电子设备、电动汽车、等热门行业的电源。锂离子电池负极材料中, 硅是理想的选材之一, 但在充放电过程中其体积变化较大, 高效粘合剂是克服这一缺陷的有效方法。具有二维网络的粘合剂对活性物质有较高的粘附力, 这种粘合剂结构中含有羧基、羟基, 如羧甲基纤维素钠、聚酰亚胺等, 形成的共价键或氢键可以与硅产生较强的相互作用, 从而形成相对稳定的界面^[1]。我们通过粘合剂的特性, 筛选出了不同的粘合剂, 来配适之前优选出的Si@C-G负极材料^[2]。在此研究了Si@C-G负极材料在不同粘合剂作用下, 其界面行为的变化和材料电化学性能的改变。

实验过程

1. 实验方法与表征

1.1 不同粘合剂Si@C-G电极的制备

以前期优选出的Si@C-G (Si:G=1:3) 负极材料为活性材料, 采用羧甲基纤维素钠、聚酰亚胺、羧甲基纤维素钠&丁苯橡胶 (羧甲基纤维素钠:丁苯橡胶=1:3) 作为粘合剂分别组装标准的CR2032纽扣电池。

1.2 电化学性能测试

组装好的电池静置12h后在室温下用电池测试系统(LAND CT2001A)进行测试, 恒流密度为50 mA g⁻¹, 电压范围在0.02V到2V之间。循环伏安(CV)曲线 采用扫描速率为1mv s⁻¹的电化学工作站(CHI-660E)进行。

结果和讨论

2. 实验结果与分析

2.1 不同粘合剂对硅/碳/石墨负极形貌与结构的影响

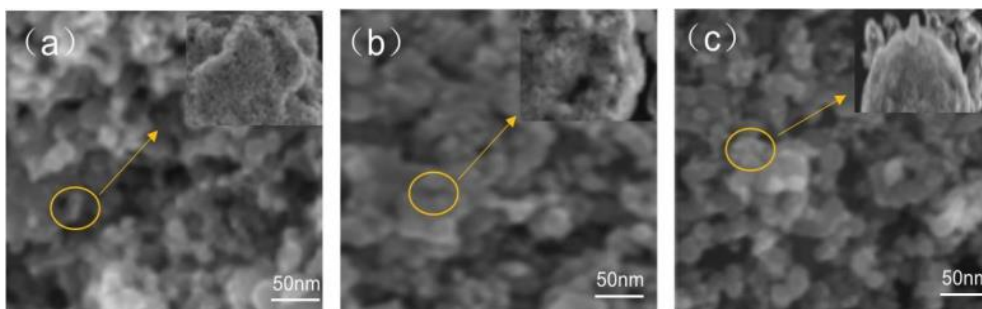


图1 不同粘合剂Si@C-G复合材料SEM图 (a: 聚酰亚胺, b: 羧甲基纤维素钠, c: 羧甲基纤维素钠&丁苯橡胶)

图1为不同粘合剂Si@C-G复合材料SEM图。从图中可以观察到硅的结构完整性保持较好。图a中硅颗粒的表面光滑没有异物; 图b中硅球的表面有少量附着物; 图c中相较前两张图可以观察到附着物明显增加。图中的附着物为添加的粘合剂, 随着不同粘合剂的加入, 硅颗粒和石墨表面的粘结剂逐渐增加。

由图2可知, 在 $2\theta=28.4^\circ$, 47.3° , 56° , 69° , 76.4° , 88.1° 处三种样品有明显的衍射峰, 分别对应于硅相 (标准卡: JCPDS No. 27-1402) 的 (111), (220), (311), (400), (331) 和 (422) 晶面。羧甲基纤维素钠&丁苯橡胶粘合剂相较于前两种粘合剂可以形成二维网络, 能够均匀的在硅碳表面覆盖并起到粘结作用, 其良好的覆盖作用, 硅的特征峰值呈现出较明显的降低。

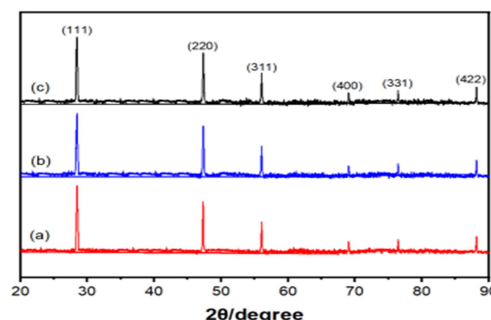


图2 不同粘合剂制备电极材料的XRD图 (a)聚酰亚胺 (b)羧甲基纤维素钠 (c)羧甲基纤维素钠&丁苯橡胶

2.2 不同粘合剂对Si@C-G负极材料电化学性能的影响

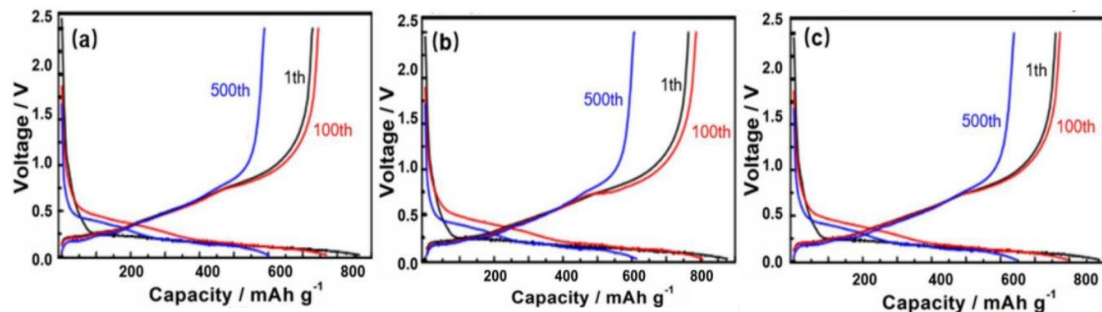


图3 不同粘合剂 (a)聚酰亚胺 (b)羧甲基纤维素钠 (c)羧甲基纤维素钠&丁苯橡胶制备电极的充放电曲线

图3是Si@C-G负极材料在不同粘合剂作用下的电压-容量的变化曲线。将聚酰亚胺粘合剂电极、羧甲基纤维素粘合剂电极、羧甲基纤维素-丁苯橡胶粘合剂电极在50 mA/g的电流密度下对其进行充放电，首次放电容量分别为865.1 mAh/g, 871.2 mAh/g, 881.4 mAh/g；首次库仑效率分别为86.6%，87.3%，87.5%。可以发现，从聚酰亚胺粘合剂到羧甲基纤维素钠&丁苯橡胶粘合剂，材料第一圈容量在逐渐增大，这得益于活性物质和粘合剂的接触点逐渐增多，增加了锂离子与电子反应位点的运输通道^[3]，从而提高了材料容量。

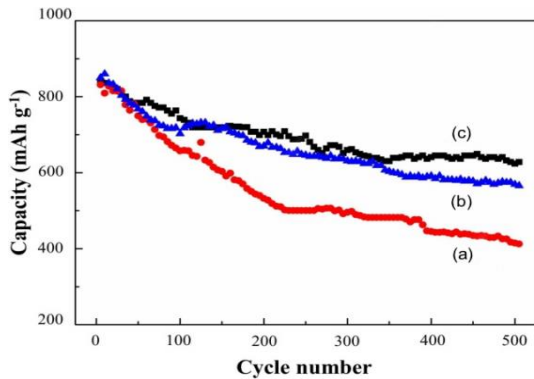


图4是复合材料在不同粘合剂作用下对应的的循环曲线。在经过500次循环后复合材料的容量保持率分别为55.8%、77.3%、80.3%。循环稳定性较差的是聚酰亚胺粘合剂对应的电极材料，羧甲基纤维素钠粘合剂对应电极材料的循环稳定性小于羧甲基纤维素&丁苯橡胶粘合剂电极材料。

图4 不同粘合剂Si@C-G复合材料的循环曲线图 (a)聚酰亚胺 (b)羧甲基纤维素钠 (c)羧甲基纤维素钠&丁苯橡胶

结论

研究了Si@C-G复合材料在不同粘合剂作用下，其对材料电化学性能的影响，其结论如下：

- (1) 聚酰亚胺、羧甲基纤维素钠和羧甲基纤维素钠&丁苯橡胶作为粘合剂对Si@C-G材料电化学性能稳定性的影响，其中，结合效果最好的是羧甲基纤维素钠&丁苯橡胶，其对应材料的循环稳定性也最好。
- (2) 羧甲基纤维素钠&丁苯橡胶粘合剂可以提高Si@C-G材料的电化学稳定性，这是由于在石墨和碳硅体系中羧甲基纤维素钠&丁苯橡胶的均匀分布，可以增加粘结位点，促进活性物质的粘结。羧甲基纤维素钠的长直链结构易与丁苯橡胶的柔性结构在循环过程中形成二维网络，从而包覆活性材料，使电极片的结构保持稳定，提高循环性能。

参考文献：

- [1] Lu J, Maggay I V, Liu W. CoV₂O₄ : A novel anode material for lithium-ion batteries with excellent electrochemical performance[J]. Chemical Communications, 2018, 54(25):3094.
- [2] 李天宇.结构型硅/碳/石墨负极材料构建及其作用机制[D].新疆大学,2020.
- [3] Le A, Wang M, Noelle D J, et al. Mitigating thermal runaway of lithium-ion battery by using thermally sensitive polymer blend as cathode binder[J]. Journal of Applied Polymer Science, 2017:45737.

基金项目：国家自然科学基金项目（51763022）；新疆研究生科研创新项目（XJ2019G073）。

致谢

非常感谢安徽工程大学提供此次宝贵的学习交流机会。本研究是在夏老师的悉心教导下才得以顺利完成，由衷的对夏老师的教导表示感谢！同时还特别感谢课题组的各位小伙伴在我实验和学习过程中提供的帮助。感谢成长过程中所有老师和同学的陪伴和帮助。最后，感谢国家自然科学基金项目（51763022）和新疆自治区研究生科研创新项目（XJ2019G073）对课题提供的支持。



聚吡咯基纳米纤维膜的制备及电化学性能研究

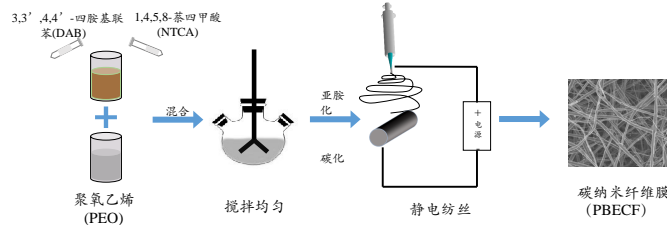
马鸣，陈品德，程璐，周惠敏，夏鑫*

新疆大学，乌鲁木齐，中国

引言

聚吡咯 (BBB) 分子主链拥有刚性多重稠环结构拥有优异的机械柔性、导电率，且含有一定的杂原子基团，满足锂电池电极材料的要求。纯BBB难以通过静电纺丝制备碳纳米纤维，因此采用两步法先制备BBB的前驱体并加入高分子量的聚氧乙烯进行纺丝再通过高温碳化得到碳纳米纤维膜。本文将改善BBB的可纺性和构建微纳米结构相结合，以获得优异的电化学性能。

实验过程



- DAB和NTCA等摩尔混合制备BBB的前驱体
- 制备7%PEO溶液作为助纺聚合物
- 加入一定比例的PEO溶液均匀搅拌制备纺丝液
- 调整适当参数进行静电纺丝
- 静电纺丝膜在经过亚胺化、碳化后得到碳纳米纤维膜 (PBCF)

结果和讨论

1. PBCF-85-15纤维形貌与柔性分析

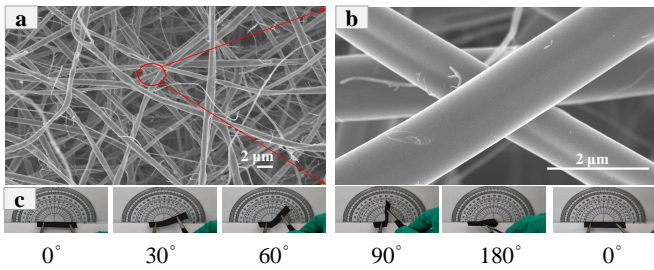


图1 PBCF-85-15纳米纤维膜的表面形貌、折叠0° - 180°的数码照片

图1a PBCF-85-15纤维表面附有许多细小纤维，细小短纤维穿插于纳米纤维膜中，因此BBB/PEO纳米纤维膜较紧密；短纤维的出现，可能由于纤维膜在高温碳化下，PEO作为牺牲材料从纤维表面中失重，而部分BBB材料在纤维从纤维表面脱落从而出现短纤维的现象；图1b为PBCF-85-15纤维膜的部分放大图，直径在760nm左右；图1c取PBCF-85-15宽为1cm，长5cm的纤维膜，将该膜重复从0°折叠至180°，纤维膜仍然保持良好的形貌，折叠处的纤维几乎没有出现断裂

2. PBCF红外光谱分析

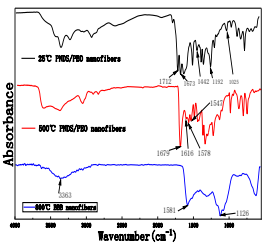


图2. 25°C、500°C、800°C PEO-BBB-85-15的红外光谱

图2为25°C、500°C、800°C PEO-BBB-85-15的红外光谱，在25°C时在1708cm⁻¹处出现了-C=O-(CONH)特征峰为BBB前驱体特征峰。随着温度的升高，PEO/BBB中在1708cm⁻¹处的特征峰消失，PEO在碳化过程中发生热分解，-CH₂-的弯曲振动的峰强降低，500°C时，BBB/PEO中在1697cm⁻¹处的-C=O(CON)的特征峰、1578cm⁻¹处的-C=N-特征峰、1437 cm⁻¹处C-N产生伸缩振动的吸收峰强度增加，由以上说明可知，在温度在500°C时，缩聚成咪唑结构形成BBB。在温度升高到800°C时，-CH₂-弯曲振动的特征峰消失，这是由于在800°C时PEO热分解完全；-C=N-的伸缩振动的峰变强C=O的特征峰消失，这可能是由于高温使C=O键发生了断裂。

3. PBCF拉曼、XRD分析

图3、4为PEO-BBB-85-15的拉曼谱图和XRD图，为了验证800°C纤维膜中碳的形态。图3中在1360cm⁻¹和1580cm⁻¹处存在两个宽的信号峰，分别为D带和G带，I_D/I_G值越大说明石墨化程度越低，无定形态越高。PEO-BBB-85-15的I_D/I_G值为1.024 (大于1)，说明此材料石墨化程度不高，具有较多的无定形态。图4中材料在24°及43°处均有峰出现，这两处是碳材料的典型出峰位置，分别对应石墨的(002)面和(110)面，利用布拉格公式计算样品在24°左右的衍射峰的晶面间距，可以得到PEBFS的d002值为0.363nm。石墨的晶面间距约在0.34nm，越接近0.34nm说明石墨程度越高，说明这种材料的结晶度比较低，无定形碳含量比较高。无定形碳的存在意味着材料存在缺陷，而缺陷的存在往往可以提供更多的嵌锂位点，从而提高材料的比容量。

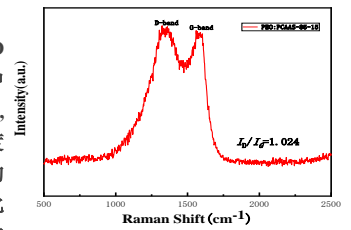


图3. PEO-BBB-85-15的拉曼谱图

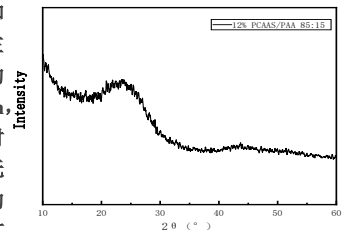


图4. PEO-BBB-85-15的XRD图

4. PBCF电化学性能分析

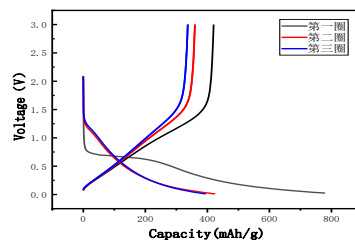


图5. PEO-BBB-85-15的充放电曲线

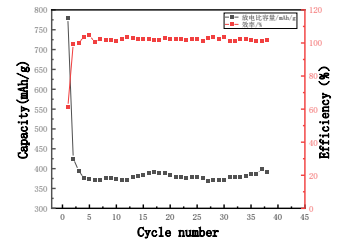


图6. PEO-BBB-85-15的循环性能效率图

图5为PEO-BBB-85-15前三圈的充放电曲线，首次放电过程在0.7V平台发生嵌锂过程，放电比容量为779.5 mAh/g，首次充放电的库伦效率为61.41%，图6为循环性能效率图，在循环38圈后，比容量为392.6 mAh/g、容量保持率为50.37%。

结论

为了改善聚吡咯 (BBB) 的纺丝性能，本文通过NTCA、DAB合成BBB前驱体加入牺牲材料PEO调节纺丝液粘度，经静电纺丝、高温处理得到PEO-BBB-85-15纳米纤维膜。结果表明：首圈的放电容量为779.4 mAh/g，38圈后，比容量为392.6 mAh/g、容量保持率为50.37%。与碳的比容量相比，本次研究采用静电纺丝制备PEO-BBB-85-15碳纳米纤维膜的方法，明显提升了碳基材料的比容量，更进一步发挥了碳基材料在负极材料的应用。

致谢

国家自然科学基金项目(51963020)；
新疆自治区杰出青年项目(2020q003)

[1] Y. Ding, et al. Polym. Sci, 2016, 61, 67—103
 [2] Zhou G, et al. Materials Letters, 2016, 165: 91-94
 [3] Lai C, et al. Journal of Power Sources, 2014, 247: 134-141.
 [4] Liu S, et al. RSC Adv, 2018, 8(45):25568-25574.
 [5] Zhu J, et al. Nanoscale, 2017:10.1039.C7NR07159K.
 [6] Abeykoon N C, et al. Rsc Advances, 2017, 7(34):20947-20959.
 [7] Zhu, J, et al. Journal of Materials Science, 2018, 53(12):9002-9012.
 [8] Peng S, Nano Energy, 2016, 22:361-395.
 [9] Jian, Zhu, Josef, et al. Acs Applied Materials & Interfaces, 2019.
 [10] B Y D A, et al. Progress in Polymer Science, 2016, 61:67-103.

Introduction

Unidirectional fiber-reinforced composites are affected by failure mechanisms such as fiber buckling instability in the direction of fiber axial compression, and their compression failure resistance is poor, which limits the further application of fiber composites. In this paper, the vine-like structure of carbon bundles was designed through polyester fibre wrapping for better mechanical properties. The effect of wrapped hybrid structure and diameters of polyester fibre on the mechanical properties of carbon-polyester fibre/epoxy unidirectional composites was investigated experimentally. Five kinds of specimens with different polyester filament diameters were produced. The impact, tensile and unidirectional compressive properties of WHC (Wrap Hybrid Composite) were measured.

Experimental process

The Wrapped carbon fibre bundles with mono-filament Hybrid Composite (WHC) were prepared using a custom winding machine and VARTM method. Firstly, the PET filament was wrapped on a spool rather than having a sleeve on the hollow shaft. With the carbon bundle throughout the centre of the shaft, the PET filament wrapped the carbon fibre upon spool rotation. Then, a unidirectional fabric was prepared by a rotary arrangement method. Four layers were paved for a composite laminate, and composed with the epoxy resin used the VARTM process.



Fig. 1. Vine-like structure

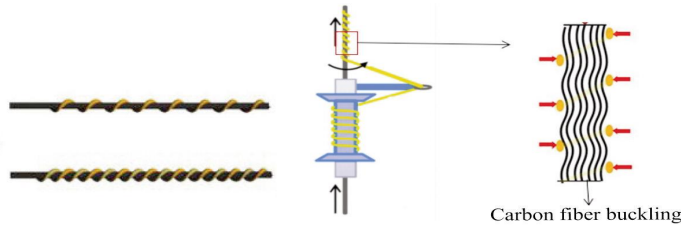


Fig. 2. Schematic diagram of carbon fibres buckling in the wrap process

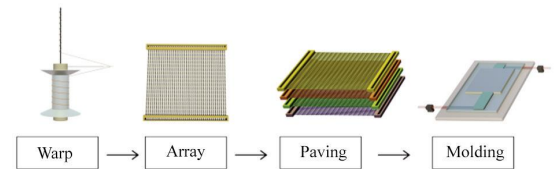


Fig. 3. Schematic of the preparation process for WHC

Results and discussion

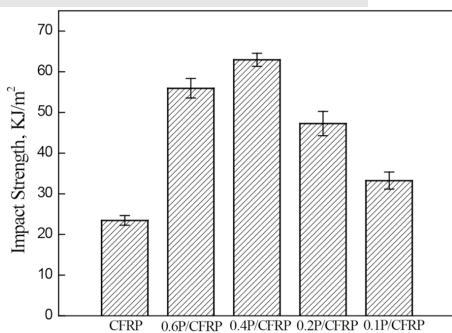


Fig. 4. Effect of diameter on the impact strength. Figure shows the effect of fibre diameter on the impact strength of the material. As can be seen from the figure, fibre wrapping improves the impact resistance of the composite material. Impact strength decreases as diameter increases and is highest for a diameter of 0.4 mm.

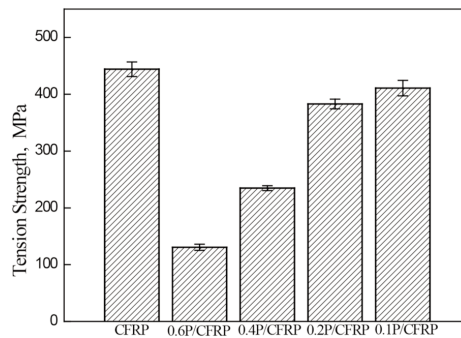


Fig. 5. Effect of diameter on the tensile strength. Figure shows the effects of fibre diameter on the tensile strength of the material. As can be seen from the figure, wrapping with polyester fibre contributes little to the tensile strength of the composites. Moreover, the performance of the composites decreases with increasing polyester fibre diameter.

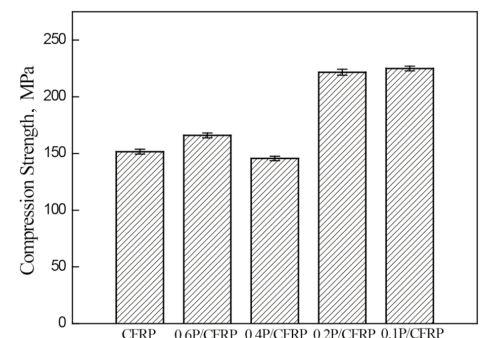


Fig. 6. Effect of diameter on the compressive strength. alters the compression failure mode of the composite material and improves its performance during compression. The use of finer PET fibers can more effectively enhance the compression properties of composite materials.

Conclusions

1. Polyester fibre wrapping improves the impact strength of the composites, which increases and then decreases as the diameter of the polyester fibre increases. The maximum impact strength of 62 KJ/m² was reached when the polyester fibre diameter was 0.4 mm, representing a 147% enhancement compared with the unwrapped material.
2. Wrapping with polyester harms the tensile properties of the composites because buckling of the carbon fibre can happen during wrapping, the degree of which has a great influence on the tensile strength of the composites. Moreover, the polyester fibre does not play a significant role in preventing tensile failure, and thus the tensile strength of the material drops.
3. Fibres with higher tensile strengths provide better impact resistance, while thinner wrapping fibres enhance the compression properties of the composite material more effectively.



Preparation and properties of multilayer sound absorbing materials based on waste PPS filter materials

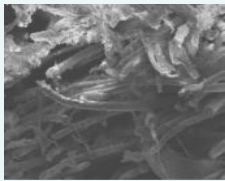
Zhang Shucheng, Xing Jian, Xu Zhenzhen*

Introduction

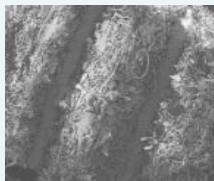
With the development of modern industry, tens of thousands of PPS filter materials are replaced every year. However, waste PPS filter materials are difficult to degrade in the natural environment. At present, the main treatment methods are stacking, landfill and incineration, resulting in serious environmental pollution; Noise pollution has a serious negative impact on people's hearing, nervous system and psychological state, so noise prevention and control has also become a key concern of the society. Therefore, it is proposed to use waste PPS filter material to prepare sound-absorbing and sound-insulating composite materials, which can not only solve the treatment problem of waste PPS filter material, but also reduce noise pollution.

Results and discussion:

1. Morphological analysis



Cross section shape of PPS filter bag

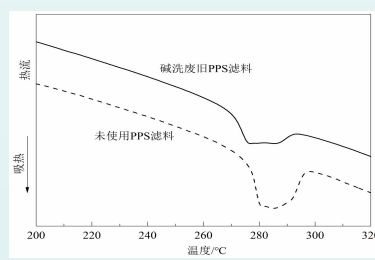
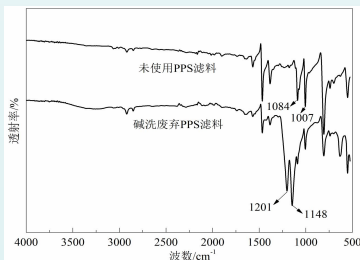


Composite section shape

The cross section of the composite becomes more regular, the interior of the material becomes more compact, the voids between fibers become smaller and more dense, the middle layer

obviously has the adhesive formed after the melting of PU film, the cross section becomes more flat, and the number of scattered fibers decreases.

2. Infrared and DSC test



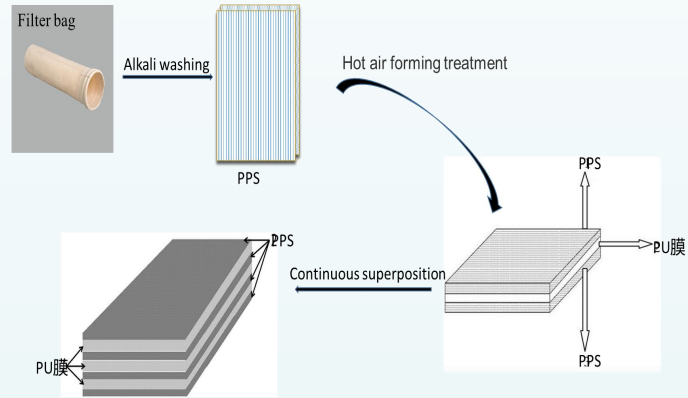
The absorption peak of C-S bond at 1084 cm⁻¹ weakened, indicating that the C-S bond of waste PPS filter material was destroyed during use, resulting in oxidative fracture and oxidative crosslinking, and PPS fiber was oxidized.

The melting peak of alkali washed waste PPS filter material moves to low temperature and widens. The melting peak temperature is 276.5 °C, the initial melting temperature is 270.0 °C, and the crystallinity is only 17.2%.

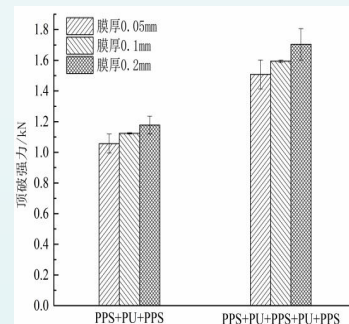
Conclusion

1. The crystallinity and thermal stability of alkali washed waste PPS filter material decreased because it was oxidized at high temperature during use, and the PPS macromolecular chain was oxidized, broken and crosslinked, resulting in the formation of some small molecular substances.
2. In the two structures, the bursting strength is positively correlated with the thickness of PU film.
3. PPS + PU + PPS + PU + PPS structure can reach 41db at high frequency, with good sound insulation performance.

Material preparation drawing

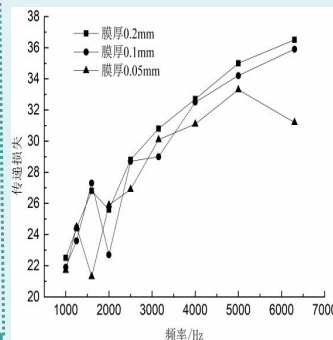


3. Bursting strength analysis

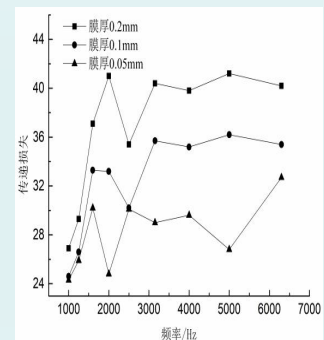


In PPS + PU + PPS structure, when the film thickness increases from 0.05mm to 0.2mm, the bursting strength increases by 6.3% and 11.4% respectively. In PPS + PU + PPS + PU + PPS structure, when the film thickness increases from 0.05mm to 0.2mm, the bursting strength increases by 5.7% and 13.0% respectively. It can be seen that the bursting strength decreases with the increase of composite thickness.

4. Sound insulation performance analysis



PPS+PU+PPS



PPS+PU+PPS+PU+PPS

Comparing the sound insulation performance of the two structures, it is found that the growth mode of transmission loss is obviously different in the high frequency stage. In PPS + PU + PPS structure, the transmission loss increases with the increase of frequency, up to 37dB; In the PPS + PU + PPS + PU + PPS structure, although the frequency continues to increase, the transmission loss remains flat and can reach up to 41dB.

Design of reinforced structure on 3D tubula composites

Min Erjun, Song Luping, Wang Hong, Wang Xu*

Anhui Polytechnic University, Wuhu, China.

Introduction

3d tubular composite is a 3d tubular woven composite reinforced by resin matrix. It has the advantages of light weight, high specific stiffness and strength, excellent fatigue resistance, high temperature and corrosion resistance, etc., and is widely used in satellite, missile, construction, pipeline repair, ship, aerospace and other important fields^[1].

Tubular tissue and three dimensional woven fabric are common, but the combination of the through-orthogonal tissue or angular interlocking tissue as the wall tissue and tubular tissue is rarely described in detail. In this paper, the combination of the two kinds of wall tissue and tubular tissue is proposed for reference.

Experimental process

The experimental materials

3d tubular fabric can be woven. The warp and weft yarn can be sample woven with PET or PP non-twisted chemical fiber filament. In this experiment, PET polyester (polyester filament) was used for both warp and weft yarns. The polyester filament used in this experiment is produced by Yizheng Company, Sinopec. The specification is 1111DTEX /192F, that is, the linear density is 1111 minutes. It is composed of 192 polyester monofilaments.

Experimental design Steps

The structure design of tubular three-dimensional woven fabric is divided into three steps:

- (1) Select the surface structure of tubular three-dimensional woven fabric;
 - (2) Table tissue according to the "negative turnover" method to get the inside tissue;
 - (3) According to the arrangement ratio of the warp and weft inside the surface and the method of layered weaving, the structure diagram of the three-dimensional tubular woven fabric is determined.
- The basic structure of three-dimensional tubular woven fabric can be selected through orthogonal, angular interlocking or multilayer.

Results and discussion

According to the design steps, the design process of the tissue chart is discussed by selecting the orthogonal through tissue and the through Angle interlock respectively.

1 through orthogonal tubular 3d tissue design

FIG. 1-1 shows a schematic diagram of three-dimensional tubular woven fabric based on three layers of orthogonal weft-through-type structure. Blue is the warp yarn, yellow is the ground weft, and green is the through-weft.

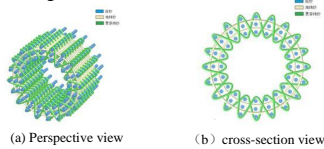


Figure 1-1 schematic diagram of three-dimensional tubular woven fabric based on three layers of orthogonal structure

The tubular three-dimensional woven fabric shown in Figure 1-1 is composed of warp, ground and through-weft. The warp is divided into outer, middle and inner layers, and the adjacent warp layers are supported by a layer of ground weft, which is then fixed by the through-weft to form a whole structure.

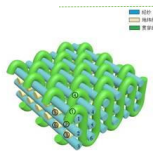


FIG. 1-2 Three-layer orthogonal structure of weft penetration



Figure 1-3 three-layer organization diagram through the orthogonal tissue

The surface microstructure and inner microstructure of tubular 3d woven fabric satisfy the relationship of "film reversal". FIG. 1-4-(b) is the inner microstructure chart obtained by "negative turnover" method with FIG. 1-4-(a) as the tabular microstructure, in which the warp is represented by number 1~VI and the weft is represented by number (I)~(VI).

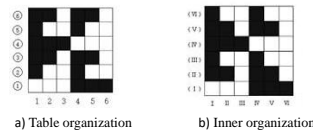


Figure 1-4. Table and inner tissue diagrams of the three layers of tubular three-dimensional tissue running through the orthojunction

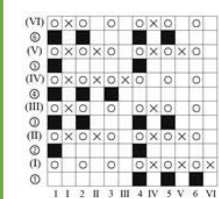


Figure 1-5 Structure diagram of three-dimensional tubular woven fabric through orthojunction

The simple and convenient threading method was used to draw the machine diagram of the four-layer angular interlocking tubular tissue, as shown in Figure 1-6 on the right.

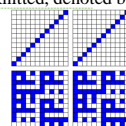


Figure 1-6 Computer diagram of three layers of tubular three-dimensional tissue running through the orthojunction

2 through Angle interlocking tubular three-dimensional structure design



Figure 2-1 Schematic diagram of four-layer angular interlocking structure

The three-dimensional angular interlocking tubular tissue can be obtained by using the angular interlocking tissue as the tube wall tissue combined with tubular tissue. The angular interlocking tissue was selected as the table tissue, and then the inner tissue was obtained by filling in the tissue points according to the negative turnover method. The inner and outer tissues of the four-layer angular interlocking tubular three-dimensional fabric are shown in Figure 2-2-(a)-(b) on the right.

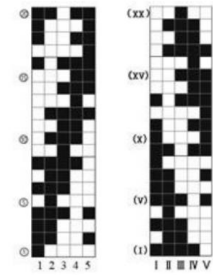


Figure 2-2 Three-layer angular interlocking tubular tissue table tissue and inner tissue

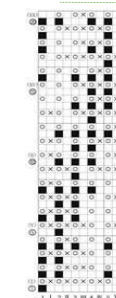


Figure 2-3 structure diagram of Angle interlocking tubular 3-D woven fabric

When the double layer structure is woven, the yarn is divided into two layers to be woven respectively. When the upper layer is woven, the upper layer is divided into two layers to interweave with the surface weft, and the inner layer is all lowered to the bottom. When the lower layer is woven, the surface warp is lifted in all layers, and the inner warp is divided into two layers and the inner weft are interwoven, while the inner weft and the surface warp are not interwoven. The tabular and inner arrangement ratio of tubular tissues was 1:1, and the tabular and inner tissues were embedded one to one. When the head is passed through, the table warp is successively passed through the odd heald frame, and the inner warp is successively passed through the even heald frame. It is similar to the method of weaving the tubular three-dimensional structure through the orthojunction. Figure 2-3 on the left shows the three-dimensional structure diagram of the angular interlocking tubular woven fabric. Figure 1-4 shows the meaning of each mark in the figure.

The simple and convenient threading method was also used to draw the machine diagram of the four-layer angular interlocking tubular tissue, as shown in Figure 2-4 on the right.



Figure 2-4 Computer diagram of the four-layer angular interlocking tubular structure

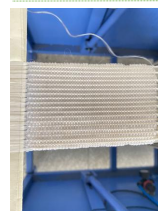


Figure 2-5. Four layers of angular interlocking tubular 3d fabric preform

Finally, the flat loom is started according to the drawing of the machine, and the small sample is obtained, as shown in figure 2-5 on the left.

Conclusions

Combined with the characteristics of the tubular fabric and the plane three-dimensional structure, the through-orthogonal structure and the Angle interlocking structure were used as the tabular structure respectively, and the inner structure was obtained by using the negative turning method, and then the structure chart of the tubular three-dimensional woven fabric was designed by the method of layered weaving according to the ratio of the outward-inside warp and the outward-inside weft 1:1. The experimental results show that the proposed design method is feasible and effective, which provides a valuable reference for further development of tubular three-dimensional composite reinforced structures.

引言

Polyester/cotton fabric has the advantages of good dimensional stability, small shrinkage rate, not easy to crease, easy to wash and quick to dry, etc., which is widely used in the fields of clothing, family curtains, bedding and industrial textile fabrics. However, polyester/cotton fabric is a flammable material, and its limit oxygen index value is only about 18%, and due to its special "wick effect", it is more difficult to flame retardant, research on improving the flame retardant properties of polyester/cotton fabric is particularly important.

At present, the flame retardants commonly used in polyester/cotton fabrics are mainly halogen and phosphorus. As is known to all, although halogen flame retardants have good flame-retardant effect, they will produce toxic gases such as dioxins in the process of combustion, which seriously harms personal safety and the environment. Their use has been limited. Environmental protection without halogen is a hot research topic of flame retardants nowadays. In recent decades, phosphorous, nitrogen, boron, silicon and other halogen-free flame retardants have attracted more and more attention. Among these flame retardants, phosphorous flame retardants have been paid great attention by researchers because of their low toxicity, low flue gas release and halogen-free characteristics. As a green and renewable organophosphorus system, biophytic acid (PA) has a high phosphorus content of up to 28%, which has great potential as a flame retardant.

In recent years, the research on the flame retardancy of phytic acid bio-based materials has been deepened. Liu huiliang et al. used phytic acid, glycerin and urea to form a new type of expandable flame retardant for flame retardant finishing of cotton fabric. After finishing, the LOI of the fabric is obviously increased, the heat release rate is decreased, but the durability is poor. Chen Wei et al. applied LBL method to finish chitosan and sodium phytate on polyester/cotton fabric modified by dopamine. After finishing, the LOI of polyester/cotton was significantly increased, but after 10 times of washing, the LOI decreased to 22.1%.

实验过程

1. Preparation of PEI and PA solution

3.0g PEI was weighed and placed in a certain amount of deionized water to prepare a 3% PEI solution. In addition, a certain amount of PA (mass fraction of 50%) was put into a 500 mL beaker, and an appropriate amount of deionized water was added to prepare the solution with mass fraction of 1.5%, 2% and 3% PA for use.

2. Preparation of flame retardant polyester/cotton fabric

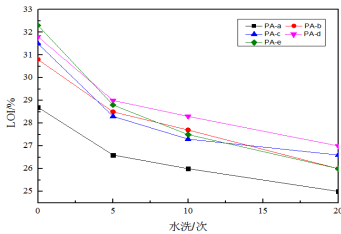
The polyester/cotton fabric was immersed in 3% PEI solution for 15 min, and then dried at 80 °C. The samples were then immersed in the solution with different mass fractions of PA for 15 min, and then removed and dried at 80 °C. To complete a layer of PEI/PA assembly, the above assembly process was repeated. After four times of assembly, all samples were washed with deionized water for 2 min, and then dried at 80 °C.

结果和讨论

Table 2 Flame-retardant properties of polyester/cotton fabrics before and after flame-retardant finishing

样品	增重率/%	LOI/%	垂直燃烧测试		
			损毁长度/mm	炭层厚度/mm	滴落时间/s
未处理	-	17.7	300	14.1	0
PA-a	45.40	28.7	105.5	0	0
PA-b	55.79	30.8	101.5	0	0
PA-c	50	31.5	100.0	0	0
PA-d	65.15	31.8	98.5	0	0
PA-e	67.56	32.3	98.0	0	0

The LOI value of the finished fabric was also proportional to the weight gain rate. And all the samples after finishing the combustion time and smoldering time are 0 s



After 20 washes, the LOI value of the finished polyester/cotton fabric is generally 26%, indicating that it still has flame retardant property.

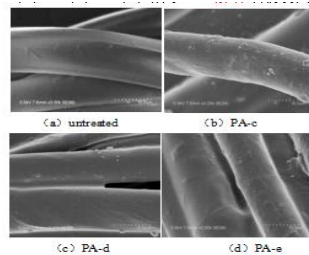
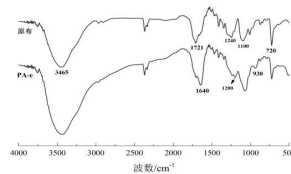
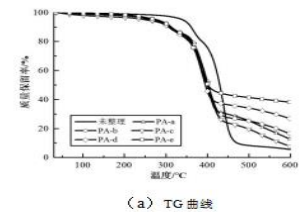


Fig 2 SEM photos of polyester/cotton fabric before and after flame retardant finishing ($\times 3000$)

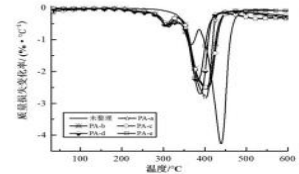
The surface of unfinished polyester/cotton fabric is smooth and clean, but the surface of polyester/cotton fabric becomes rough after finishing with PEI/PA flame retardant.



After finishing, 1640 cm^{-1} absorption peak appeared in FTIR curve, which belonged to -N-H-stretching vibration peak in PEI structure, and 1200 cm^{-1} and 930 cm^{-1} absorption peak appeared, which belonged to P=O and P-O stretching vibration peak in PA structure.



(a) TG 曲线



(b) DTG 曲线

Fig 5 TG and DTG curves of polyester/cotton under nitrogen atmosphere

After finishing, the polyester/cotton fabric has two weight loss stages, corresponding to the thermal decomposition of polyester and cotton components respectively, and the thermal decomposition temperature decreases significantly.

At 600 °C, the carbon residue of unfinished polyester/cotton fabric was 5.4% and PA-E was 38.2%. The carbon residue of finished polyester/cotton fabric was much higher than that of unfinished fabric.

结论

1) PEI/PA flame retardant coating was constructed on the surface of polyester/cotton fabric by layer self-assembly method. Compared with unfinished polyester/cotton fabric, the surface of PEI/PA finished polyester/cotton fabric becomes rough, and the characteristic absorption peaks such as P=O, P-O and -N-H- appear in the infrared spectrum, indicating that PEI/PA flame retardant coating has been successfully constructed on the surface of polyester/cotton fabric.

2) PEI/PA flame retardant coating can obviously improve the flame retardant property of polyester/cotton fabric. After finishing, the LOI of polyester/cotton fabric can be increased to 32.3%, the damaged length can be reduced to 98 mm, and the finished fabric has excellent drop-resistance.

3) The LOI value of PEI/PA flame retardant polyester/cotton fabric can be retained at 26% after 20 times of washing, indicating that PEI/PA flame retardant polyester/cotton fabric has good flame retardant durability.

4) The results of thermogravimetry showed that the initial decomposition temperature of polyester/cotton fabrics could be decreased after PEI/PA flame retardant finishing, and PEI/PA could promote the formation of stable carbon in polyester/cotton fabrics.

再生 PET 表面微孔改性及亲水性研究

胡超凡, 李继丰, 闫文静, 顾殿宽, 杜兆芳*
安徽农业大学, 合肥, 中国

引言

随着经济和社会的快速发展, 聚酯类纤维、塑料等制品消耗量剧增, 导致了大量的废旧聚酯污染。废旧聚酯再利用不仅可以解决聚酯填埋、燃烧带来的环境污染问题, 而且能够改善我国纺织原材料产量、生产规模严重不足的现状。聚对苯二甲酸乙二醇酯 (PET) 是一种力学和热力学性能优异, 弹性、耐磨性以及酸碱稳定性均较好的聚合物。但无论是原生或再生 PET 由于它的紧密分子链排列, 高结晶度, 以及较少的极性基团, 造成聚合物亲水和吸湿性差。研究发现, 轻质碳酸钙是一种流动性好、易分散、易混炼、表面润滑的无机颗粒, 利用碳酸钙掺杂聚合物能够显著提升聚合物的力学和热稳定性能。本课题以二次回收的再生 PET 切片为原料, 通过双螺杆挤出工艺将再生聚酯与碳酸钙微粒共混制备再生 PET 造孔母粒, 再通过酸处理工艺使再生 PET 表面产生微孔结构, 实现对 PET 的亲水改性。

实验过程

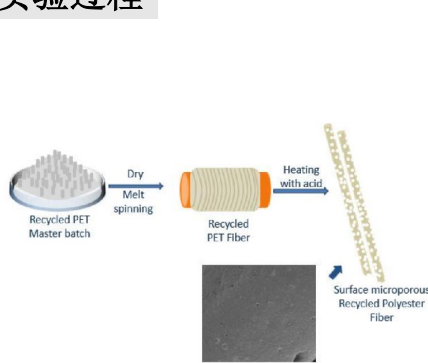


图1. 表面微孔的再生聚酯纤维制备流程图

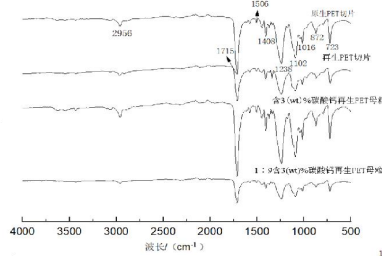


图2. 再生PET造孔母粒红外光谱图

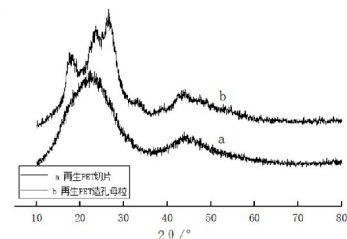


图3. 再生PET造孔母粒的XRD图

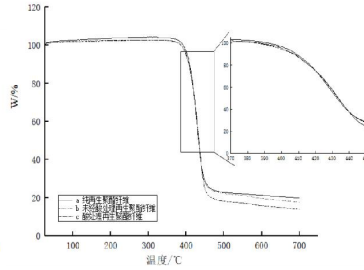


图4. 再生聚酯纤维热力学性能变化

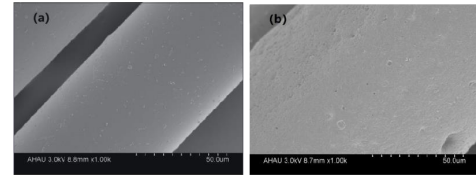


图5. 再生聚酯纤维与乙酸共热后表面微观形貌: (a) 不添加碳酸钙聚酯纤维; (b) 含碳酸钙粉末聚酯纤维

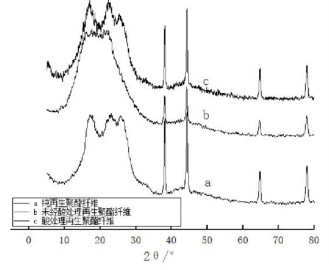


图6. 再生聚酯纤维结晶度变化

结果和讨论

图1为再生PET造孔母粒以及表面微孔再生聚酯纤维制备的流程图, 图2为再生PET造孔母粒红外光谱图, 可以看出在红外光谱图中碳酸钙的特征吸收峰并没有表现出来, 这是因为碳酸钙的特征吸收峰分别为: 1417.43 cm^{-1} 为 CO_3^{2-} 的反对称伸缩振动峰, 874.58 cm^{-1} 为 CO_3^{2-} 的对称伸缩振动峰, 1085 cm^{-1} 为 CO_3^{2-} 的面外弯曲振动峰, 724.6 cm^{-1} 为 CO_3^{2-} 的面内弯曲振动峰, 而这些特征峰与聚酯的振动吸收峰相重合。因此红外光谱分析表明碳酸钙被顺利地引入到再生PET聚合物体系中, 在熔融共混过程中碳酸钙微粒与再生PET发生了物理共混, 未改变PET的特征基团, 两者相容性良好。图3和图4说明含碳酸钙的再生聚酯纤维酸处理前的起始热降解温度为 $354\text{ }^\circ\text{C}$ 左右, 高于纯再生聚酯纤维的起始热降解温度, 这是因为再生聚酯纤维中碳酸钙粉末的耐热性导致其起始热降解温度升高。而含碳酸钙的再生聚酯纤维酸处理后的起始热降解温度是 $334\text{ }^\circ\text{C}$, 热降解率约为 86.42% , 热稳定性小于其他两者, 这是因为酸对纤维表面产生了一定“刻蚀”, 破坏了纤维的结构, 图5示, 同时经过酸处理后再生聚酯纤维表面的碳酸钙减少, 碳酸钙对其热稳定性的增强效果减弱, 导致其热稳定性下降。为进一步探究无机造孔颗粒碳酸钙对聚酯纤维的结晶度和结晶类型的影响, 如图6所示, 谱线b中特征峰消失, 谱线c中上述角度PET的特征峰又重新出现, 这说明由于碳酸钙在与PET熔融共混中起到了成核剂的作用, 使得PET的结构更规整, 特征吸收峰更明显。无机碳酸钙颗粒加入能够提高聚酯纤维的结晶度, 经酸处理后再生聚酯纤维的结晶度比未经酸处理的再生聚酯纤维有所降低, 这可能是因为PET经过酸处理后部分大分子链发生部分水解, 分子链断裂导致纤维的结晶区受到破坏, 结晶度下降。

结论

(1) 制备出的再生PET造孔母粒红外光谱分析表明碳酸钙被顺利地引入到再生PET聚合物体系中, 在熔融共混过程中碳酸钙微粒与再生PET发生了物理共混, 未改变PET的特征基团, 两者相容性良好。TG测试发现, 造孔剂碳酸钙加入后, 再生PET造孔母粒的起始热降解温度升高, 热失重率降低, 热稳定性增加。X射线衍射测试后表明, 碳酸钙的加入起到了成核剂的作用, 使得再生PET造孔母粒的结晶度增加。

(2) 实验利用乙酸与碳酸钙反应, 赋予再生聚酯纤维表面微孔结构, 再生聚酯纤维的回潮率可达 1.36% , 是聚酯纤维的公定回潮率 (0.4%) 的 3.4 倍左右, 纤维表面粗糙, 孔洞分布明显, 亲水性提高。此时, 表面微孔再生聚酯纤维的热稳定性和结晶度均有所下降。

纳米碳酸钙复合再生PET纤维的制备及性能研究

闫文静, 王娜丽, 杜兆芳*
安徽农业大学, 合肥, 中国
dzf@ahau.edu.cn

引言

实现废旧聚酯瓶片的回收再利用, 不仅可以解决环境污染问题, 而且可以改善目前我国产业用纺织品产量、规模等严重不足的现状。PET大分子中活性基团少, 导致其染色困难且吸湿性差, 亲水改性是国内外专家关注的焦点。电子束辐射接枝亲水基团、碱减量“剥皮”处理、亲水整理剂整理等方法虽然可提高纤维的润湿性能, 但是耐水洗性不高, 且会影响纤维的力学性能、产生大量废水。因此, 需探究出一种长效稳定、温和并可广泛应用的再生聚酯的亲水改性方法。

实验过程

实验原料: 废旧聚酯; 纺丝级半消光原生PET切片; CaCO_3 .



图1 制备微穴中空聚酯纤维制备流程

结果和讨论

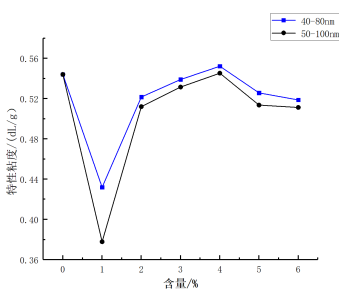


图2 纳米碳酸钙含量对再生聚酯母粒特性黏度的影响

探究纳米碳酸钙含量对再生聚酯母粒特性黏度的影响, 随着纳米碳酸钙增加, PET母粒粘度发生较大变化。

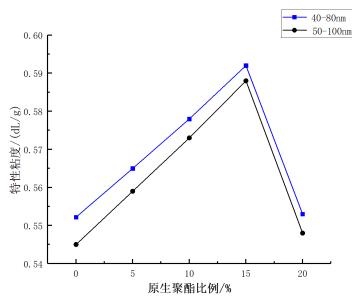


图3 原生聚酯比例对再生聚酯母粒特性黏度的影响

探究不同的原生聚酯与再生聚酯共混质量比对再生聚酯母粒特性黏度的影响。提高原生PET, 再生聚酯母粒的特性粘度可提升。

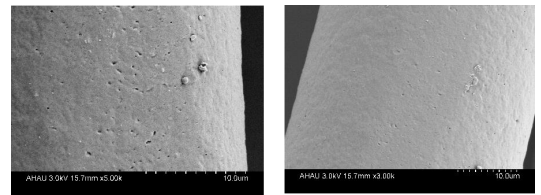


图4 纳米碳酸钙/再生聚酯复合纤维经乙酸处理形貌图

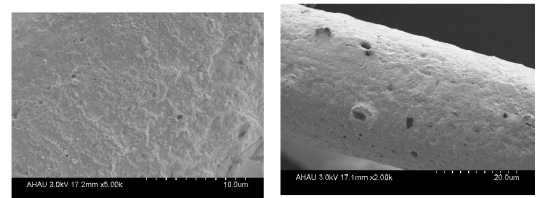


图5 纳米碳酸钙/再生聚酯复合纤维经盐酸处理形貌图

结论

当碳酸钙的含量为4%、粒径为40-80nm、原生PET瓶片含量为15%时, 再生PET母粒特性粘度为0.614dL/g, 此时可纺性能最佳, 且制得的纤维热稳定性和伸长率提高。所制得的再生PET纤维回潮率达到2.5%。

羊毛角蛋白在聚丙烯腈材料中的吸湿发热效应研究

顾殿宽, 何娅, 史浙安, 杜兆芳*

安徽农业大学, 合肥, 中国

dzf@ahau.edu.cn

引言

随着“轻、薄、暖”服用新理念的日渐流行, 开发自主产热式的保暖纤维和面料对于纺织服装行业来说意义非凡。角蛋白是一种天然蛋白质, 富含氨基、羟基等亲水基团, 具有良好的吸湿性、生物亲和性以及亲肤特性。本文首先从羊毛废脚料中提取角蛋白, 利用静电纺丝技术, 将角蛋白与PAN原位混合纺丝, 通过调节角蛋白与PAN的配比、纺丝液的浓度来制备在微环境中能自发进行吸湿发热的PAN/角蛋白复合纤维膜材料。

实验过程

实验药品		
药品名称	纯度规格	生产厂家
羊毛废脚料	-	安徽天威羊绒制品有限公司
聚丙烯腈	分析纯	国药集团化学试剂有限公司
N,N-二甲基甲酰胺	分析纯	国药集团化学试剂有限公司
十二烷基硫酸钠	分析纯	国药集团化学试剂有限公司
羧酸钠	分析纯	国药集团化学试剂有限公司
尿素	分析纯	国药集团化学试剂有限公司
氯化钠	分析纯	国药集团化学试剂有限公司
羊绒织物	-	安徽天威羊绒制品有限公司
甲基丙烯酸甲酯	分析纯	国药集团化学试剂有限公司



Fig 1.1 Wood keratin

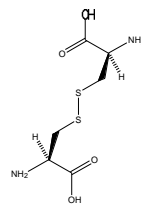


Fig 1.2 Structure of keratin cysteine

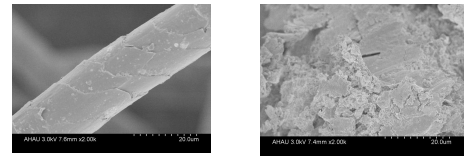


Fig 1.3 Comparison of morphology of wool before and after dissolving in buffer (a. before dissolving b. after dissolving)

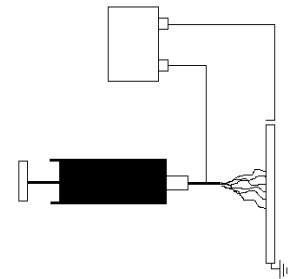


Fig 1.4 Schematic diagram of high voltage electrospinning of wool keratin and PAN

结果和讨论

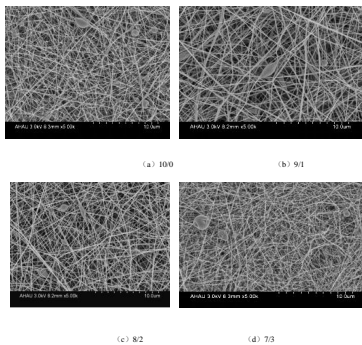


Fig 2 Micro morphology of fibers with different PAN/keratin ratios at 6% spinning solution concentration. (a) 100 b) 9:1 c) 8:2 d) 7:3

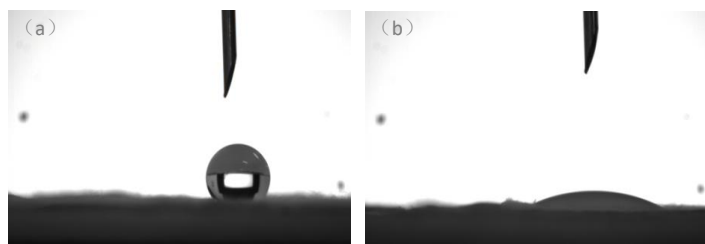


图2 (a) 纯PAN纤维膜接触角图 (b) 10%纺丝液浓度下PAN:角蛋白为7:3时纤维膜接触角图

图2 (a)、(b) 可以看出, 由于角蛋白中氨基、羟基等亲水性基团影响, PAN/角蛋白纤维膜的老水性、润湿性明显提高。

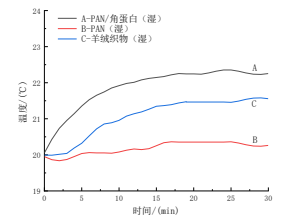


图3 试样温度变化曲线图

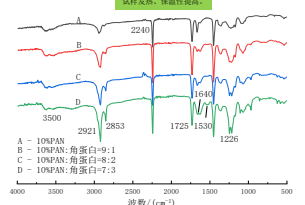


图4 10%纺丝液浓度下PAN:角蛋白为7:3时纤维膜红外光谱图

结论

(1) 当纺丝液浓度为10%, PAN与角蛋白配比为7:3时, 角蛋白与PAN之间界面相容性良好, 纤维表面光滑。随着角蛋白含量的增加, 复合纤维膜热稳定性提高, 但高角蛋白含量会导致其力学性能降低; 红外光谱与XRD谱图显示, 羊毛角蛋白在聚丙烯腈纤维膜中引入了氨基、羟基等亲水极性基团, 纤维膜吸湿性得到改善。

(2) 吸湿发热实验表明, 在 $90 \pm 3\%$ 湿度下, 吸湿30 min, 纤维膜温度最高可提升 $2.3\text{ }^{\circ}\text{C}$ 。



引言

Wool macromolecules have a large number of disulfide bonds, which can be reduced to thiols (-SH groups) by the treatment of thioglycolic acid to wool. By the strong reducibility of -SH groups, wool-g-poly(glycidyl methacrylate) (wool-g-PGMA) can be prepared by graft copolymerization of wool with GMA by building a redox system between -SH groups and sulfhydryl ammonium persulfate (APS). Wool-g-PGMA was characterized by the analyses of Fourier transform infrared (FTIR) spectroscopy, scanning electron microscopy (SEM), thermogravimetric (TG) and x-ray diffraction (XRD). Influences of molar concentrations of monomer and initiator as well as reaction temperature on grafting ratios were investigated. The experimental results showed that the -SH groups/APS redox system built could effectively initiate graft polymerization of lipophilic GMA on wool surface in an aqueous medium. The suitable process parameters of graft copolymerization were: 0.6 mmol/L molar concentration of GMA, 3.0 mmol/L molar concentration of APS and reaction temperature of 50°C. At the suitable parameters, grafting ratio of wool-g-PGMA showed a maximum value of 195.8%, indicating an efficient graft copolymerization was achieved. The copolymerization could obviously reduce degree of crystallinity of wool. The wool-g-PGMA had higher thermal stability than raw wool at the temperature of below 406°C by performing the TG analysis. The measurement of oil absorbency and oil retention revealed that wool-g-PGMA could improve the high-value utilization of wool in the application of oily wastewater treatment.

实验过程

The surface-initiated grafting method refers to introduction of the active sites on the surface of the matrix and subsequently introducing the grafted branches into the sites of the matrix surface. Active sites include polymerizable double bonds and initiating groups. In order to confirm the types of active sites in the graft polymerization of this work, the controlled experiments of preparing wool-g-PGMA samples are performed, as shown in Table 1. The graft copolymerization in the experiments (I, II and III) contained the addition of APS solution (3.0 mmol/L) used as the initiator whereas the copolymerization in the experiments (IV, V and VI, as the contrast) did not contain the addition of APS. The experimental results showed that the wool samples without adding the initiator had no increase in the weights, which indicated that the graft polymerization was initiated by the -SH groups/APS redox system.

The preparation process of initiating graft polymerization of GMA on the wool surface by -SH groups/APS redox system is shown in Scheme 1. The disulfide bonds on the wool molecules are reduced into the -SH groups by the treatment of thioglycolic acid to wool. The -SH groups can constitute redox system with the APS in an aqueous medium. The -SH groups cause the decomposition of APS to produce sulfate free radicals at a lower temperature, meanwhile the hydrogen atoms on the -SH groups of the wool surface are transferred to the sulfate free radicals. As a result, a large number of sulfur free radicals are formed on the wool surface, which directly initiates the graft copolymerization of GMA on the wool surface, introducing grafted PGMA branches onto the wool surface and forming the wool-g-PGMA samples with high grafting ratios.

结果和讨论

When the molar concentrations of APS and GMA were 3.0 mmol/L and 0.6 mmol/L, respectively, influence of reaction temperature on the graft copolymerization of GMA on the surface of wool was investigated, as shown in Fig. 1. It could be seen that the grafting ratio of GMA was dependent on the reaction temperature. In the temperature range of 15-70°C, grafting ratio gradually increased, reached its maximum value of 195.8% when the temperature was 50°C, and then decreased. When the temperature was lower than 50°C, the decomposition rate of the APS increased as the temperature raised, leading to an increased grafting ratio. However, as the temperature was more than 50°C, the decomposition rate of the APS would increase rapidly, which might result in an increase in the homopolymerization of GMA due to the obvious increases in the amounts of free radicals in the reaction system. For the reason, a reduced grafting ratio could be expected as the temperature exceeded 50°C. Accordingly, we concluded that the appropriate reaction temperature under the given process conditions was 50°C.

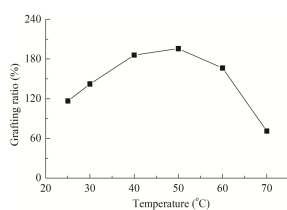
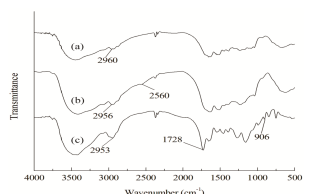
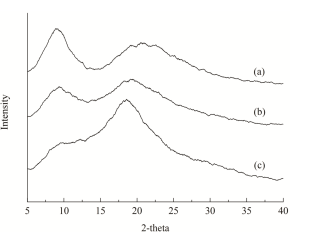


Fig. 4 shows FTIR spectra of raw wool, sulfhydrylated wool and wool-g-PGMA samples. The peaks appeared at 2960 cm⁻¹, 2956 cm⁻¹ and 2953 cm⁻¹ corresponded to the characteristic absorption peak of the C-H. And the peaks at 1644 cm⁻¹, 1542 cm⁻¹ and 1390 cm⁻¹ correspond to the amide I band (C=O telescopic vibration peak), the amide II band (N-H expansion vibration peak), the amide III band (C-N telescopic vibration peak), respectively. In addition, a new peak appeared at 2560 cm⁻¹ in the spectra of sulfhydrylated wool (Fig. 4(b)), which belongs to the characteristic peak of sulfhydryl groups and indicates the successful introduction of the sulfhydryl groups on the wool surfaces. There was no sign of this bond in the spectrum of the wool-g-PGMA (Fig. 4(c)), and there were two new peaks appeared at the wavenumbers of 1728 cm⁻¹ and 906 cm⁻¹. The peak at 1728 cm⁻¹ corresponded to the characteristic absorption band of C=O in the PGMA branches. The other one appeared at 906 cm⁻¹, which indicated the asymmetric absorption vibration of the epoxy groups. The two new peaks demonstrated the successful grafting of the PGMA branches on wool surface.



XRD patterns of raw wool and wool-g-PGMA samples with the grafting ratios of 50.5% and 137.0% are depicted in Fig. 6. It could be seen that there was no difference in the crystal configuration of the wool before and after grafting. Both raw wool and wool-g-PGMA samples appeared the diffraction peaks at about 9.0° and 19° (2θ). The strong diffraction peak appears at about 9.0° corresponded to the common diffraction peaks of α-crystallization and β-crystallization, while the strong diffraction peak at about 19° corresponded to the peak of β-crystallization. In addition, it could be seen that the peak intensity at about 9.0° diminished, whereas the intensity at about 19° enhanced after graft copolymerization. Compared with that of wool-g-PGMA sample (GR=50.5%), the peak intensity at about 9.0° of the wool-g-PGMA (GR=137.0%) obviously weakened, while an increased peak intensity at about 19° was exhibited. The degrees of crystallinity were 33.3%, 25.4% and 18.1% for the raw wool and wool-g-PGMA samples with the grafting ratios of 50.5% and 137%, respectively, which implied the graft polymerization was able to reduce the degree of crystallinity of wool. The reduction of degree of crystallinity is probably attributed that the graft polymerization destroys the scale layer of wool fiber and thus lowers the α-degree of crystallinity of wool.



结论

The surface-initiated grafting method refers to introduction of the active sites on the surface of the matrix and subsequently introducing the grafted branches into the sites of the matrix surface [17]. Active sites include polymerizable double bonds and initiating groups [18]. In order to confirm the types of active sites in the graft polymerization of this work, the controlled experiments of preparing wool-g-PGMA samples are performed, as shown in Table 1. The graft copolymerization in the experiments (I, II and III) contained the addition of APS solution (3.0 mmol/L) used as the initiator whereas the copolymerization in the experiments (IV, V and VI, as the contrast) did not contain the addition of APS. The experimental results showed that the wool samples without adding the initiator had no increase in the weights, which indicated that the graft polymerization was initiated by the -SH groups/APS redox system.

The preparation process of initiating graft polymerization of GMA on the wool surface by -SH groups/APS redox system is shown in Scheme 1. The disulfide bonds on the wool molecules are reduced into the -SH groups by the treatment of thioglycolic acid to wool. The -SH groups can constitute redox system with the APS in an aqueous medium. The -SH groups cause the decomposition of APS to produce sulfate free radicals at a lower temperature, meanwhile the hydrogen atoms on the -SH groups of the wool surface are transferred to the sulfate free radicals. As a result, a large number of sulfur free radicals are formed on the wool surface, which directly initiates the graft copolymerization of GMA on the wool surface, introducing grafted PGMA branches onto the wool surface and forming the wool-g-PGMA samples with high grafting ratios.

Cross-linking/sulfonation to improve paste stability, adhesion and film properties of corn starch for warp sizing

Zhengqiao Zhang, Wei Li, Lanjuan Wu, Zhifeng Zhu, Qingqing Ni, Zhenzhen Xu, Jie Wu

1. College of Textiles and Garments, Anhui Polytechnic University, Wuhu, 241000, Anhui, China;

2. Department of Mechanical Engineering and Robotics, Shinshu University, 3-15-1 Tokey, Ueda, Nagano, 386-8576, Japan

Introduction

No studies have been conducted on the IA cross-linking and sulfonation of starch, and little is known about the influence of such reactions on the properties of starch (such as viscosity stability, adhesion, film properties, and desizability). Therefore, one of the aims of this research was to reveal if IA cross-linking/sulfonation can stabilize paste viscosity, ameliorate adhesion to cotton and polyester fibers, and diminish film brittleness. Moreover, the influence of the level of cross-linking (LCL) of IA and the degree of substitution (DS) of sulfonates on the properties have also been analyzed. The obtained starch samples in this work were characterized by scanning electron microscopy (SEM), and measurements of LCL and DS of IACLSS samples, apparent viscosity and viscosity stability of cooked starch paste, adhesion to cotton and polyester fibers, tensile strength, breaking elongation, moisture regain of the films and time required to break the films in hot water, were performed.

Experimental process

Preparation

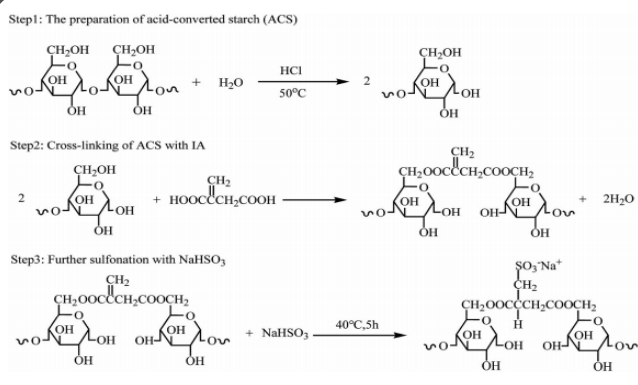


Fig. 1. The preparation of IACLSS samples.

Characterization and measurement

Briefly, 324 g of dried acid-converted starch (ACS) was dispersed in distilled water containing itaconic acid (IA) for forming a 40 wt% starch aqueous suspension. After being stirred at room temperature for 30 min, the dispersion was vacuum-filtered to form a cake. After being dried at 50 °C for 2 h and at 75 °C for 4 h, the cake was pulverized, and sieved for passing through a 100-mesh sieve. Thereafter, the powered starch was cross-linked at 130 °C for 3 h. Finally, the product was washed to remove residual IA with distilled water, dried at 50 °C, pulverized, and sieved with a 100-mesh sieve. Dried IA cross-linked starch (IACLS, 162 g) was dispersed in distilled water containing sodium for forming a 35 wt% starch aqueous dispersion. Then, the dispersion was mechanically stirred and heated to 40 °C, and the sulfonation was performed for 5 h. Finally, the product was neutralized to approximately pH 7 using a 6 wt% Na₂CO₃ solution, filtered, washed with a mixture of ethanol and distilled water 4 times, vacuum-dried at 40 °C, pulverized, and sieved with a 100-mesh sieve to obtain the IACLSS.

Results and discussion

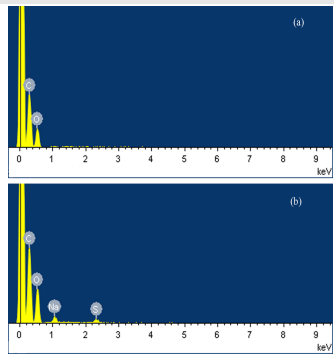


Fig. 2. EDS images of ACS (a) and IACLSS (b).

The experimental results showed that cross-linking/sulfonation could improve the viscosity stability of cooked starch paste, enhance the adhesion of starch to cotton and polyester fibers, increase breaking elongation and bending endurance as well as decreasing its tensile strength, thereby stabilizing paste viscosity, ameliorating the adhesion to fibers and diminishing film brittleness.

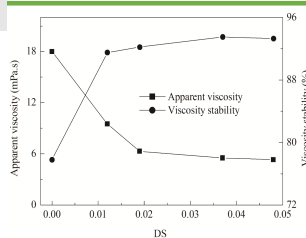


Fig. 3. Apparent viscosity and its stability of gelatinized QHOTS paste.

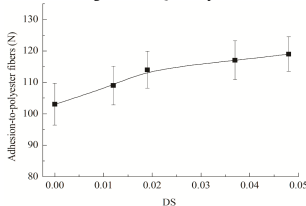


Fig. 5. Influence of cross-linking/sulfonation on adhesion of starch to polyester fibers.

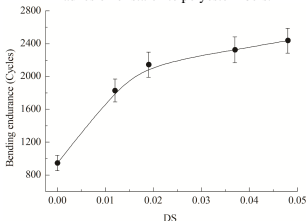


Fig. 7. Influence of cross-linking/sulfonation on bending endurance of ACS film.

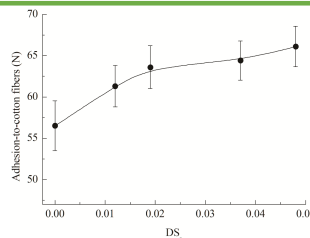


Fig. 4. Influence of cross-linking/sulfonation on adhesion of starch to cotton fibers.

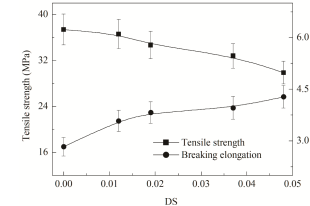


Fig. 6. Influence of cross-linking/sulfonation on tensile properties of starch film.

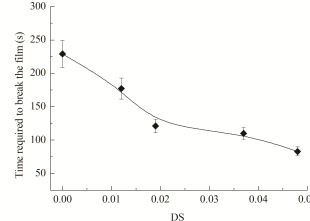


Fig. 8. Influence of cross-linking/sulfonation on time required to break the film.

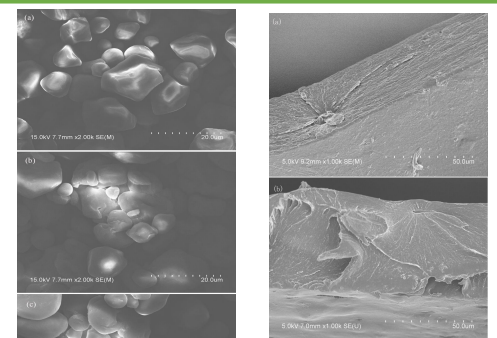


Fig. 9. SEM images of ACS granules (a), IACLS ones (b) and IACLSS ones (c).

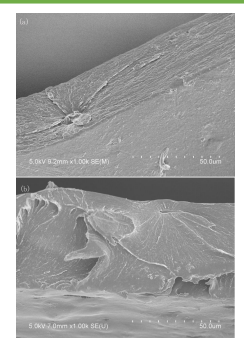


Fig. 10. SEM images of the cross sections of ACS film (a) and IACLSS film (b).

In addition, the modification could reduce the time required to break the films in 80 °C water, indicating that modification favored desizing of starch in hot water. Increasing sulfonation levels whilst decreasing the LCL values favored improvement in stability and desizability, enhancement in the adhesion to both fibers, and decrease in brittleness.

Conclusions

- ◆ IA cross-linking and sulfonation of starch with IA and NaHSO₃, respectively, were able to eliminate the drawbacks of starch for ameliorating its end-use ability in warp sizing.
- ◆ The adhesion of IACLSS to cotton and polyester fibers as well as breaking elongation, bending endurance of the IACLSS film were superior to those of ACS, and its tensile strength was inferior to that of ACS, implying the modification could enhance the adhesion and reduce film brittleness.
- ◆ IACLSS with the DS_s and a LCL ranges of 0.037-0.048 and 26.0-19.8 (AGU/CL) showed potential in the applications of cotton and polyester sizing.

Electrospun flexible core-sheath PU/PAN/ β -CD@Ag nanofiber membrane decorated with ZnO: Enhance the practical ability of semiconductor photocatalyst

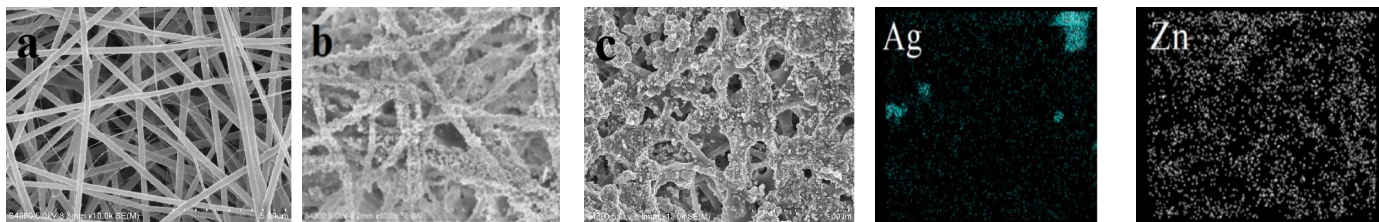
Suo Liu, Dingsheng Wu, Lingling Zhao, Lei Zhao, Maohuan Yang, Quan Feng
(School of Textile and garment, Anhui Polytechnic University, Wuhu, Anhui)

Introduction

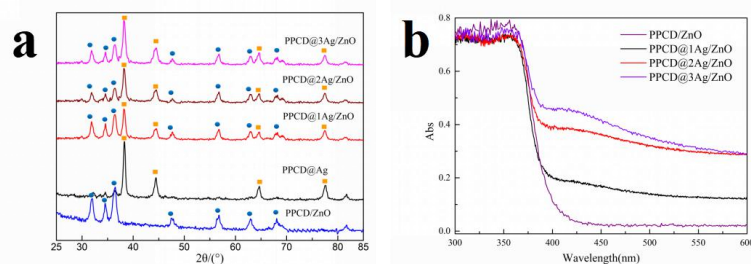
Tetracycline hydrochloride (TCH) is a hormonal substance widely used in pharmaceutical husbandry industries. However, it could cause serious pollutio. Printing and dyeing wastewater represented by methylene blue (MB) also cause serious harm to the human body without thorough treatment, due to its complex components and poor biodegradability. Photocatalytic technology represented by metal oxides may be one of the most effective way to solve above environmental problems in the process of rapid development of human society. Among all the photocatalytic materials, ZnO has been widely used in the field of industrial wastewater due to its high photocatalytic activity and chemophysical stability. However, ZnO NPs as a nano-sized semiconductor photocatalyst have three main disadvantages that make them not suitable in the extensive treatment of industrial wastewater: poor photoresponse range, low degradation efficiency, and worse reuse performance. In the work, we prepared and characterized PAN/PU/ β -CD nanofiber membrane firstly, followed by Ag NPs were dispersed in the nanofiber membrane surface by effectively controlling the sequence and parameter in the reaction process, which could avoid the inert Ag NPs caused by its aggregation in the nanofiber membrane. Simultaneously, MB and TCH were used to confirm its visible-light photocatalytic performance and reusability.

Experimentation

1. Electrospun PU/PAN/ β -CD nanofiber membrane
2. Synthesis of silver-coated PPCD nanofiber membrane
3. Preparation of ZnO loaded on PPCD@Ag nanofiber membrane



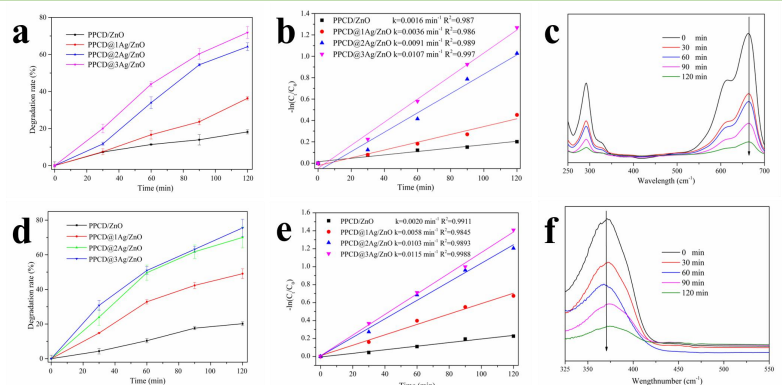
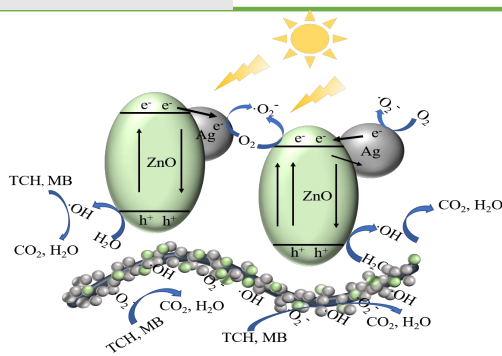
Results and Discussion



Significantly, all the characteristic peaks of ZnO and Ag NPs appear in PPCD@Ag/ZnO sample, which indicate that Ag and ZnO NPs could be coexistence on the nanofiber membrane with correct crystal form.

As we expected, PPCD@Ag/ZnO sample have good absorption capacity at a wavelength greater than 390 nm. Enhancing the light capture efficiency is owed to the plasma resonance of Ag NPs.

Conclusion



- [1] Rasheed, Haroon. Ur., et al. J. Environ. Chem. Eng. 2019,7(3).
- [2] Ahmed, Waheed., et al. Ceram. Int. 47(17), 2021, 24895-24905.
- [3] Wei, MB., et al. Mater. Express. 2019, 9(5), 413-418.
- [4] M Lettieri., et al. Build. Sci. 2019,147, 506-516.
- [5] Wu, Di., et al. J. Hazard. Mater. 2019, 377, 1-7.
- [6] Chen, Fei., et al. J. Catal. 2017,352, 160-170.
- [7] Xu, Difa., et al. Appl. Catal., B. 2015,164, 380-388.
- [8] Cao, HuaMin., et al. Mater. Charact. 2020,160(110125).

The practical results show PAN/PU/ β -CD@3Ag/ZnO nanofiber membrane has a good photocatalytic degradation performance for 10 mg/L MB and TCH under visible light, and the degradation rate reached 71.5% and 70.5%, respectively, and its catalytic activity remains 89.6% and 70.5% even up to 5 cycles.

Highly loading TiO₂ and Au on flexible three-dimensional network (bacterial cellulose) for photoelectric synergistic degradation of tetracycline hydrochloride under visible light irradiation

Tang Zhou, Quan Feng*, Dingsheng Wu, Suo Liu, He Wang, Haiao Zeng
(Anhui Polytechnic University, Wuhu 241000, China)

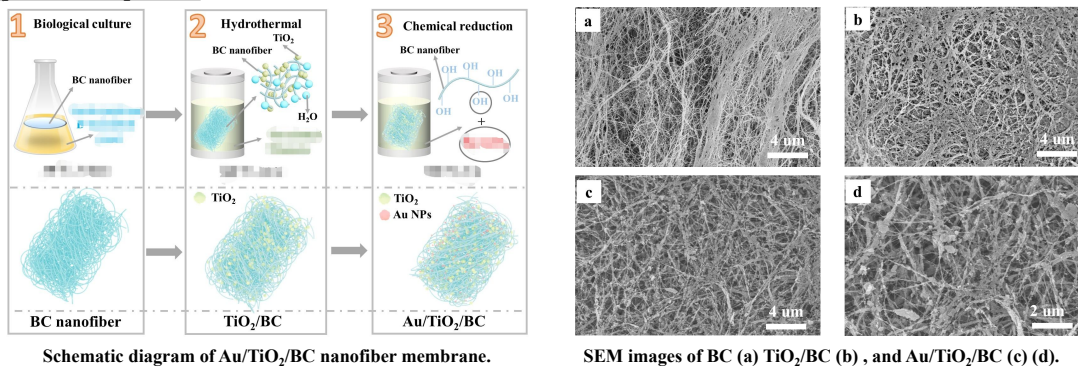
Introduction

As an emerging and promising technology, photoelectric catalytic technology (PEC) can effectively remove trace organic pollutants such as tetracycline hydrochloride (TC-HCl, an antibiotic) in water. Among the photocatalysts, titanium dioxide (TiO₂) has been widely investigated as a preferred material. However, the efficiency of TiO₂ photocatalyst is presently limited by the wide bandgap (3.0–3.2 eV) and the fast quenching of photogenerated electron-hole pairs. Surprisingly, light can cause collective oscillations of conduction electrons in the matter metallic (e.g., Au) nanostructures. This strong localized surface plasmon resonance (SPR) can confine optical fields in a nanoscale space, and create the hot spot exciting the electrons to energy levels above the Fermi level of Au. In addition, the noble metal on TiO₂ can prevent recombination of photo-generated electron-hole pairs by forming schottky barrier due to the different work function with the photocatalyst.

In recent years, the immobilization of catalysts on specific substrates has become a current research focus. Bacterial cellulose (BC), biosynthesized primarily by Gram-negative *Komagataeibacter xylinus* (*K. xylinus*), exhibited promising potential as alternative eco-friendly substrates for electronics, photonic, and energy storage devices due to their unique microstructures. The three-dimensional network of nanofibers and porosity of BC can allow other materials to be incorporated and form reinforced composites.

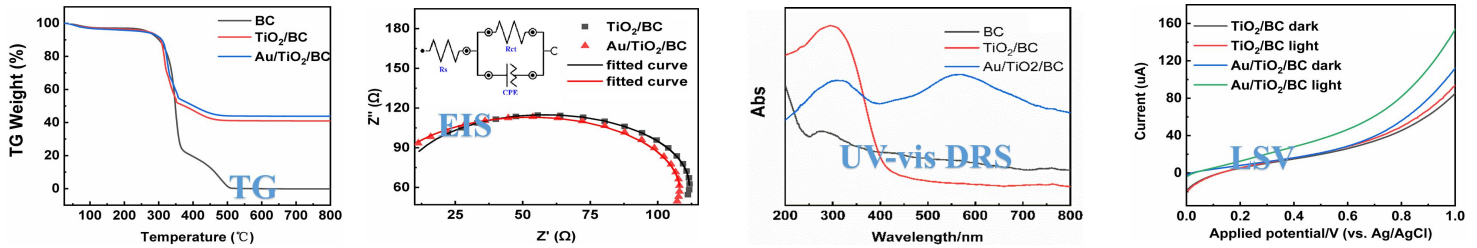
Based on the previous studies, this study presented a novel approach to immobilize TiO₂ NPs and Au NPs into the three-dimensional network structure of BC membrane. This work can provide valuable insights to the design of flexible photoelectrocatalytic materials.

Experimental process



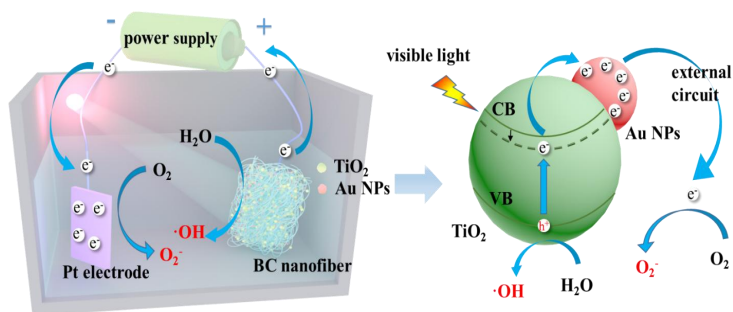
In this study, the TiO₂ and Au nanoparticles were highly loaded on the three-dimensional network of bacterial cellulose by biological culture, hydrothermal method and chemical reduction.

Results and discussion

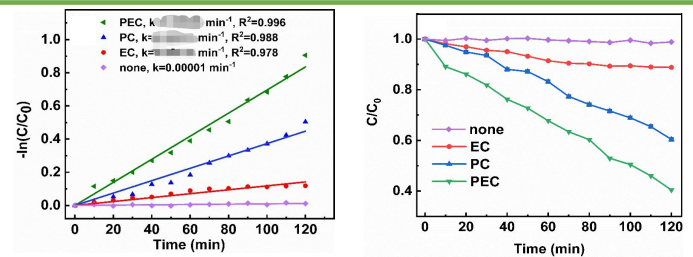


The result from TG indicated the weight loss of Au/TiO₂/BC membrane shown a high loading capacity of nanofiber. The UV-vis DRS indicated that Au NPs significantly enhanced the light response range. The results of LSV, EIS and photo-current responses measurements indicated that Au/TiO₂/BC membrane had a good photoelectrochemical performance under light and additional electric field.

Conclusion



Schematic diagram of Au/TiO₂/BC nanofiber membrane.



The system has exhibited excellent light absorption, obvious photo-current response and effective charge separation. These results further supported Au/TiO₂/BC membrane might serve as promising high-performance photoanode. The degradation efficiency of TC-HCl by PEC (* min⁻¹) was 5.90 (* min⁻¹) and 1.87 (* min⁻¹) times than that by Electrocatalysis (EC) and photocatalysis (PC) under visible light irradiation, respectively, showing the synergistic effect of electrocatalysis and photocatalysis.

References:

- [1] B. Ma, N. Yu, S. Xin, Y. Xin, C. Zhang, X. Ma, M. Gao, *Chemosphere*, 267 (2021) 129242.
- [2] Q.L. Chen, W.L. Yang, J.J. Zhu, L.C. Fu, D.Y. Li, L.P. Zhou, *Journal of Hazardous Materials*, 384 (2020).
- [3] A.A. Memon, A.A. Arbab, S.A. Patil, N. Mengal, K.C. Sun, I.A. Sahito, S.H. Jeong, H.S. Kim, *Applied Catalysis a-General*, 566 (2018) 87-95.
- [4] F. Zhou, Z. Zhang, J. Wang, S. Huang, J. Liu, Y. Li, Q. Wang, W. Liu, *Nanotechnology*, 31 (2020) 375606.
- [5] Y. Zhang, J.B. Zhou, J.H. Chen, X.Q. Feng, W.Q. Cai, *Journal of Hazardous Materials*, 392 (2020).
- [6] J.J. Wu, Y.F. Zhang, J.S. Zhou, K.N. Wang, Y.Z. Zheng, X. Tao, *Applied Catalysis B-Environmental*, 278 (2020).
- [7] C.J. Liu, Y.H. Yang, J. Li, S. Chen, W.Z. Li, X.D. Tang, *Chemical Engineering Journal*, 326 (2017) 603-611.
- [8] R. Montenegro-Ayo, J.C. Morales-Gomero, H. Alarcon, A. Corzo, P. Westerhoff, S. Garcia-Segura, *Chemosphere*, 268 (2021) 129320.
- [9] Z.L. Wang, L.W. Lai, Y.C. Wang, T.F. Zhang, Z.Z. Huang, Y.H. Jin, J.P. Wang, K.L. Jiang, S.S. Fan, Q.Q. Li, *International Journal of Hydrogen Energy*, 45 (2020) 31963-31975.
- [10] B. Gao, M. Sun, W. Ding, Z. Ding, W. Liu, *Applied Catalysis B: Environmental*, 281 (2021).

C6位羧基纤维素制备及其对金属离子吸附性能

李继丰, 张涵林, 戴千淳, 杜兆芳*
安徽农业大学, 合肥, 中国
dzf@ahau.edu.cn

引言

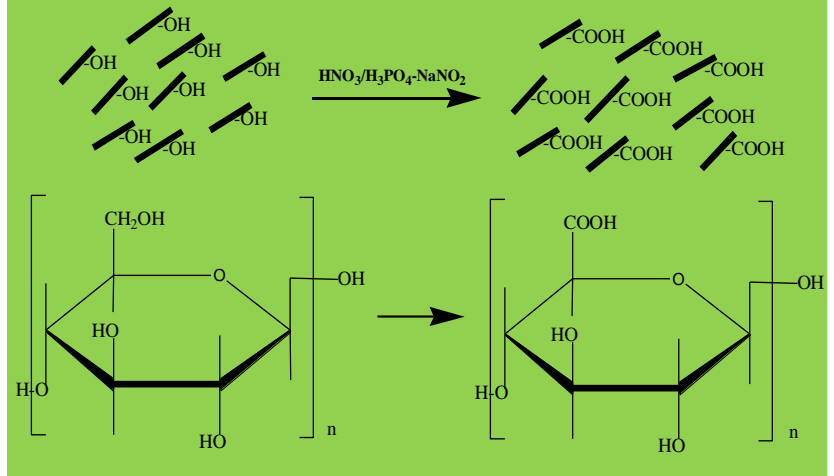
随着经济和工业的快速发展, 带来了印染、皮革和电子等行业大量含有金属离子的污水的排放。分析发现, 天然纤维素吸附剂应用在金属离子去除主要存在的问题是吸附容量小、选择性低等。虽然改性天然纤维素吸附剂能够提高对金属离子吸附量, 但吸附效果仍不理想, 这主要是因为天然纤维素在分子链和分子间形成大量氢键, 使其结构紧密, 纤维素反应可及性低, 导致纤维素表面的官能团改性接枝率低, 最终造成改性纤维素吸附剂应用效果差。为提高纤维素对金属离子污染物的吸附能力, 本实验通过选择性氧化体系制备C6位羧基微晶纤维素(CMCC), 并研究了CMCC对Cu²⁺吸附性能。

实验过程

实验药品:

微晶纤维素(MCC); 硝酸(68% w/v), 磷酸(85% w/v), 亚硝酸钠, 三水硝酸铜(Cu(NO₃)₂·3H₂O), 分析纯, 购于国药集团化学试剂有限公司; 去离子水。

实验流程图



结果和讨论

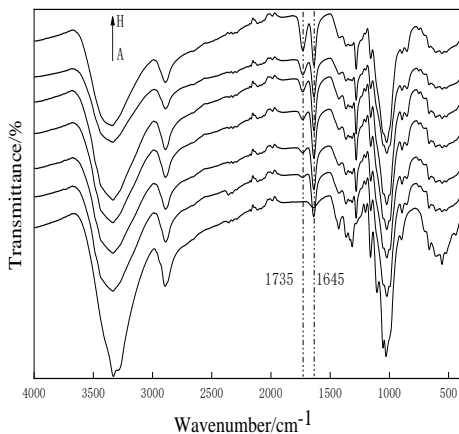


Fig. 1 FT-IR spectra of MCC by oxidized with different time (A: original MCC; B-H: MCC with oxidation of 30 min, 60 min, 90 min, 120 min, 150 min, 180 min, 300 min, respectively)

HNO₃/H₃PO₄-NaNO₂ 氧化的MCC在1735 cm⁻¹处出现了羧基C=O的伸缩振动吸收峰, 且1645 cm⁻¹附近的吸收峰随着氧化时间的增加, 吸收峰强度也在不断增加, 上述两处吸收峰强度在不断增加。

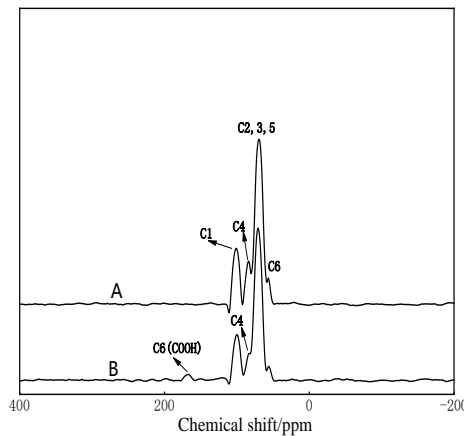


Fig. 2 Solid-state ¹³C CP/MAS NMR spectra of MCC and CMCC (A: original MCC; B: CMCC)

HNO₃/H₃PO₄-NaNO₂ 氧化的MCC在62-69 ppm处出现了羧基, 且在175 ppm附近出现了羧基碳原子的信号, 这说明MCC分子中C6上的羟基基团已被HNO₃/H₃PO₄-NaNO₂体系选择性氧化成羧基。

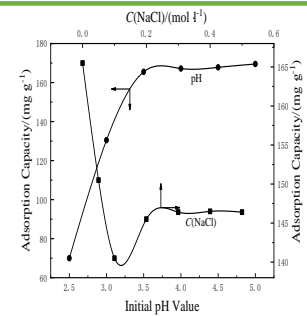


Fig. 3 Effect of pH and NaCl on the adsorption properties of CMCC-3

pH=2.5为吸附条件, 吸附液NaCl浓度在0.2 mol/L左右, NaCl浓度增加, CMCC/Cu²⁺吸附量逐渐降低, 当NaCl浓度超过0.2 mol/L时, CMCC/Cu²⁺吸附量基本保持不变。

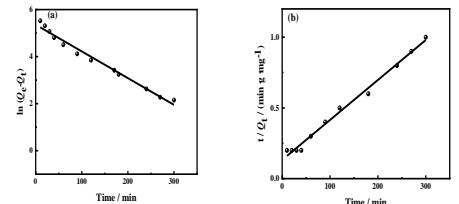


Fig. 4 Kinetic fitting curves of adsorption data of Cu²⁺ onto CMCC-3 (a) pseudo-first-order kinetic model and (b) pseudo-second-order kinetic model

羧基微晶纤维素对Cu²⁺具有良好的吸附性能, 吸附行为遵循准二级动力学模型, 在303 K下吸附容量高达165.5 mg/g。

结论

(1)通过HNO₃/H₃PO₄-NaNO₂体系可将微晶纤维素选择性氧化成C6位羧基微晶纤维素,保持了纤维素的基本骨架结构。氧化得到的羧基微晶纤维素具有良好的吸湿性。

(3)吸附实验表明, 羧基微晶纤维素对Cu²⁺具有良好的吸附性能, 吸附行为遵循准二级动力学模型, 在303 K下吸附容量高达165.5 mg/g。